UNIVERSITÀ DEGLI STUDI DI MILANO-BICOCCA

Department of Materials Science

Ph.D. in Materials Science and Nanotechnology

(XXXV Cycle)

Additive Manufacturing by Digital Light Processing (DLP)

Rajat Chaudhary

Matr. N. 862575

Supervisor: Prof. Carlo Antonini

Co-supervisor: Dr. Francesca Mazzanti

Coordinator: Prof. Marco Bernasconi

Academic year 2021/2022

“Logic will get you from A to B. Imagination will take you everywhere.”

-Albert Einstein

I understood the first half of the quote in my academics,

but I realized the latter during my Ph.D. in Additive Manufacturing.

Acknowledgments

This thesis discusses only the collection of my research work. But what it does not discuss is the experience I gained in the past three years. I could not imagine myself as mature as I am today, three years back as a person or in research. This was possible only because of the people around me and the environment they provided.

First and foremost, words cannot express my sincere gratitude to my supervisor Prof. Carlo Antonini for his constant support, patience, motivation, immense knowledge, and teachings during the Ph.D. and related research. His guidance helped me all the time inside and outside the research. Needless to say, I would not be grown as much as I am today without him. I also share my gratitude to my co-supervisor Dr. Raziyeh Akbari. Her insightful inputs constantly made me grow as a researcher.

Further, I am extremely grateful to Dr. Giuseppe Magnani, director of Laboratory of Material Technologies Faenza (TEMAF), for hosting me at ENEA, Faenza. I could have not taken this journey without Dr. Francesca Mazzanti whose supervision helped in building the initial fundamentals of the research during my period at the ENEA-TEMAF lab. I also extend my gratitude to Dr. Enrico Leoni, Dr. Paride Fabbri and other colleagues for their constant support during my work.

My courteous thanks to Prof. Marco Bernasconi, coordinator of the Ph.D. program in Materials Science and Nanotechnology and the doctoral school, University of Milano-Bicocca for their technical and financial support. I also acknowledge my Ph.D. funding from Regione Lombardia under the program “Laboratorio sui Materiali e processi industriali sostenibili 4.0” (Accordo di collaborazione RL-ENEA).

I would also like to express my deepest regards to Abhinav for being by my side from the very beginning. Thanks to all my colleagues at SEFI Lab for their kind and enjoyable company. I feel blessed to find all these wonderful people who were part of this memorable journey.

Finally, I would like to thank my family, especially my parents and brother for their blessings, unconditional support, love and care, which kept me feel close to them, no matter the distance.

Preface

Additive Manufacturing (AM) or 3D printing is a process, based on different technologies, for the design and fabrication of three-dimensional objects, an alternative to conventional subtractive manufacturing. AM enables cost-effective manufacturing especially for complex geometries, potentially with lower environmental impacts compared to conventional processes, due to design flexibility and reduced waste. These advantages have drawn the attention of various industrial sectors, for a variety of applications. Currently, several AM technologies are being used to manufacture lightweight, functional, and non-functional parts.

Among them, Digital Light Processing (DLP) is one of the most recent and promising technologies for producing high-definition functional and non-functional parts. When compared to stereolithography (SLA), which is based on a laser source for voxel-by-voxel polymerization, one of the major advantages of DLP is the use of a high-resolution source, curing an entire layer with one projection at each step, thus reducing the overall printing time. Initially developed for producing prototypes using pure photopolymers (resins), the technology has been recently tested to print ceramic and metal suspensions. Currently, the technology is being used to produce 3D parts using functional materials, such as elastomers, conductive polymers, shape memory polymers, biopolymers and piezoelectric materials. These photocurable, environmentally responsive materials add up another dimension to the printed part extending 3D printing to 4D printing.

In this thesis, the novelties and peculiarities of DLP are highlighted in contrast to other AM technologies. Further, it covers various aspects of the DLP printing process including material preparation, insight into light-matter

interaction during printing, and applications together with the advancements in DLP technology. The study also focuses on printing optimization for pure photopolymers, as well as ceramic and metal suspensions. Further, a simple methodology based on preliminary printing tests of single layers is proposed, to identify the material properties, including the penetration depth and critical energy. Such information is the base to draw a printing map using layer thickness and exposure time as independent variables: as such, a printing space is defined within the constraint of material printability, thus ensuring optimal polymerization during three-dimensional object printing.

Contents

1. Additive Manufacturing 13

1.1. Introduction 14

1.2. AM steps 18

1.3. Additive manufacturing technologies 20

1.3.1. Selective Laser Sintering (SLS) 20

1.3.2. Electron Beam Melting (EBM) 20

1.3.3. Laser Engineered Net Shaping (LENS) 21

1.3.4. 3DP or binder jetting 22

1.3.5. Laminated Object Manufacturing (LOM) 22

1.3.6. Fused Deposition Modeling (FDM) 23

1.3.7. PolyJet (PJT) 23

1.3.8. Stereolithography (SLA) 24

1.3.9. Digital Light Processing (DLP) 24

2. Digital Light Processing and Applications 27

2.1. Digital Light Processing 28

2.2. Post-processing 34

2.2.1. Cleaning of the green body 34

2.2.2. Removal of the support structure 35

2.2.3. UV curing 35

2.2.4. Debinding 36

2.2.5. Sintering 37

2.3. Applications 39

3. Photopolymers and Light-Matter Interaction 45

3.1. Photoinitiating systems 46

3.1.1. Free radical system 49

3.1.2. Ionic system 51

3.1.3. Oligomers and monomers 52

3.2. Resins and suspensions 53

3.2.1. Ceramic feedstock 53

3.2.2. Metallic feedstock 58

3.3. Light interaction with pure photopolymers *60*

3.4. Light interaction with suspensions *65*

4. Materials and Experimental Methods **67**

4.1. Photopolymers *68*

4.2. Printer and software *69*

4.2.1. Radiation Source 69

4.2.2. Vat (resin container) 70

4.2.3. 3D design and Slicing 71

4.2.4. Mask generation 71

4.3. Printability tests of photopolymer *73*

4.4. Sample preparation for photopolymer characterization *74*

4.5. Characterization *76*

4.5.1. Radiation Characterization of Voyager Z-20 76

4.5.2. Material Characterization 76

4.6. Post-printing and thermal treatment *78*

4.6.1. Sample cleaning 78

4.6.2. Debinding and Sintering 78

5. Results **81**

5.1. Experiments performed with 3DL Printer - HD 2.0+ printer *82*

5.1.1. Surface homogeneity tests 82

5.1.2. Effect of masks 84

5.1.3. Effective printing parameters 85

5.1.4. Freeform layer thickness determination 87

5.2. Rational design and characterization of materials with Voyager Z-20 printer *89*

5.2.1. Radiation source characteristics 89

5.2.2. Preliminary characterization of resins 90

5.2.3. Polymerization of monolayer films 92

5.2.4. FTIR-ATR analysis 97

5.2.5. Optimized 3D printing space 99

5.3. Preliminary thermal treatment *102*

5.3.1. Debinding and sintering 102

5.3.2. SEM analysis 104

6. Conclusions and perspectives **107**

7. Bibliography **113**

1. Additive Manufacturing

1.1. Introduction

Additive manufacturing is a layer-by-layer strategy enabling the advanced design and fabrication of complex 3D objects and structures, overcoming geometry limitations and reducing waste production compared to conventional technologies. Additive manufacturing, rapid prototyping, rapid manufacturing, layer-oriented manufacturing, digital fabrication, 3D printing [1], and many more terms have been introduced after the patent filed by Chuck Hull in 1984 [2] before standardization in ISO/ASTM 52900: 2015 (Additive manufacturing - General Principles - Terminology)[1]. At present, the term additive manufacturing (AM) is more common in the scientific and technical communities, whereas 3D printing is usually preferred in communications with the general public. In a nutshell, AM reverses the conventional approach of subtractive fabrication techniques: it is based on layer-upon-layer fabrication of an object, starting with liquid or solid powder as a raw material to form a three-dimensional (3D) object from stacking of two-dimensional (2D) layers. Within the framework of the fourth industrial revolution, also referred to as Industry 4.0 [3], AM is a part of the larger plan to integrate digital technology and Internet of Things (IoT) with conventional technologies [4]. This integration leads to the reduction of space needed for production, irrespective of the output mass, and can help to reduce the efforts of setting up a conventional manufacturing unit by facilitating customization. One of the most significant advantages of AM is the almost constant manufacturing cost, which is independent of the production scale and, to some extent, the product shape complexity [5] (Figure 1.1 a). Minimal production of waste makes this technology environmental-friendly [6] and provides an advantage towards

[1] https://www.iso.org/obp/ui/#iso:std:iso-astm:52900:ed-1:v1:en (last access: 3rd February 2022).

sustainable manufacturing compared to traditional manufacturing methods. These features have attracted various manufacturing sectors [7], such as biomedical/dental [8–10], automobile [11], aviation [12], and construction [13], from the early stages of AM development. Many more sectors are adopting AM, making the manufacturing process economically affordable and environmentally sustainable (Figure 1.1 b).

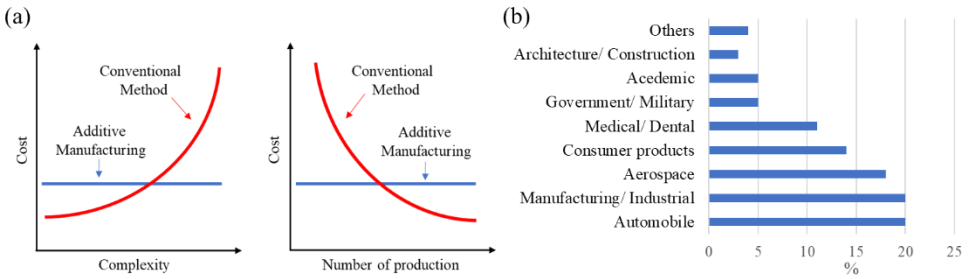

Figure 1.1 Comparison of additive manufacturing and conventional manufacturing methods in cost, complexity, and the number of productions. (b) Distribution of AM revenues from different sectors (Source: Canada's Additive Manufacturing Ecosystem, ICTC; Wholers 2019).

As a result, AM technology has gained remarkable popularity in the last decade. The industrial potential is also reflected by the steady and exponential rise in the number of research articles (Figure 1.2), which have focused on the development of new technologies improving AM by achieving faster and cost-effective processes, and materials with enhanced properties (mechanical, finishing, etc.).

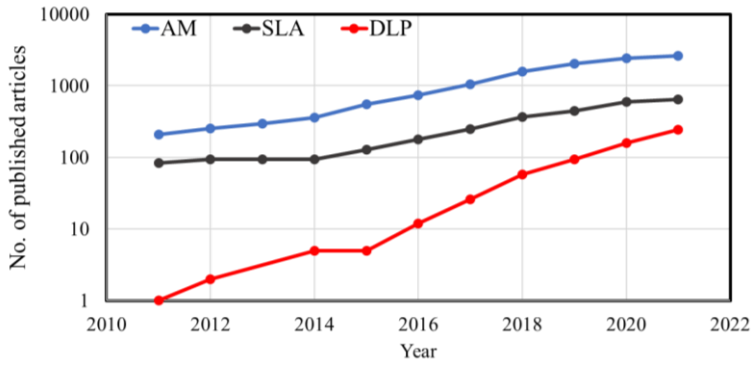

Figure 1.2 Statistics related to AM, extracted from Scopus, show an increase in articles published from 2011 to 2021. The following keywords were used to extract results: for "AM"- {Selective laser sintering} OR {selective laser melting} OR {laser engineered net shaping} OR {prometal} OR {3DP binder jetting} OR {laminated object manufacturing} OR {fused deposition modeling} OR {polyjet technology} OR {stereolithography} OR {vat polymerization}; for "SLA"- {stereolithography} OR {vat polymerization}; for "DLP"- ("Digital light processing") AND ("Additive Manufacturing") OR ("3D Printing"). The keywords were searched within TITLE-ABS-KEY. (Query performed on: 20th January 2022).

In recent years, a new range of materials and printing technologies [14,15], including friction-based [16,17], has been developed for various applications [18]. Among various AM technologies, digital light processing (DLP) is a technology used to print photopolymer parts, using a projected light source to cure an entire layer at once. Initially developed for pure resins, recent advances have demonstrated the potential of DLP in the polymerization of ceramic and metal-loaded suspensions, enabling the fabrication of ceramic and metal components after proper debinding and sintering. Such flexibility increases the potential of DLP for different applications, ranging from dental implants and bone scaffolds to smart biomaterials for soft robotics, smart wearables, and microfluidic devices.

The objective of this thesis is to highlight DLP novelties and peculiarities in contrast to other AM technologies, including: (a) a high-resolution DLP source, a simple and inexpensive device that nonetheless allows reaching printing resolution of few microns in the printing plane; (b) mask projection-based approach, which ensures a fast printing compared to multistep mask-

based processes or laser-based manufacturing technologies, requiring time-consuming scanning in XY plane; (c) availability of a variety of materials offering DLP a potential of manufacturing of functional and non-functional parts; (d) possibility of biomaterial printing, due to low-power DLP source; and (e) low cost and user-friendliness of printers makes it available even to inexperienced users. Further, the next chapters cover various aspects of the DLP printing process including material preparation, advancements, and provide insight into light-matter interaction during printing.

1.2. AM steps

Additive manufacturing of a 3D object can be divided into three major steps: (i) designing, (ii) printing, and (iii) post-processing [19]. In the designing step, the desired 3D shape is created using CAD (computer-automated design) software (Figure 1.3 a), such as TinkerCAD, Fusion 360, SOLIDWORKS, AutoCAD, etc. In a classic manufacturing process, the designed geometry is converted into STL (Standard Tessellation Language) format [20] and sliced into 2D images (layers) by slicing software (Figure 1.3 b). The output file from the slicing software contains the geometrical information related to the sliced layers. Printing parameters such as exposure time, which depend on the technique and the specific process, are typically defined in the printer software before printing. Currently, 3D printers, based on different manufacturing technologies use G-codes generated by the printer software and are compatible with different formats of 3D files. These G-codes contain all the information required for printing, including printer movements, sliced images, exposure time, temperature, etc. During printing (second step), 2D slices (layers) are printed one after the other, until the final object emerges on the build head as a compact stack of layers (Figure 1.3 c). This manufactured object, also called ‘green body’ (Figure 1.3 d) at this stage, is then removed from the build head and subjected to post-processing (third step). Post-processing required to remove the excess raw material or impart the final finishing (Figure 1.3 e) may depend on the specific AM technology, the material used, and the final application for produced parts.

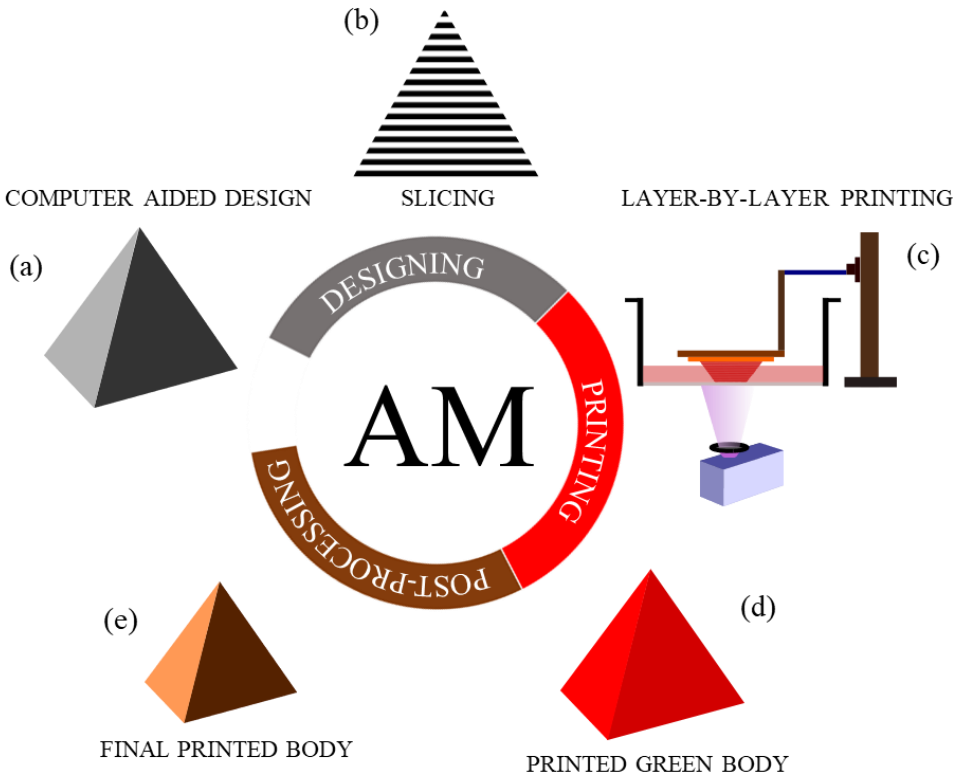

Figure 1.3 Step-by-step manufacturing process in AM. Designing step consists of CAD modeling and slicing of a 3D object (a & b). These sliced layers are printed one layer after the other in the printing process (c). The printed body in green form (d) is then subjected to post-processing before emerging as a final printed body (e).

1.3. Additive manufacturing technologies

A variety of AM technologies have evolved in the last forty years, and the categorization is not unique. Process- [21] and material-based [22] classifications are more frequently used. A brief description of the most widely used manufacturing technologies [23] is provided here while comparing their key properties (Table 1.1).

1.3.1. Selective Laser Sintering (SLS)

SLS is a powder bed manufacturing technology (Figure 1.4 a). In this technology, a computer-guided, high-energy laser source is used to sinter particles [24]. The laser scans the powder bed surface, replicating the sliced 2D image to form each new layer. The building tank that contains the leveled powder and partially printed part subsequently moves to a distance equal to layer thickness, and a roller deposits a new even layer of fresh powder for further laser scan. Oxygen-sensitive materials are usually processed under an inert atmosphere, such as argon or nitrogen [25,26].

Selective laser melting (SLM) and direct metal laser sintering (DMLS) are derived from SLS and based on different binding mechanisms: solid-state sintering, liquid-phase sintering, partial melting, and full melting [27]. Solid powder and powder with binders are used as materials in these technologies.

1.3.2. Electron Beam Melting (EBM)

EBM is similar to SLS, the main difference being the energy source. Instead of a laser, an electron beam controlled by magnetic lenses is used to scan and melt the powder layer. This system requires a high vacuum (10^{-4}-10^{-5} m bar) because of the high reactivity of metal and alloys with gases like oxygen and

nitrogen [28]. The build head, which is a metallic tray, should be the same or similar material of powder to avoid impurities and produce high-performance 3D objects [29]. Cooling is performed at the end of the process using an inert gas.

1.3.3. Laser Engineered Net Shaping (LENS)

LENS is an AM technology used to produce high-density metallic/ceramics parts by directed energy deposition (Figure 1.4 b). Differently from the powder bed technologies, the powder material is air-blown (inert atmosphere) through a nozzle into a melted pool on the substrate forming a layer. A scanning laser source is used to form a melted pool by heating the powder material, which solidifies after cooling. The technology gives freedom to use different powders in different ratios, opening exciting research opportunities for metallurgy [30,31].

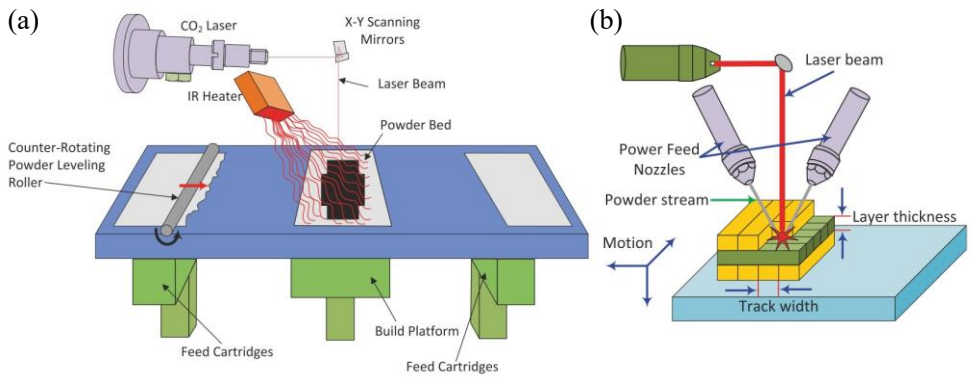

Figure 1.4 Schematic of (a) powder bed fusion and (b) direct energy deposition process (adapted and reprinted from ref. [32] with permission from Springer Nature).

1.3.4. 3DP or binder jetting

In this process, a binder material is sprayed by a nozzle over a power bed following the path of 2D sliced images provided by the slicing software (Figure 1.5 a). The process is simple and does not require any complex machine or post-processing. As such, this technology is mainly used for rapid prototyping and less indicated for building functional components. For functional parts, post-processing steps like sintering, infiltration of other metal powder, and then finishing are needed [33,34].

1.3.5. Laminated Object Manufacturing (LOM)

LOM is a technology where the starting raw material (paper, metal sheet, plastic, or synthetic fibers) is used in solid form (Figure 1.5 b). The material must be a sheet coated with an adhesive. A guided laser source cuts the sheet according to the 2D slices. The sheets are then laminated, one after another, by pressing with a heated roller at optimized temperatures [35,36].

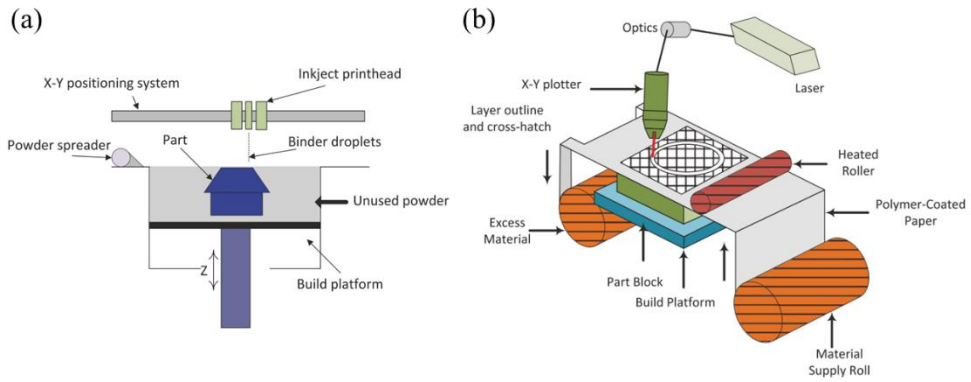

Figure 1.5 Schematic of (a) binder jetting and (b) sheet lamination process (adapted and reprinted from ref. [32] with permission from Springer Nature).

1.3.6. Fused Deposition Modeling (FDM)

FDM is an extrusion-based manufacturing technology where the material filament is liquified by heating just above the melting point, using a heating device (Figure 1.6 a). The material extruded from the nozzle is deposited cross-sectionally to print one layer at a time. The technology can produce functional prototypes and models, but it is unsuitable for high-resolution manufacturing objects. The major disadvantages of this process are the long building time and the possibility of interlayer delamination [37,38].

1.3.7. PolyJet (PJT)

PJT technology is based on jetting/spraying of the material, consisting of an acrylate-based photopolymer, in tiny droplets onto the build heads (Figure 1.6 b). A roller, then, makes the liquid polymer surface even, and subsequently, UV light cures the layer. The advantage of this technology is the possibility to manufacture parts using different photopolymers [39,40].

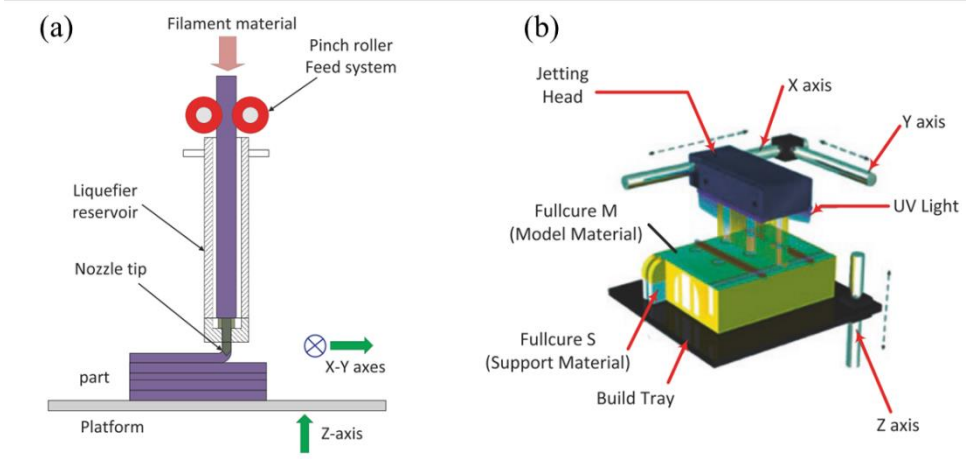

Figure 1.6 Schematic of (a) material extrusion and (b) material jetting process (adapted and reprinted from ref. [32] with permission from Springer Nature).

1.3.8. Stereolithography (SLA)

(SLA) is one of the first AM technologies categorized under the vat polymerization process (Figure 1.7 a). A UV laser source is used to polymerize liquid acrylate/epoxy-based resin inside the vat, by scanning the laser over in the XY-plane, to polymerize one layer, pixel by pixel. The vertical movement of the build head with respect to the vat allows the liquid resin to fill the space for consecutive layer formation [41,42].

1.3.9. Digital Light Processing (DLP)

DLP is an advanced version of SLA, where the laser source is replaced by a digital light projector (Figure 1.7 b). This radiation source projects one 2D image at a time and polymerizes the exposed liquid resin layer locally. The significant advantage is that one complete layer is cured during each exposure, reducing the time needed by the laser source used in SLA, where raster in a 2D plane is performed. The materials used in both SLA and DLP can be the same, and the post-processing methods such as removal of the support structure, debinding, and sintering are similar [43,44].

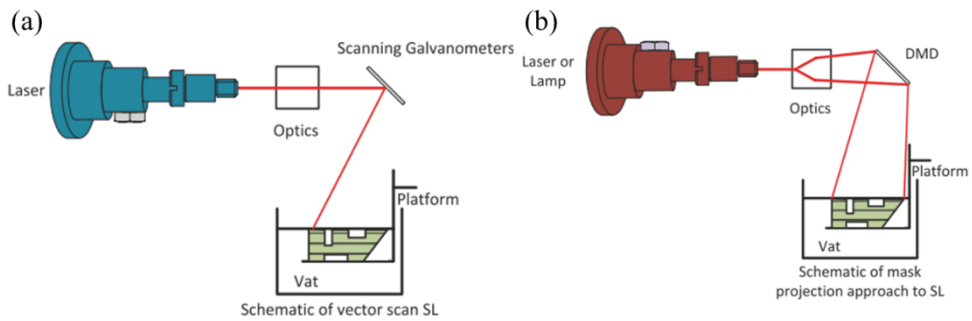

Figure 1.7 Schematic of vat polymerization processes: (a) Stereolithography and (b) digital light processing (adapted and reprinted from ref. [32] with permission from Springer Nature).

AM Technology	Process	Power Source	Material	Accuracy and Finish	Post-processing	Application	References
SLS	Powder bed fusion	Low power laser	Polymer, Ceramic, Metal powder	Not very accurate/ Standard Finish	Sintering, infiltration	Prototypes, casting	[24,27]
SLM		High power laser	Metal powder	Surface quality limited by size of particles	Infiltration	Tools, functional parts	[25,26]
EBM		Electron beam	Metal powder	Low surface quality but with high density	Infiltration	Tools, functional parts	[28,29]
LENS	Direct energy deposition	Laser	Metal powder	Poor surface quality	Cleaning	Biomedical: bone implants and scaffolds	[30,31]
3DP	Binder jetting	Chemical reaction of the binder	Liquid binder, starch-based powder, ceramic	Low z-resolution	No chemical post-processing, need polishing for a smooth surface in the z direction	Prototypes, casting	[33,34]
LOM	Sheet lamination	Laser or blade	Paper, plastic, metal, ceramic, fiber	Less dimensional accuracy, delamination is common	Polishing, Painting	Prototypes, non-functional parts	[35,36]
FDM	Material extrusion	Heating element for melting filament	Plastic, ceramic or metal filled filaments	Low z-resolution	Finishing for surface smoothness	Modeling, prototyping	[37,38]
Polyjet	Material jetting	UV source	Photopolymers	High resolution, different materials, low mechanical strength	Removal of the support structure	For prototypes, latest research claims end to use as well	[39,40]
SLA/DLP	Vat polymerization	UV Laser (SLA)/DLP	Photopolymer, suspension	Most accurate / Excellent surface finish	Support structure removal. Thermal treatment	Prototypes, casting, end to use parts	[41–44]

Table 1.1 Comparison of different AM technologies.

2. Digital Light Processing and Applications

2.1. Digital Light Processing

DLP is named after the digital light projector [45], based on digital micro-mirror device (DMD) technology [46]. The photosensitive resin is polymerized locally and forms a stack of layers by a back-to-back projection of images of 2D layers from the DLP source. These images are an ensemble of light and dark pixels created by micron-sized mirrors on DMD, which determine the XY-plane resolution of the polymerized layer. The technology shares the same fundamental steps of manufacturing as other AM technologies, i.e., designing, printing, and post-processing. A brief representation of the complete DLP process is illustrated in the flowchart in Figure 2.1. Pre-printing steps may change, based on the specific CAD and slicing software. For example, some slicing software can generate support structures, or can repair critical issues in the .stl file, such as holes or

intersections.

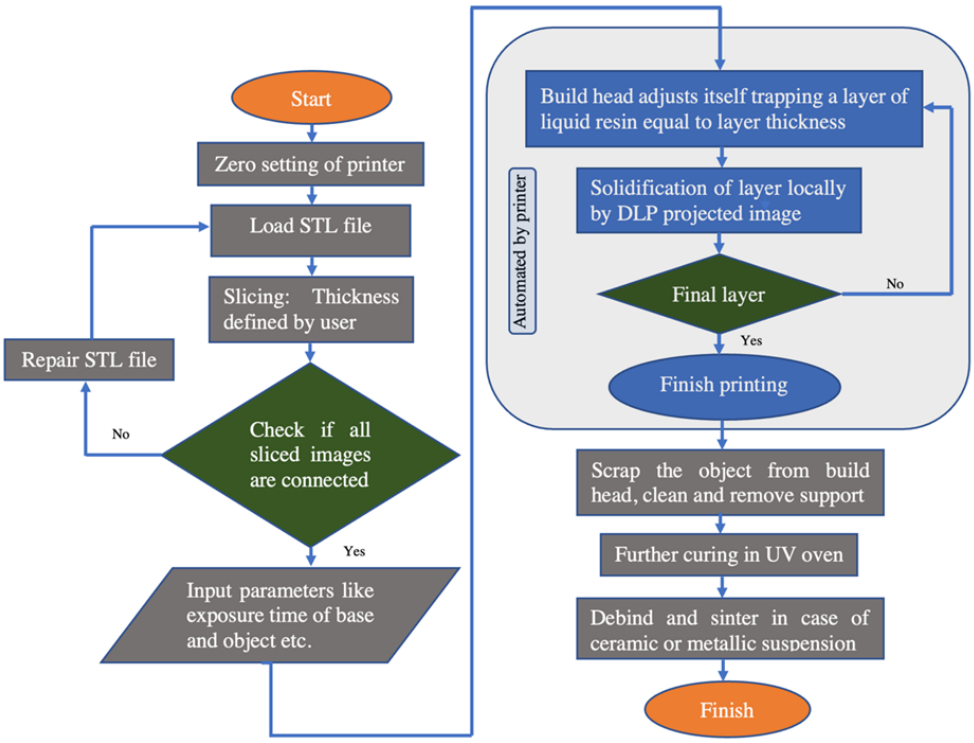

Figure 2.1 Schematic flow diagram of a DLP printing process.

In principle, the printing process is similar for all DLP-based printers. However, geometric configurations may differ. Two main geometric configurations [47] are usually adopted in DLP: bottom-up and top-down. In the bottom-up configuration (Figure 2.2 a), the build head is dipped in the resin container (vat); the immersion height (i.e., the distance from the head to the vat base) is equal to the desired layer thickness. Since the bottom of the vat is transparent, it allows the UV light to pass through and project the image onto the thin layer of liquid resin, trapped between the vat base and the build head. The trapped liquid resin layer is polymerized and remains attached to the build head after a defined exposure time. The upward movement of the build head helps in the separation of the polymerized layer from the vat base. As the build head moves up, the vat base is recoated with a fresh liquid layer of

unpolymerized resin. Differently, in the top-down configuration (Figure 2.2 b), the DLP source is mounted at the top of the vat, and the build head is completely immersed into the resin container. The build head depth is equal to the desired layer thickness. This thin layer over the build head is then cured by the DLP source mounted above the vat. After curing, the build head with adhered first layer shifts down inside the container to a distance equal to layer thickness. A recoating device is used to fill the void space with a fresh layer of resin.

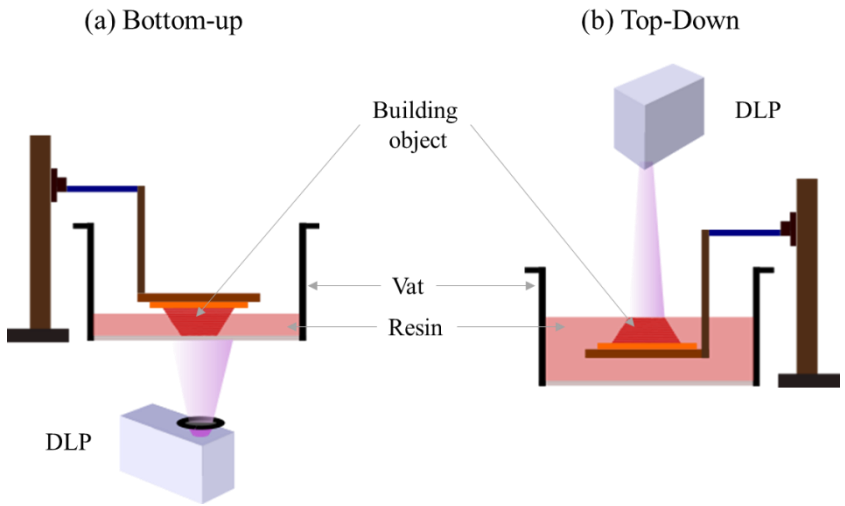

Figure 2.2 Two different geometries used in DLP-based printing technology. (a) Bottom-up: The object is built inverted on the build head by polymerizing the layers exposed from the bottom of the vat. (b) Top-down: The object is manufactured on the build head by polymerizing the layers exposed from the top of the vat.

Each configuration presents its advantages. The bottom-up configuration requires less fresh resin in the vat and can print small objects with less resin in the container. The vacuum developed with the upward movement of the build head facilitates the recoating process even for the viscous resins. However, the separation of polymerized layers from vat base media is a critical step during the printing process. Flexible films [48], coated films [49,50], and separation movements [51,52] have been introduced to overcome the adherence of polymerized film with the vat base. Differently, in the top-down configuration,

a higher amount of less viscous resin is required. This aids the adjustment of the build head inside the vat with a resin layer on the top. However, printers equipped with a recoating device/scraper make the coating easier even for highly viscous resins or resin filled with solid particles. An advantage of the top-down configuration is that there are no issues with adherence between layer and vat base media, as the resin is polymerized at the free surface, in contact with air. However, the contact of environmental oxygen to the resin surface may inhibit the polymerization on the projection site. Consequently, both configurations have pros and cons, and commercial printers on the market exploit both configurations.

Several advancements in the technology have been introduced recently to overcome the abovementioned limitations, including single material restriction inside vat in both configurations. Multi-vat DLP systems or material swaps enabled the fabrication of multi-material mechanical, electrical and bio-functional components [43,53,54] (Figure 2.3 a). Another approach for manufacturing multi-materials is the integration of two different manufacturing technologies. Peng et al. demonstrated the printing of multifunctional structures and devices using an integrated DLP and direct ink writing (DLW) system [55] (Figure 2.3 b), whereas Nguyen et al. presented the integration of DLP with binder jet printing (BJP) in their research for metal components manufacturing [56].

Other methods have been implemented in DLP for improving the process. The time-consuming and critical post-polymerization detachment from the vat base in bottom-up DLP was eliminated by Continuous Liquid Interface Production (CLIP) method (Figure 2.3 c): Janusziewicz et al. introduced an oxygen preamble window, which generates a continuous liquid interface, also called “dead zone”, by inhibiting polymerization between the polymerized resin and the vat base [57]. The method not only facilitates an increase in

manufacturing speed but also limits staircase effects in manufactured objects. In another similar approach, high-area rapid printing (HARP, see Figure 2.3 d), this dead zone is replaced by mobile immiscible fluorinated oil at the interface, which reduced the adhesion between polymerized resin and the vat base [58]. Tomographic volumetric additive manufacturing (Figure 2.3 e) is another extension of vat polymerization-based technologies after SLA and DLP, where liquid photopolymer is selectively polymerized by projecting two-dimensional images inside the material volume [59]. Based on the principle of computed tomography (CT), collective energies of propagated images at multiple angles through the material help in getting desired geometry in a shorter time than layer-by-layer methods. Similar to volumetric additive manufacturing, photopolymer is cured freely inside a vat using a laser beam in two-photon polymerization (2PP) technology [60] (Figure 2.3 f). The minimum identity of freely cured photopolymers (called “voxel”, which stands for “volumetric pixel”) allows the manufacturing of micro-objects with nanometric features [61].

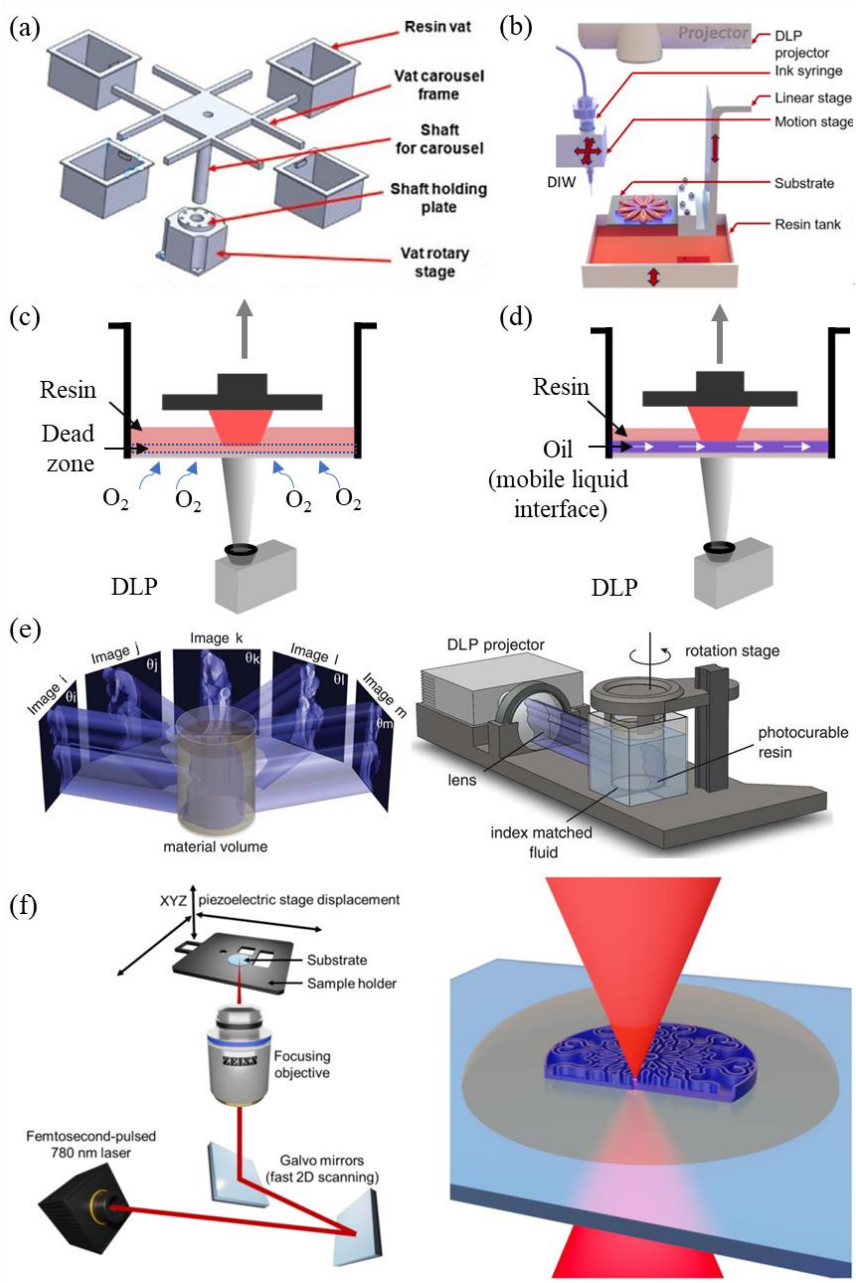

Figure 2.3 Advances in DLP and similar vat polymerization technologies: (a) Multi-vat system for switching photopolymers for multi-material printing (adapted and reprinted from ref. [62] with permission from Elsevier. (b) Multi-material printing with hybrid printing technology using DLP and DIW (adapted and reprinted from ref. [55] with permission from Elsevier). (c) Schematic of CLIP method. (d) Schematic of HARP method. (e) Vat polymerization-based volumetric additive manufacturing (adapted and reprinted from ref. [59] with permission from Science). (f) Two-photon polymerization (adapted and reprinted from ref. [61] licensed under a Creative Commons license, CC BY 4.0)

2.2. Post-processing

As briefly discussed in the previous chapter, post-processing is the last step in AM to produce a desired 3D object. One or more of the following steps may be required to: (i) clean off the residue liquid polymer from the surface, (ii) remove the support structure, (iii) polish the green body to obtain a smooth surface, and (iv) thermally treat the green body for producing dense solid object. Several finishing methods, such as vibratory finishing [63], hot cutter machining, optical polishing, micromachining process, etc., have been developed to obtain the required surface finishing [64]. Hereafter the most common post-processing phases used in DLP or SLA-based manufacturing are presented.

2.2.1. Cleaning of the green body

In both geometries, bottom-up and top-down, used in the DLP process, the printed object emerges from the unpolymerized resin vat, with resin residues on the printed structure. This residual resin needs to be cleaned off soon after the printing process to avoid gelation by the natural light and complete curing in further process. Generally, the green body is rinsed and sonicated in solvents like isopropyl alcohol, ethyl alcohol, or acetone. However, the high reactivity of these solvents may wear off the printed part surface in case of overexposure to the solvent. Keeping green parts inside these solvents also generates swelling, which affects the final geometry. Tripropylene glycol monomethyl ether (TPM) and dipropylene glycol monomethyl ether (DPM) are other classes of solvents, which are less volatile and flammable compared to alcohol-based solvents [65].

2.2.2. Removal of the support structure

In the manufacturing of complex 3D objects from liquid or powder materials, support structures are often required [66]. Changes in the printing orientation may mitigate the necessity of support structures [67]. However, for structures such as overhangs or horizontal bridges, the use of supporting structures is almost inevitable. The slicing software enables automatic or manual generation of supports. Printed supports are removed from the green body before UV curing. Incomplete polymerization of the resin during printing makes removal steps easier. At present, multiple slicers allow different parameters for support structures and 3D objects, making the removal process easier. In general, most of the resins are fragile after the polymerization, thus it is easy to break off thin support from the bulk object.

2.2.3. UV curing

For the polymerization of the liquid polymer layer with UV radiation, the exposure time is carefully chosen. In case the exposure is too short, the photopolymer remains under-cured, potentially leading to dissolution in solvents during cleaning. On the opposite, if the exposure to UV is too long, the photopolymer tends to achieve complete polymerization, leading to high adhesion between the resin and the vat base: over time, this may damage the vat base. Therefore, an ideal exposure time is needed for optimal polymerization of layers to prevent under- or complete polymerization. Indeed, the post-curing of polymerized parts is done in a UV oven to ensure complete polymerization to achieve better mechanical properties [68]. However, there is a limitation related to thicker walls of manufactured parts, across which the radiation cannot penetrate and reach the inner part. This leads

to anisotropy in the degree of polymerization across the wall resulting in deformation of shape while post-curing.

For suspensions, where the polymerized resin provides a matrix for solid particles (ceramic and metal), further post-processing steps are performed to remove the organic part during the debinding step, and to consolidate the particles together in the sintering step for manufacturing a dense solid part. These steps are further detailed in the following sections.

2.2.4. Debinding

During debinding, the polymerized resin (also referred to as binder), which provides the matrix to the solid powder after polymerization, is decomposed and evaporated at high temperatures in controlled atmospheric conditions. Thermogravimetric analysis (TGA) and Fourier transform infrared (FT-IR) spectroscopy are utilized to determine the optimum heat cycle for debinding. Previous studies reported that mass loss typically starts at around 200 ºC, and nearly complete organic material decomposition occurs before ~600 ºC [69,70]. Physical properties such as powder size distribution and amount of filler material also affect the debinding process. Wang et al. reported that debinding is a two-stage process: low-temperature debinding (200-300 ºC) and high-temperature debinding (300-600 ºC). In low-temperature debinding, the binder starts to melt, and decomposed gas flows from inside to outside via formed interconnected pores [71]. In high-temperature debinding, carbon is oxidized after binder decomposition, followed by a release of expanded CO_2, forming cracks. Slow ramps and long temperature hold may thus be required, resulting in a long debinding process (of the order of 100 hours), to optimize the process and avoid cracks, especially for ceramics. In a study by Liu et al., a fast debinding process has been reported for producing silica glass [72].

Penetration tunnel formed by early-stage evaporation led material out of the green part rapidly while reducing debinding time by factor three. Removal of the organic resin causes shrinkage and porosity in the debinded object. This porous, fragile 3D structure with loosely bonded solid particles needs further treatment for manufacturing dense solid objects, i.e., sintering (Figure 2.4).

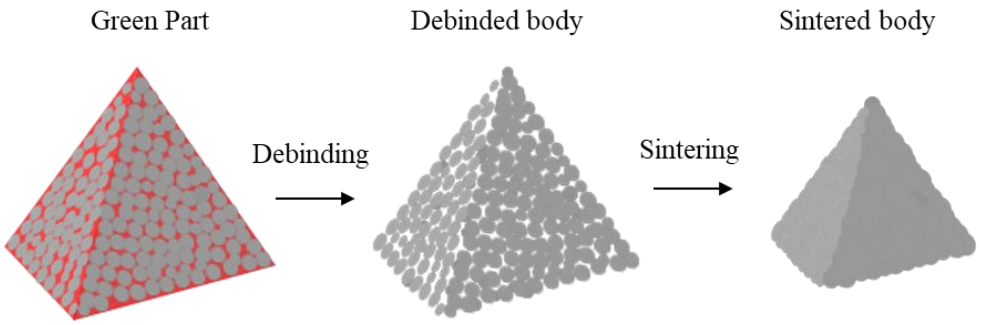

Figure 2.4 Thermal treatment of the green body prepared with suspension-based resin. The photopolymer provides the organic matrix to the solid powder (left) in creating the structure. Later, this organic part is burnt in debinding process (middle), leaving only powder that is fused in the sintering process (right).

2.2.5. Sintering

Sintering is the final stage of post-processing, where solid particles are compacted at high temperatures, producing a denser solid structure to improve mechanical properties and product quality. However, incomplete healing from the defects generated during debinding step may hinder reaching higher densities. Sintering time, temperature ramp, and hold time at constant temperature affect the intergranular bonding between particles. Low heating rates produce high relative density at a given temperature. Sintering is normally divided into three stages: (i) an early stage where no shrinkage is observed due to the merge and recrystallization of crystallites; (ii) an intermediate stage, during which particles start to adhere and grain growth is

observed; (iii) a final stage, during which micropores close and densification finish [73].

Various studies on the ceramic parts sintering produced by DLP, such as zirconia ZrO_2 [74,75], alumina Al_2O_3 [76], titania TiO_2 [77], silica SiO_2 [72] have been conducted (Table 2.1). Metal sintering still needs to be systematically explored in the context of the DLP process, as only a few examples are available, e.g. stainless steel [56] and copper [78,79].

Table 2.1 Sintering temperature for different materials from the literature.

Powder	**Particle size (µm)**	**Max. Sintering Temperature (°C)**	**Relative density (%)**	**Reference**
Zirconia (ZrO_2)	-	1600	99.5	[75]
Alumina (Al_2O_3)	0.2 **(d_{50})**	1650	99.3	[76]
Titania (TiO_2)	1-2	1350	-	[77]
Silica (SiO_2)	-	1250	-	[72]
Stainless Steel (SS-420)	55/22	1250	97.5	[56]
Copper (Cu)	22 **(d_{50})**	1050	94	[79]
d_{50} is the value of the particle diameter at 50% in the cumulative distribution.				

2.3. Applications

AM has been significantly developed from prototyping non-functional parts since it was introduced in the early 1980s. In the last decade, all manufacturing technologies have reached a significant landmark due to the development of innovative materials [80,81] for manufacturing (Figure 2.5). From micro-structures to macro fabrication, AM is taking the place of conventional manufacturing technologies in many sectors owing to its ability to generate complex, lightweight structures with high strength [82]. Aerospace, automobile, and medical sector [32] were some of the early adopters of AM because for these reasons. At present, a distinct AM technology [19] is chosen for a specific application based on the choice of raw material. Within this framework, DLP technology is used to produce functional and non-functional parts in various application parts with unforeseen resolution in AM.

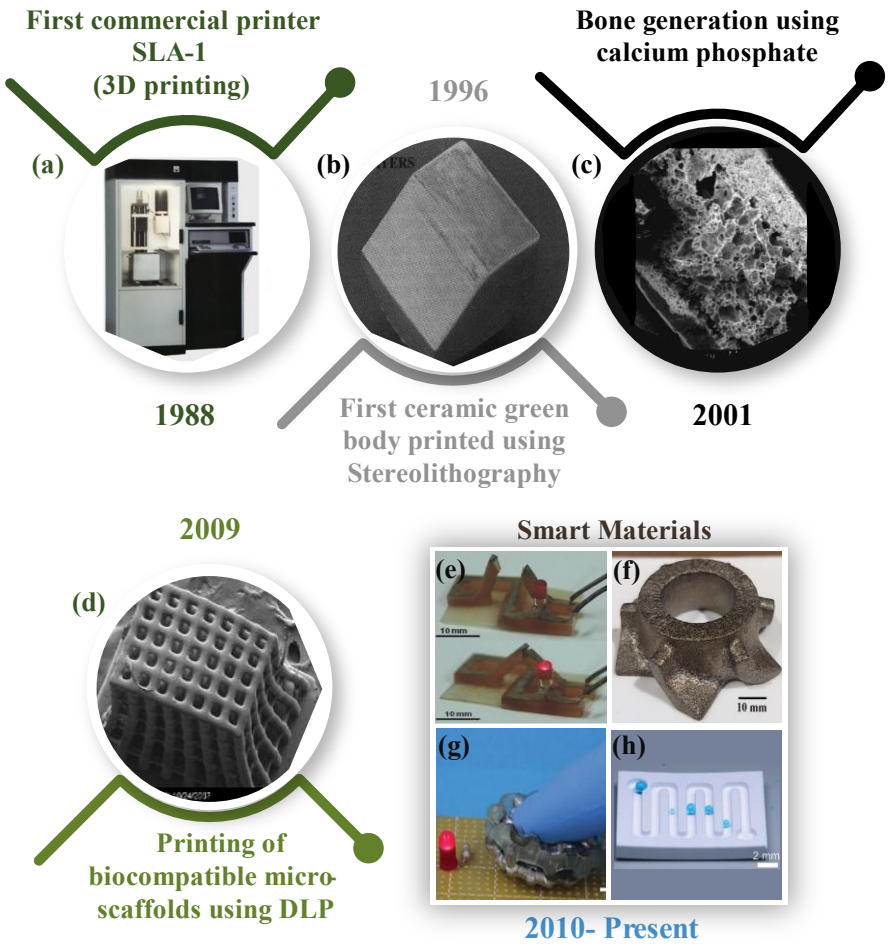

Figure 2.5 Timeline of the development of materials, applications and, stereolithography technology. Block (a), (b), (c), and (d) are adapted and reprinted from Ref. [83] (with permission from Elsevier), [84] (with permission from John Wiley and Sons), [85] (with permission from John Wiley and Sons) and [86] (with permission from Elsevier), respectively. Block (e), (f), (g), and (h) are adapted and reprinted from [87] (with permission from John Wiley and Sons), [56] (with permission from Elsevier), [88] (with permission from John Wiley and Sons) and [89] (licensed under a Creative Commons license, CC BY-NC 4.0), respectively.

In 1995, during the early development of stereolithography-based techniques, Dickens et al. reported 100 µm of minimum layer thickness with 50 µm accuracy for rapid prototyping [90]. Kim and Hwang et al. reported a resolution of 76±14 µm in dental prototypes using a DLP printer with 70 µm of XY resolution and 75 µm layer thickness [91]. Among projection-based

technologies, Janusziewicz et al. introduced the CLIP method of AM using 0.4 µm slice thickness. The advancements in dimensional accuracy with high precision of manufactured objects made DLP the best choice to create prototypes and casts [57].

Biocompatibility of ceramic powders, such as zirconia [92] and alumina [93], opened the way to the use of DLP-printed ceramics for medical applications. The technology is popular among dentists to customize orthodontic models and develop implants, bridges, and teeth [94]. Apart from dentistry, ceramic-based DLP manufacturing technology is also used for producing bone scaffolds for bone regeneration. Christina et al. used tricalcium phosphate ceramic powder to produce bone scaffolds using DLP [95]. In another work by Liu et al., hydroxyapatite (HA) bioceramic was used for manufacturing bone scaffolds [96]. In recent works, the manufacturing of transparent glass has been reported by low-cost DLP technology using ceramic-based resin [97,98]. In a work by Rodríguez et al., fuel cell components have been manufactured using yttria-stabilized zirconia-based feedstock [99]. High melting point, working temperature, and lightweight with excellent mechanical properties allow ceramic parts for myriad applications [100–102].

Another application of the low-power source DLP technology is the bioprinting of living tissues [103] using functional biopolymers and synthetic polymers [104]. In a recent study by Kim et al., UV-curable silk fibroin bio-ink has been developed to generate organ structures [105]. Lu et al. used an acrylate-based photocurable resin as a scaffold, and murine bone marrow-derived cells incorporated on fibronectin functionalized scaffolds using DLP [106]. Review articles by Zhu et al. and Vincula et al. demonstrated extended applications and progress in tissue engineering using AM technologies [107,108].

With the advancement in materials for DLP, researchers also introduced smart printable materials, such as elastomers. Elastomers have good mechanical properties and can provide thermal and electrical insulation and, in some cases, self-healing capabilities, which is interesting for electronics, wearables, soft robotics, etc. Traugutt et al. used the DLP technology for manufacturing complex liquid crystal elastomer (LCE) structures for strain energy dissipation [109]. In another work by Patel et al., DLP printed the so-called stretchable and UV-printed (SUV) elastomer, with a reported 1100% strain. The printed object can be used for soft and deformable structures [88]. Zhao et al. reported the manufacturing of silicone elastomers with 1400% strain. The geometry is then applied with carbon nanotubes-doped hydrogel for possible application in stretchable electronics [110].

DLP has also been exploited with composite-based photopolymers. Photopolymers reinforced with glass fibers, graphene nanoparticles, silicon carbide, zinc oxide, and multi-walled carbon nanotubes are used for manufacturing 3D objects with different functionalities [111]. Mu et al. introduced multi-walled carbon nanotube (MWCNT)-based polymeric composites to produce electrically conductive objects, which can be used as capacitive sensors, stretchable circuits, and shape memory devices [112]. Yunus et al. presented DLP-printed nanocomposite-reinforced samples using copper, magnetite nanoparticles, and carbon nanofiber via aligning and condensing conductive nanoparticles for producing embedded electronic components [113].

Wu et al. presented the printing of a novel acylate-based shape memory polymer via DLP [114]. Zhou et al. printed a piezoelectric nanogenerator for self-power sensor application using a barium titanate polymer-based composite [115]. Zhu et al. mentioned DLP printing of healable and recyclable

polymers for various applications [116]. High-resolution printing DLP technology also enables the manufacturing of microfluidic devices [117,118]. For sensing applications, DLP has been exploited for the fabrication of optical devices such as optical fibers [119] and lenses [120]. Recently, the technology has been used to fabricate superhydrophobic objects with pillar structures [89,121].

3. Photopolymers and Light-Matter Interaction

3.1. Photoinitiating systems

A simplified system of photopolymer (resin) [122] contains oligomers, monomers (mono- or poly-functional), and a small amount of photoinitiator (PI). Oligomers are long chains of molecules that provide the backbone to the photoinitiating system, while monomers are utilized as diluting agents. Resin exposure to the light source activates the PI, which generates reactive species, free radicals, or reactive ions. These species react with oligomers and monomers, enabling the formation of long chains leading to photopolymerization [123,124]. Monomers and oligomers alone are not able to produce enough reactive species for polymerization. Hence, a small amount of PI is needed for initiating the process [125]. To increase the PI yield, more complex photoinitiating systems are developed, including co-initiator, inert dyes, photosensitizers, etc. [126]. Furthermore, the high reactivity of resins to radiation allows the addition of fillers (ceramic or metal) to the base resin formulation to form a suspension [42] (Figure 3.1).

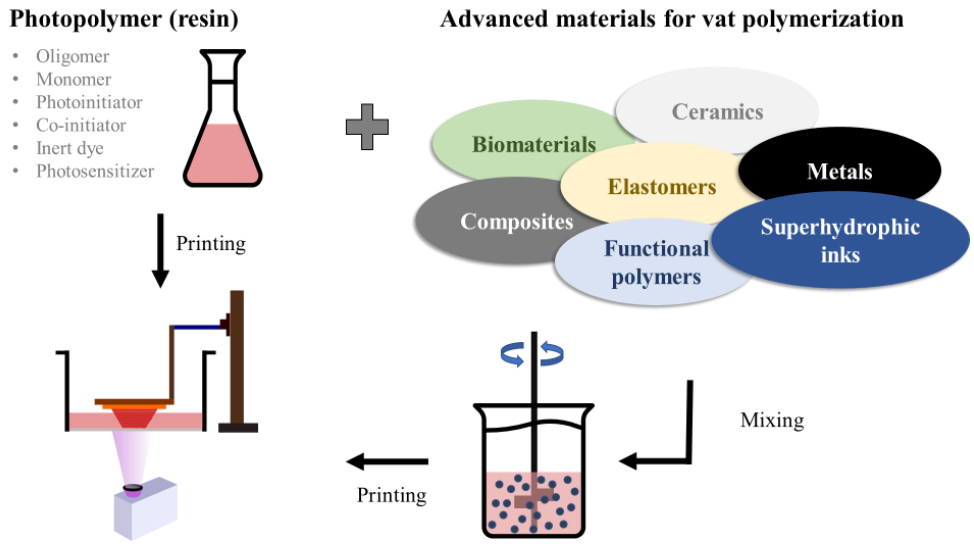

Figure 3.1 Schematic illustrating material composition for vat polymerization process, which can be either a pure resin or advanced material, such as ceramic or metal suspensions, which can be added and mixed with the resin before printing.

The proportion of the components inside a photopolymer affects the printing process in several ways. Specifically, oligomers with a small number of repeated units have a higher molecular weight than monomers. A high proportion of oligomers increases the mechanical strength of printed objects, but also increases the liquid photopolymer viscosity, decreasing the flowability and hindering the recoating process in the vat. Conversely, increasing the monomer percentage reduces liquid viscosity, but increases the polymerization time to achieve similar mechanical properties. As such, the proportion of oligomers and monomers is essential to tune the resin viscosity, the exposure time for polymerization, and the final properties of the printed object [127]. The viscosity of the photoinitiating system also depends on fillers, which is detailed in section 3.2. In general, the steps for polymerization are the same for all the photopolymers while interacting with the radiation, but the mechanism is different based on the photoinitiating system which is detailed in the next sections.

Photopolymers are categorized based on photoinitiating reactions: (i) free radical and (ii) ionic-based [125]. These systems differ by the produced reactive species by PI, radicals, and reactive ions, as they are exposed to a light source, starting chain reactions leading to photopolymerization. Both free radical and ionic-based processes consist of three steps, schematically represented in Figure 3.2: (i) initiation, (ii) propagation, and (iii) termination. Initiation starts with the absorption of UV radiation by PI generating the reactive species. These species react with oligomers and monomers, promoting the formation of long chains during the propagation step. The reaction terminates either of the three causes, recombination, disproportion, or occlusion [103].

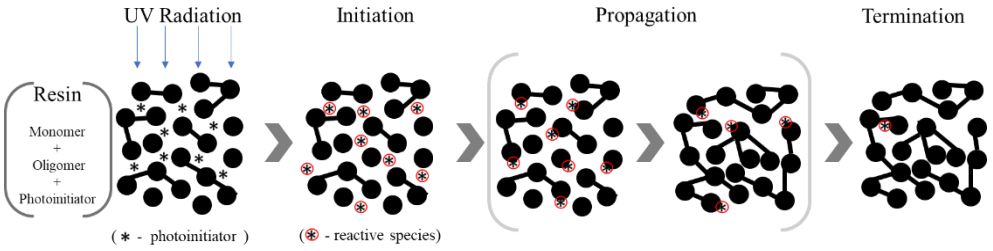

Figure 3.2 Schematic of the polymerization process of a photosensitive resin. The photoinitiator (black star) generates reactive species (star in a red circle) during the initiation process, as soon as the photosensitive resin is irradiated by UV light. The reactive species react with monomers and oligomers and start photopolymerization in the propagation step, followed by the termination step resulting in the polymerization of the liquid photopolymer.

Free radicals can crosslink acrylate, styrene, and thiol-ene-based monomers, to form a long chain responsible for free radical polymerization. This process is fast and terminates in the absence of radiation [128]. Differently, ionic species induce ionic polymerization of another category of monomers such as ketones, aldehydes, heterocyclics, etc., which are not polymerized by free radicals [129]. Cationic polymerization is more widely used in the latter

polymerization system, while it needs more exposure time than radical polymerization and continues even after the removal of the light source.

3.1.1. Free radical system

In these photoinitiating systems, free radicals are generated from the photoinitiator after exposure to light radiation [128]. Acrylates (di- or multifunctional) (highly reactive) are the main choice for these kinds of formulations. Unimolecular type I and bimolecular type II are two kinds of photoinitiators, with different mechanisms, that are used for producing free radicals (Figure 3.3). Type I photoinitiators undergo homolytic bond cleavage, generating two free radicals after absorbing a photon [130]. Benzil ketals, acetophenones, aminoalkyl phenones, acyl phosphine, O-acyl-α-oximo ketones, R-hydroxyalkyl ketones, and acyl phosphine oxides are widely used compounds under this category. Type II photoinitiators abstract hydrogen or electrons from co-initiator species from their triplet state excited by UV radiation and generate free radicals (Figure 3.3) [123]. Derivatives of benzophenone and thioxanthone are used as conventional type II photoinitiators.

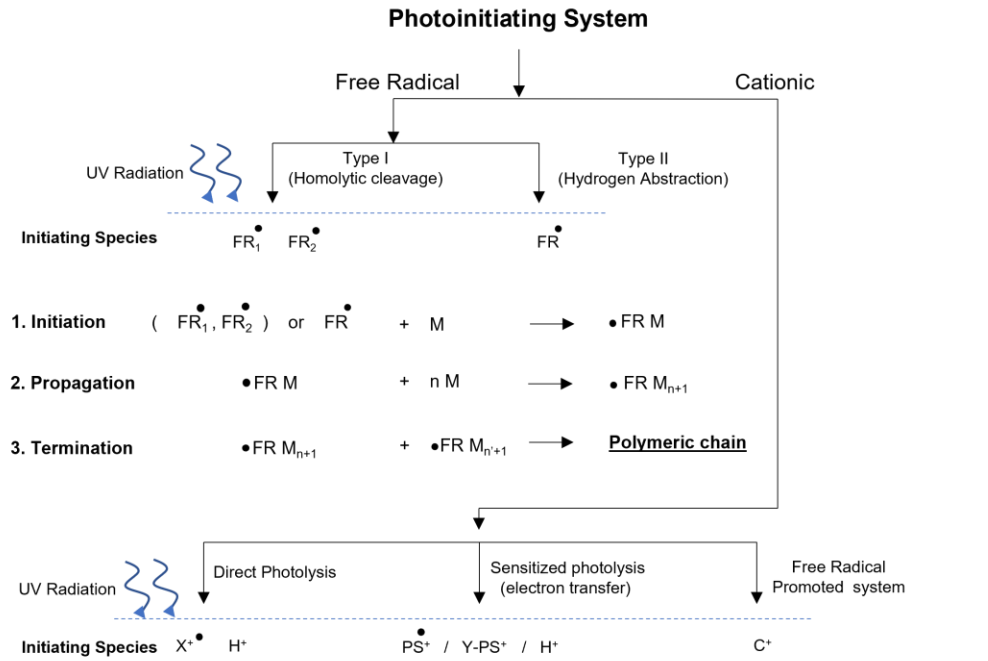

FR	Free radical
M	Monomer
H+	Proton
X+•	Radical cation generated by bond cleavage from onium salt [(X-Y)$^+$A$^-$)]
PS+•	Oxidized photosensitizer by onium salt
Y-PS+	Cation generated by PS+ and radical Y from onium salt
C$^+$	Carbon-centred free radical oxidized by onium salt

Figure 3.3 Photopolymerization process of radical and cationic-based photoinitiating system. Both systems follow the three main steps: initiation, propagation, and termination, but different reaction mechanisms.

3.1.2. Ionic system

In ionic photoinitiating systems, polymerization is promoted by anions in anionic systems and by cations in cationic systems [129]. In anionic polymerization, a nucleophilic group or an electron is transferred to a monomer by anionic PI to initiate photopolymerization. Anionic photoinitiating systems are more challenging to control than radical-based systems; therefore, they are usually considered a secondary option. Cationic photoinitiating systems are more widely used and well-explored for the vat polymerization process. Thus, this chapter is focused more on cationic polymerization in ionic-based PI, along with free radical polymerization.

Onium salts, diazonium salts, and organometallic complexes are the main categories of a cationic PI system [131]. Figure 3.3 depicts the generation of reactive species, i.e., cations from onium salts in three ways: (i) direct photolysis of PI, (ii) sensitized photolysis of PI, and (iii) free radical mediation upon irradiation with light source followed by initiation, propagation, and termination step. In direct photolysis, a radical cation and a proton, generated after the photolysis of the onium salt, react with the monomer during initiation. In the mixture of PI and photosensitizer (PS), initiation can start in three possible ways: (i) radical cation (oxidized PS by onium salt), (ii) cation generated by oxidized PS, and (iii) radical from onium salt, and proton. In the free radical-promoted system, the reactive species are generated by the oxidation of carbon-centered free radicals by the onium salts. Unlike the free radical systems, nucleophilic impurities of the PI system terminate the chain photopolymerization process in cationic systems [132].

3.1.3. Oligomers and monomers

Oligomers and monomers represent the largest component in photosensitive resins. These molecules add together in a chain process, creating a polymer chain after reacting with UV activated photoinitiator. Generally, acylates, mono- and poly-functional, with olefinic double bonds, are chosen in free radical systems. The monomers with two or more (meth) acrylate groups (multi-functionalities) usually work as crosslinkers in this system, linking multiple growing chains together, which affects the final properties of the polymerized part [133]. Compounds like epoxides and vinyl ether, which do not polymerize with free radical photoinitiators, are polymerized with cationic-based photoinitiators; n-butyl acrylates (BA), 1,6-hexanediol diacrylate (HDDA), poly (ethylene glycol) diacrylate (PEGDA), pentaerythritol triacrylate (PETA), 1,4-cyclohexanedimethanol divinyl ether (CHDMDE) are a few examples of acrylate-based monomers commonly used. 3,4 epoxycyclohexanemethyl 3, 4 epoxycyclohexylcarboxylate (EPOX), diglycidyl ether (DGEBA), 1,4-cyclohexane dimethanol divinyl ether (CDVE) [134] works for cationic based polymerization process [57]. Both free radical and ionic photopolymerization have their advantages and disadvantages [135]. In free radical photopolymerization, acrylates are more reactive and polymerize rapidly, but may experience deformations, such as shrinkage and curls, in polymerized parts; conversely, in ionic photopolymerization, epoxy-based resins cure slowly and even after the radiation stops, resulting in lower risks for defects. Epoxy-based resins possess less odor and toxic compounds in comparison with acrylates. Photopolymerization is not affected by environmental oxygen in ionic polymerization as in radical polymerization. Currently, a mixture of acrylate-based and epoxy-based resins is used to formulate optimized resins. However,

a large number of acrylate-based resins are available compared to epoxy-based alternatives.

3.2. Resins and suspensions

During the initial development of stereolithography, the technology was only limited to liquid photopolymers as raw materials. The need to produce solid parts with high mechanical properties and functionalities motivated the researchers to incorporate micro and nano-size fillers inside the liquid photopolymer to cover a variety of applications [111,136]. Ceramic powders were one of the first choices as fillers due to their chemical inactivity with the organic resin, to produce non-functional prototypes.

Moreover, vat polymerization is currently studied as a new forming technique to produce components made of different materials (e.g., ceramics and metals) for many applications, by tuning material mechanical strength, electrical conductivity, biocompatibility, etc. Therefore, the following sections are mainly focused on ceramic-filled photopolymers, as well as the more recent development of printing metal parts using metal powder-filled photopolymers.

3.2.1. Ceramic feedstock

Vat polymerization can be considered a promising process for the net-shape forming of complex ceramic components. Compared to gel-casting and injection molding, net-shape techniques are already mature at an industrial level, as vat polymerization does not require expensive multi-part molds for casting or injection, and allows the realization of complex geometries [137].

DLP technology allows the manufacturing of monolithic ceramic components, either porous or dense. Two types of ceramic feedstock can be distinguished for vat polymerization: Photopolymerized suspensions and photopolymerized preceramic resins. The first type of resin provides a heterogeneous dispersion of solid particles in a mixture of liquid monomers, whereas the latter type is a homogeneous mixture of resins in which the ceramic precursor is present. After printing, the object requires two thermal treatments: debinding (to remove the polymer matrix) and sintering (for material consolidation).

3.2.1.1. Photopolymerizable suspensions

In this case, the ceramic feedstock is a suspension in which the photopolymerized organic matrix and the photoinitiator are mixed with the ceramic powder. This approach of fabricating ceramic parts with photopolymerizable suspension has been developed almost in parallel with the stereolithography technique [84,138,139], but optimizing a ceramic suspension is still a challenge. First, the ceramic filler plays an active role within the suspension, interfering with the penetration of radiation. The main reason is the scattering that is generated by the mismatch of refractive indexes between the ceramic powder and monomer; moreover, scattering depends on the solid content and the size of the powder [140–142]. For this reason, it is easier to control photopolymerization with fillers having a refractive index similar to that of the resin. The optimization of ceramic feedstocks containing materials with a high refractive index such as ZrO_2 and SiC powders (Table 3.1) is still an interesting challenge.

Table 3.1 Physical properties of the reactants and fillers used (data from Ref. [141]).

Product	Density	η (mPa s) at 25 °C	Specific area ($m^2\ g^{-1}$)	d_{50} (μm)	Refractive index *n* (365 nm)
PEAAM	1.15	70	-	-	1.488
HDDA	1.02	7	-	-	1.456
Al_2O_3	3.97	-	1.52	2.3	1.787
Al_2O_3	3.97	-	2.41	1.4	1.787
Al_2O_3	3.97	-	5.74	0.5	1.787
SiO_2	2.26	-	5.31	2.25	1.564
ZrO_2	5.92	-	4.48	0.65	2.249
SiC	3.38	-	0.60	12.25	2.553
					(467 nm < λ < 691 nm)
d_{50} is the value of the particle diameter at 50% in the cumulative distribution.					

Another aspect to be considered in the preparation of ceramic suspensions for vat polymerization is viscosity. To avoid crack formation in the ceramic components during the debinding phase and to limit the sintering shrinkage, it is important to maximize the solid content of the ceramic suspension, usually >40 %vol [139,142,143]. However, the increase of the solid content significantly affects the rheological behavior, from a typical Newtonian behavior observed for pure resins to a shear-thinning behavior for concentrated suspensions [143,144]. On one hand, high viscosity or gel-like behavior makes the suspension more stable, decreasing the sedimentation effect during the photopolymerization process, on the other hand, it reduces the flowability. Indeed, the suspension should have a sufficiently low viscosity, so that a fresh liquid layer can be restored after printing each layer. This aspect is also a function of the device used for printing: the film formation occurs naturally due to gravity, due to the tilting or oscillating movement of the vat (in a bottom-up geometry/configuration, see Figure 2.2, or following the passage of a recoating device/scraper (in a top-down configuration). The suitable viscosity for printing is generally less than 20 Pa·s (at a shear rate of

100 s^{-1} at 25 °C) for devices equipped with recoating devices/scrapers [145] and less than 3 Pa·s [146] with printers without recoating device/scraper. Reactive diluents (often monofunctional monomers) or inert diluents (not participating in the photopolymerization reaction) in the formulation of photopolymerizing suspensions can be used to reduce viscosity [147,148].

The preparation of a well-dispersed ceramic suspension begins with the mixing of the components in the liquid phase: monomers and oligomers. Ceramic powder is commonly incorporated directly into the pre-mix (mixing of monomers and oligomers, dispersing, etc.) using grinding/mixing systems capable of breaking down agglomerates: ball milling and planetary milling are the most common methods [149–151]. Generally, the addition of the photoinitiator occurs only at the end of this phase to prevent unwanted reactions catalyzed by the temperature of the grinding process.

To obtain a high solid content suspension, which, nonetheless, has good fluidity, it is often necessary to add a suitable dispersant to the organic powder-matrix system [146,152,153]. Since the suspensions are colloidal, the interaction between the ceramic particles is relevant and depends not only on the viscosity but also on stability against sedimentation. Dispersant agents are commonly used to increase the repulsion force between particles and limit their agglomeration.

In some studies, the photopolymerizing suspension preparation is obtained in two steps [154–156]. In the first step, the ceramic powder is disaggregated into a highly diluted suspension, in which the dispersant is dissolved; at the end of the process, the solvent (water or ethanol) is removed by using a rotational evaporator or by separation after centrifuge [157]. The obtained ceramic powder is dried and sifted then added to the resin mixture. Wang et al. reported that dispersant adsorption is more effective, and, in particular, the adsorption

phase is not affected by competition by the mixture of monomers [154]. Moreover, with the same solid content, the viscosity obtained by two steps is less than that of the one-step preparation process [155].

In the preparation of photopolymerizing resins, the use of nanometric silica is also possible to manufacture transparent glass components. The presence of monomers, able to create a solvation layer on silica particles, in the resin makes it possible to obtain concentrated suspensions while maintaining low viscosity without additional dispersing additives [158,159]. The feedstock preparation is simple in this case: the nano powder is added in small increments to the monomeric matrix, using a laboratory dissolver stirrer.

3.2.1.2. Preceramic polymer (PCP) resins

The use of photopolymerizing suspensions in vat polymerization may be difficult in some cases due to high viscosity [143]. Besides, certain ceramic powders, in particular the class of non-oxides, are colored and therefore absorb light in the UV-VIS [160] spectrum. To overcome these issues, preceramic polymers (PCPs) offer an alternative strategy. PCPs are organic compounds from which amorphous ceramic materials are obtained, precisely called polymer-derived ceramics (PDC) [161], following thermolytic decomposition. PCPs are polycarbosilanes [162], polysiloxanes [163], polysilazane [164], polysilsesquioxanes [165] and they are precursors of Si-based bicomponent (SiO_2 [166], SiC-rich ceramic), Si_3N_4 [167]) and multicomponent ceramics (SiOC [102,162,168], SiCN [169], SiBCN [170]).

Approaches to this technique are not limited to the use of PCPs with photo-reactive acrylic functionality [168]. Photo-reactive PCPs currently available on the market are still limited; it is, therefore, common to use chemical

synthesis to modify the backbone of PCP to make it photocurable, e.g., commercial silicon [165] and polyvinylsilazane [169] modified with methacrylate groups or by a sol-gel synthesis between 3-acryloxypropyl trimethoxysilane (APTMS) and tetraethyl orthosilicate (TEOS) to obtain a photocurable ink [171].

Some authors used the acrylate-vinyl (allyl) for PCP reticular and multifunctional acrylic monomers [162,167], but also the fast curing of thiol-ene free radical addition in a system composed of polysiloxane with vinyl function and 1,6-hexanedithiol [172]. Other works propose UV-curable blends of multiple PCP [102,173], in which only one PCP participates in the crosslinking reaction, while the others contribute to increasing ceramic yield. Other variants of this technique use filled polysiloxane feedstock. Brinckmann et al. obtained a SiOC-SiC whisker PDC in which the mere addition of 0.5 wt% filler allows considerably limits the shrinkage and improves part stability [174]. Besides, absorbance, in the presence of the filler, may increase by an order of magnitude when compared to the base resin.

3.2.2. Metallic feedstock

Similar to the ceramic-loaded resin, a UV-curable feedstock with metal powder is prepared by incorporating metallic powder into the resin. Acrylates, epoxies, or a mixture of both can be used as a polymerizable resin. However, contrary to most ceramic powder-based feedstocks, metal powder-based feedstocks are dark in color. Therefore, in general, a high-energy source with longer exposure times is needed for polymerization. High-density metal powder is treated with dispersing agents to avoid early sedimentation of the powder and to avoid change in penetration of radiation inside the resin. The powder content is kept high to prevent cracks during the removal of organic

parts in debinding. However, as discussed in the previous section, higher powder content increases the feedstock viscosity, which may not be desirable as it limits the flow of liquid resin for film formation. An increase in the viscosity is also reported as the size of the particle decreases for a given metal concentration. New DLP printers with recoating device/wiping blades and heating elements enable an increase in the powder content. At present, only a few studies [56,78,79,175] have investigated the use of metallic suspension printed with DLP. However, a potential increase in the preparation of metal-based feedstocks can be seen to facilitate DLP technology with the competence to produce metallic parts.

3.3. Light interaction with pure photopolymers

Light interacts with the photoinitiating system to produce reactive species. Polymerization is the result of the interaction between light radiation in the UV-visible range and the photoinitiators in the resin. The radiation energy is converted into chemical energy, generating reactive agents, such as free radicals and ions. Overlapping of the absorption band of the PI and the emission line of the radiation source promotes the electron in the lowest unoccupied molecular orbital (LUMO) to the highest occupied molecular orbital (HOMO). Generally, $n\pi^*$, $\pi\pi^*$, and charge transfer transitions occur in organic PI molecules [127]. In a short excited state, the photoinitiator (PI^*) tends to return to its original ground state by losing the energy, quenched by oxygen or monomer, or yielding to reactive species (free radicals or ions) [124]. The formation rate of PI^*s depends on the number of absorbed photons in unit time, on the fraction of PI^*, and on the fraction of PI. The number of absorbed photons is directly proportional to the light intensity. The photoinitiator absorbance is defined by Beer's law,

$$A = \varepsilon\, l\, [\mathrm{PI}] \qquad (1)$$

where ε is the photoinitiator molar absorptivity, l is the path length inside the PI system, and [PI] is the photoinitiator concentration. Nonetheless, the initiation rate is not proportional to the PI concentration. From equation (1), when [PI] increases, A increases proportionally. However, the amount of absorbed energy decreases exponentially along the path length, resulting in non-uniform polymerization. Hence, it is essential to find a balance between the initiation rate and the absorbance by adding the right concentration of PI, with defined molar absorptivity, to the system.

Also, the irradiation of the light source I_0 and the irradiation inside the PI system at path length l, I, can be related by Beer's equation:

$$A = \ln(I/I_0) \tag{2}$$

The combination of equations (1) and (2) gives:

$$l = -(1/\varepsilon[\mathrm{PI}])\ln(I/I_0) \tag{3}$$

Or,

$$I = I_0 \exp(-l\,\varepsilon\,[\mathrm{PI}]) \tag{4}$$

The corresponding dose of irradiation E (l, t) at time t is:

$$E = t\,I \exp(-l\,\varepsilon\,[\mathrm{PI}]) \tag{5}$$

The critical dose at which the polymer starts to polymerize is:

$$E_c = t_p\,I \exp(-l_p\varepsilon\,[\mathrm{PI}]) \tag{6}$$

Thus, corresponding to the critical time:

$$t_c = D_c/I_0 \tag{7}$$

Considering the critical radiation dose for polymerization, the thickness of the polymerized layer (l = D_c, cure depth) can be expressed as:

$$D_c = D_p \ln(t_p/t_c) \tag{8}$$

where the penetration depth D_p ($= 1/\varepsilon[\mathrm{PI}]$) and critical time t_c are entirely resin, i.e., material, parameters [176], depending on the photopolymer composition, and independent of the radiation source.

Another approach to reach equation (8) is through the reaction mechanism of free radical polymerization where the photopolymerization rate is related to the monomer concentration decrease, which is given by the sum of the initiation rate, R_i, and the propagation rate, R_p, with $R_p >> R_i$, thus,

$$Polymerization\ rate = \frac{-d[M]}{dt} = R_i + R_p \sim R_p \tag{9}$$

The polymerization rate (or propagation rate, R_p) can be expressed as the sum of all individual propagation rates, which are the same for all growing chains,

$$R_p = k_p[M][M'] \tag{10}$$

where k_p is the propagation rate constant, [M] and [M'] are the concentration of monomers and all growing chains, respectively [177]. The equation cannot

be used directly as the concentration of growing chains is difficult to measure. Therefore, a steady-state assumption is made, where the number of chains grows rapidly initially and reaches a steady state, and the rate of change quickly becomes zero. This implies that in steady state conditions, the initiation and termination rates are equal, i.e.

$$R_i = R_t = 2k_t[M']^2 \tag{11}$$

where k_t is the termination rate constant. Substituting the value of [M'] in eq. (10),

$$R_p = k_p[M]\left(\frac{R_i}{2k_t}\right)^{\frac{1}{2}} \tag{12}$$

For photoinitiated reactions, the initiation rate can be expressed as

$$R_i = 2\,\Phi\,I_V \tag{13}$$

where Φ is the quantum yield of the photoinitiator, I_V denotes the photons (in moles) absorbed per unit volume and time (Einstein or mol $cm^{-3}s^{-1}$), and the numeric factor 2 denotes the number of generated free radicals during photolysis. Substituting into equation (12),

$$R_p = k_p[M]\left(\frac{\Phi\,I_V}{k_t}\right)^{\frac{1}{2}} \tag{14}$$

Beer-Lambert's law can be used to determine the absorbed light as

$$I_S = I_0\left(1 - e^{-\alpha[PI]z}\right) \tag{15}$$

where I_S and I_0 (both are surface light intensity) are the absorbed light at distance z and on the surface, respectively. [PI] and α are the molar concentration and absorption coefficient of the photoinitiator.

To determine absorbed light intensity I_V at the distance z inside the vat, surface intensity I_S can be differentiated with respect to z,

$$I_V = \frac{dI_S}{dz} = \alpha[PI]\,I_0\,e^{-\alpha[PI]z} \tag{16}$$

Substituting I_V in equation (14),

$$R_p = k_p[M]\left(\frac{\Phi\ \alpha[PI]\ I_0\ e^{-\alpha[PI]z}}{k_t}\right)^{\frac{1}{2}} \quad (17)$$

The term represents polymerization rate at distance D_c. Further, from equation (9),

$$\frac{-d[M]}{dt} = R_p = k_p[M]\left(\frac{\Phi\ \alpha[PI]\ I_0\ e^{-\alpha[PI]z}}{k_t}\right)^{\frac{1}{2}} \quad (18)$$

Separating variables and integrating with the assumption of no time dependency in the bracketed term on the right-hand side, gives,

$$ln\frac{[M]_0}{[M]} = \left(\frac{{k_p}^2\Phi\ \alpha[PI]\ I_0\ e^{-\alpha[PI]z}}{k_t}\right)^{\frac{1}{2}}.t \quad (19)$$

The term on the left-hand side is simply the degree of polymerization with monomer conversion from $[M]_0$ to [M] after certain exposure ($t = t_p$),

$$Degree\ of\ polymerization\ (x) = \frac{[M]_0}{[M]} = \frac{1}{1-p} \quad (20)$$

where p is the extent of polymerization. At the gel point, $p = p_c$, the critical threshold for gelation. It, therefore, corresponds to the limit of the cure depth ($z = D_c$), in the photocuring process and is a characteristic of the photochemical system. From Equations (19) and (20),

$$\left[\frac{k_t}{{k_p}^2\Phi\alpha I_0}\right]\left[\frac{ln\ (1-p_c)}{t_p}\right]^2 = [PI]\ e^{-\alpha[PI]D_c} \quad (21)$$

Or,

$$\left[\frac{k_t\{ln\ (1-p_c)\}^2}{{k_p}^2\Phi\alpha}\right]\frac{1}{I_0 t_p^2} = [PI]\ e^{-\alpha[PI]D_c} \quad (22)$$

In DLP, the liquid photopolymer is polymerized by modulated light, which is reflected from DMD and focused on the vat base by an objective lens. Several models have been introduced to standardize the curing with pixel-based systems, assuming the reflected light from the single micromirror is incoherent but follows Gaussian distribution [178], as this is typical for lasers used in SLA. However, for our purpose, such an assumption is not necessary, and we

can simply consider an average irradiance within the illuminated pixel, I_{av} (W/cm^2), so that the energy per unit area at the vat base can be expressed as,

$$E_0 = I_{av}.t_p = \left(\frac{Nhc}{\lambda}\right) I_0.t_p \tag{23}$$

Rearranging and substituting values of I_0 and t_p in equation (22) gives

$$\left[\frac{k_t\{ln\,(1-p_c)\,\}^2}{{k_p}^2\Phi\alpha}\right]\frac{NhcI_{av}}{\lambda E_0^2} = \,[PI]\,e^{-\alpha[PI]D_c} \tag{24}$$

Substituting, $\left[\frac{k_t\{ln\,(1-p_c)\,\}^2}{{k_p}^2\Phi\alpha}\right] = A^2$, parameters based on the composition of the resin, $\frac{NhcI_{av}}{\lambda} = B^2$, light parameters, and solving equation (24),

$$D_c = \frac{2}{\alpha[PI]}\,ln\,\left[\frac{E_0[PI]^{\frac{1}{2}}}{AB}\right] \tag{25}$$

By comparing the above equation with Jacob's fundamental equation derived for stereolithography, one recognizes that the penetration depth, D_p, depends on the photoinitiator concentration, whereas critical energy is determined by both the photoinitiator concentration and the radiation source [179].

Furthermore, for constant radiation rate, the above equation can be rewritten as [117],

$$D_c = D_p \ln\left(\frac{t_p}{t_c}\right) \tag{26}$$

where t_c (= E_c / I_{av}) is the so-called critical time needed to start polymerization. Another representation of equation (26) is

$$D_c = D_p \ln\left(\frac{E_0}{E_c}\right) \tag{27}$$

where E_0 and E_c are corresponding energies for t_p and t_c, respectively.

3.4. Light interaction with suspensions

In pure photopolymers, polymerization depends on the factors defined in the previous section; however, in suspension (metal or ceramics) -based resins, the powder affects the resin interaction with the radiation. Specifically, the relevant parameters are the powder material, concentration, and size. For high-density final objects, it is necessary to have a better packing fraction, which is only possible with the high loading of small-size particles. However, the high-packing fraction reduces the radiation penetration inside the system, hindering polymerization. Polymerization thickness is calculated in suspension-based resins by modifying Beer's equation [180]:

$$D_c = \frac{2 < d >}{3Q} \frac{n_0^2}{\Delta n^2} \ln\left(\frac{E_0}{E_{crit}}\right) \tag{28}$$

where $<d>$ is the average particle size, Q is the scattering efficiency term, and Δn is the refractive index difference between the powder and the resin. To reduce scattering and lower the polymerization time, a decrease in the powder size and a close matching between the resin and powder refractive indexes are desirable.

4. Materials and Experimental Methods

4.1. Photopolymers

The research demonstrates the study on commercially available photopolymers for the vat polymerization process: Fun To Do (standard blend, Fun To Do, Netherlands), G-Strong (Sharebot S.r.l., Italy), Model Resin (HARZ Labs LLC., Russia), Dental Clear (HARZ Labs LLC., Russia), Porcelite (Tethon 3D, United States), and Ferrolite (Tethon 3D, United Stated) (Figure 4.1). Fun To Do, G-strong, Model Resin and Dental Clear are the mixtures of (meth-) acrylate-based monomers, oligomers and photoinitiator (undefined) with different color dyes: red, grey, black, and translucent, respectively. Porcelite and Ferrolite are alumina and iron-based suspensions, respectively, with similar composition as pure photopolymers. All materials were used as received. Ferrolite is further added with 1% of diphenyl (2,4,6-trimethylbenzoyl) phosphine oxide (TPO) (purity > 98.0%) (TCI Europe N.V., Netherlands) as a photoinitiator for extending its printability at a different wavelength. All the resins undergo chain polymerization through a free radical mechanism.

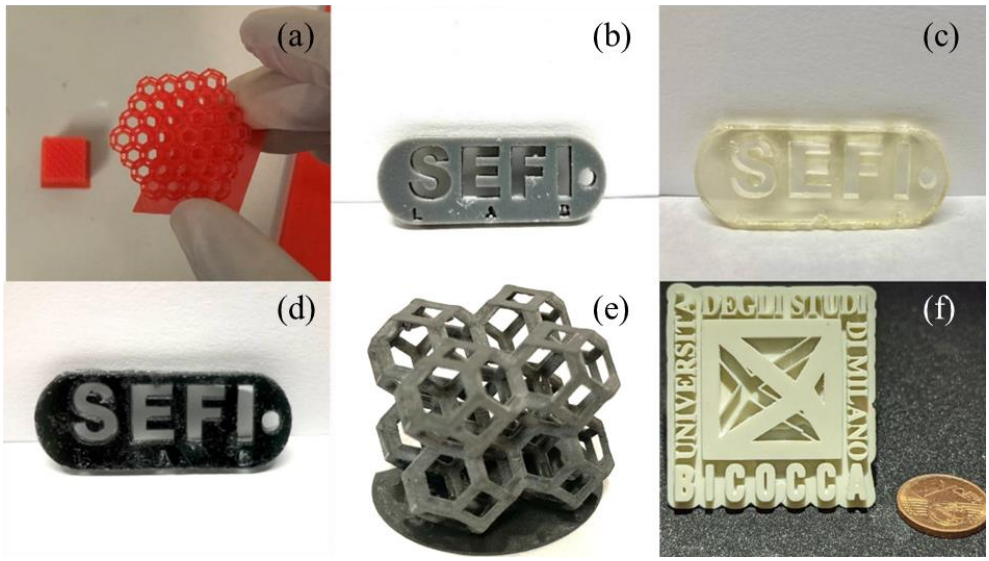

Figure 4.1 Printed objects using different photopolymers used in the study: (a) Fun To Do, (b) G-Strong, (c) Dental Clear, (d) Model Resin, (e) Ferrolite, and (f) Porcelite.

4.2. Printer and software

All the experiments were performed on two commercially available DLP printers with bottom-up configuration: 3DL Printer - HD 2.0+ (Robot Factory, Italy), available at the Laboratory of Material Technologies Faenza (ENEA-TEMAF), and Voyager Z-20 (Sharebot, Italy), available at the Department of Materials Science at UNIMIB (Figure 4.2).

4.2.1. Radiation Source

3DL Printer - HD 2.0+ is equipped with a high-resolution DLP source (365-405 nm) with printing resolution (i.e., pixel size) of ~50 μm in the XY-direction and from 30-100 μm in the Z-direction, along the layers. With the optimum build volume of 60 × 40 × 150 mm (Length, Width, Height), the

projection enables a layer-by-layer polymerization for the printing of three-dimensional objects.

Voyager Z-20 is powered with an LED-powered DLP source, with a printing resolution of ~50 μm (in XY-plane) and 5-200 μm (in Z-direction) with a build volume of 99.8×56.1×10 mm container area of ~140 × 120 mm^2. Radiation characteristics were further studied for material compatibility and printing optimization.

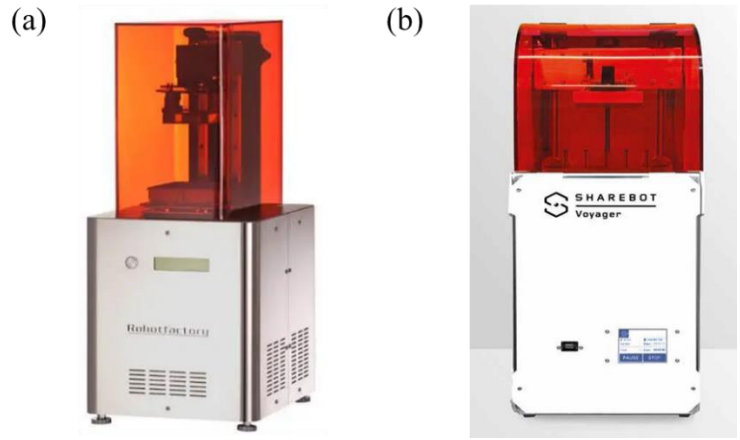

Figure 4.2 (a) 3DL Printer - HD 2.0+ and (b) Voyager Z-20 DLP printers. Both printers use a bottom-up configuration.

4.2.2. Vat (resin container)

In the 3DL Printer - HD 2.0+ printer, a cured dimethylpolysiloxane (PDMS) film, also referred to as siligel, over a glass plate worked as an interface. Whereas a fluorinated ethylene propylene (FEP) film over polymethyl methacrylate (PMMA) facilitated soft detachments in the Voyager Z-20 machine (Figure 4.3). These films facilitate soft detachments of each polymerized layer from the transparent vat base, due to the low adhesion to the polymerized layers.

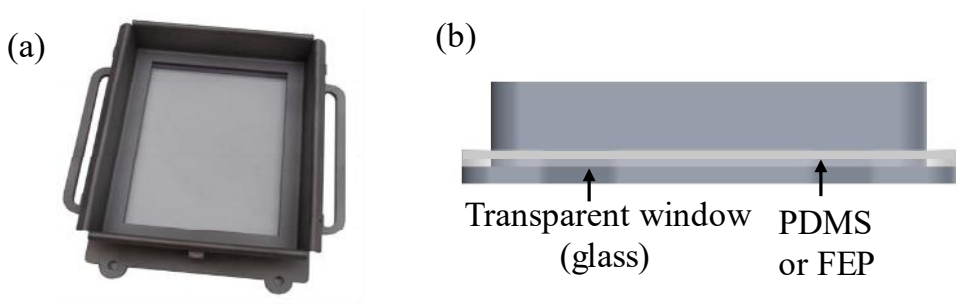

Figure 4.3 Top (a) and side view (b) of Vat and its component for the 3DL Printer - HD 2.0+ printer.

4.2.3. 3D design and Slicing

SOLIDWORKS and Fusion 360 were used for the generation of CAD files and exporting them into supported stl format. Printing parameters, including layer thickness, exposure time, radiation intensity, object orientation and printing placement (on the build head) were controlled by the printer slicing software. Additionally, layer-interface separation time was controlled only on the Pyramis slicing software specifically configured for the Voyager Z-20 printer.

Both the printers were used for object fabrication starting from either pure photopolymer or suspension, which could be eventually thermally treated during debinding and sintering.

4.2.4. Mask generation

Non-uniform radiation projected by the DLP source was compensated by imaging the light projection (Figure 4.4 a1, b1), only for 3DL Printer - HD 2.0+ printer. During the printing, the program analyzes the image of light projection, pixel by pixel, computes the negative (in the photographic sense),

and generates, with these values, the image (layer) to be projected (Figure 4.4 a2, b2). The effect of the mask was adjusted by varying the grayscale (0-255) of the image using printer software. The value represents the threshold of the conversion work in shades of gray, which can take values from 0 (Black) to 255 (White).

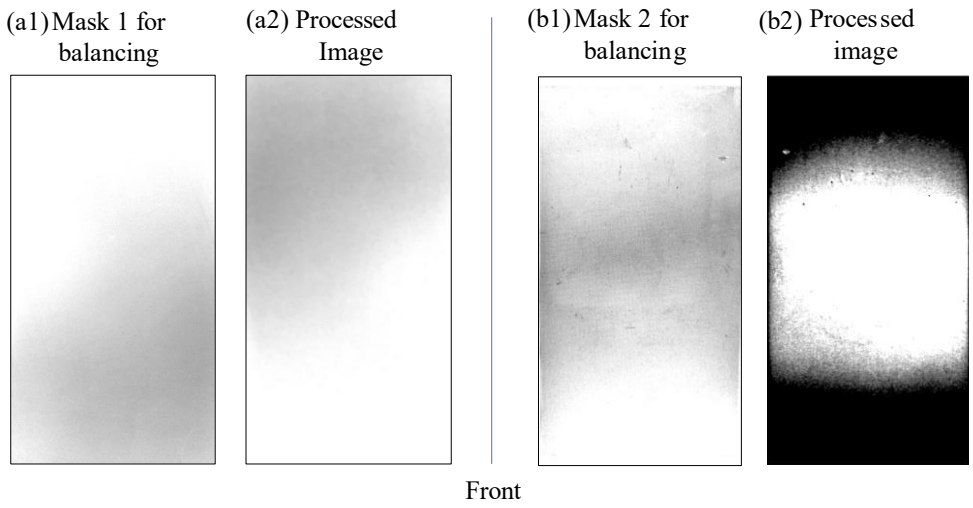

Figure 4.4 Captured images of the projection (a1) and (b1), and generated masks (a2) and (b2), respectively, for compensating the radiation.

4.3. Printability tests of photopolymer

Preliminary tests were performed to avoid printing failures and to find the optimum printing spot on the vat. Initially, surface defects in the Vat, formed during manufacturing and installing the PDMS film, were spotted. Later, the uniformity of projected radiation was improved by varying the grayscale of projection for digital masks. To test these flaws, a geometry covering the full projection of the light source, referred to as base (150 μm), with the dot patterns (350 μm) (Figure 4.5 a) printed with Fun To Do. The layer thickness was defined as 50 μm, which resulted in 3 layers for the base and 7 layers for the dots. The exposure time was varied in the experiment systematically to identify the correct printing conditions. After finding the optimum printing conditions, the correlation between exposure time and polymerized layer thickness was investigated for the photopolymer, Fun To Do, using a table structure (Figure 4.5 b). Printed objects were cleaned with solvents and further cured in a UV oven (Robot Factory, 36 W, 380-420 nm).

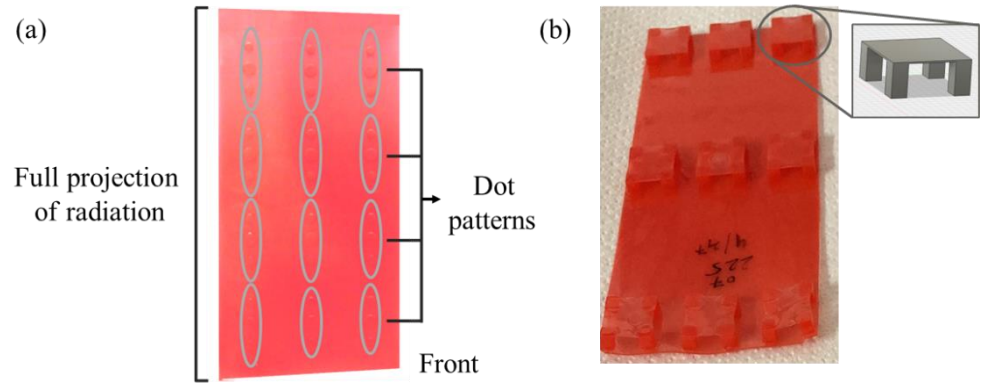

Figure 4.5 3D designs used for (a) analyzing printing defects, and (b) establishing a correlation between exposure time and polymerized layer thickness.

4.4. Sample preparation for photopolymer characterization

When the resin is exposed to radiation for a given polymerization time, t_p (corresponding to a given radiated energy, E_0), the resin polymerizes to form a film with a layer thickness, D_c. To study the correlation between D_c and t_p (or E_0), preliminary photopolymerization tests were conducted producing polymerized films in a free resin bath, in absence of the printing head (referred to as "no printing head" configuration). A single-layer CAD file to print a film with an area of 15 × 15 mm^2 (an arbitrary height of 50 μm was defined for the film thickness) was generated in Autodesk Fusion 360 and subsequently converted as STL as input for the Pyramis software. The vat container was filled with enough resin (typically up to 5 mm), ensuring that the resin at the bottom was not exposed to air, to avoid oxygen inhibition during polymerization. Fifteen monolayer films with different thicknesses using different irradiation times from 1 s to 8 s, in the step of 0.5 s, were prepared with each resin. Tests were then systematically repeated modulating the radiation power intensity at 100% (maximum), 80%, 60%, and 40% (see result section 5.2.1 between intensity and irradiance), to investigate the effect of radiation power on polymerization (corresponding to sample sets #1 to #4, respectively, see Table 4.1). These polymerized monolayer films were carefully detached from the vat to measure the thickness.

For FTIR analysis, monolayer films were prepared using the G-Strong resin, in no printing head configuration. The same CAD file and the procedure were followed as for previous sample sets, irradiating from 1 s to 8 s in the step of 1s, at 100% intensity (sample set #5, see Table 4.1). FTIR measurements were performed on the UV-exposed side of the monolayer films. Polymerized monolayer films were extracted from the vat after removing the liquid

photopolymer, to avoid contamination of the exposed side to the liquid photopolymer.

Table 4.1 Details of five sets of prepared samples (i.e., monolayer films, using the "no printing head" configuration, see text for details). In sets #1-#4, samples were produced for each resin modulating the radiation intensity; in set #5, G-Strong samples for G-Strong were prepared for FTIR analysis.

Set	Intensity (%)	UV Exposure time (s)	Time step (s)	No. of samples	Characterization	Note
#1	100	1-8	0.5	15	D_c vs t_p	No printing head; for each resin
#2	80	1-8	0.5	15	D_c vs t_p	No printing head; for each resin
#3	60	1-8	0.5	15	D_c vs t_p	No printing head; for each resin
#4	40	1-8	0.5	15	D_c vs t_p	No printing head; for each resin
#5	100	1-8	1	8	FTIR	No printing head; for G-Strong only

4.5. Characterization

4.5.1. Radiation Characterization of Voyager Z-20

The radiation spectrum of the DLP source was analyzed by a mini-spectrometer (C10083CA, Hamamatsu, Japan) with a spectral resolution (FWHM) of 5 nm. The radiation was collected using an optical fiber directed in the center of the projection area on the vat.

To investigate irradiance at different grayscale of projection, a power meter (PM200, Thorlabs, US) with Si photodiode power sensor (S120VC Thorlabs, US; aperture diameter 9.5 mm, measurement uncertainty ±5 %) was used. The measurements were taken while setting the attenuation 0 dB, wavelength 405 nm, bandwidth 10 kHz and range 18.0 mW in the power meter. The photodiode was placed at five different points on the vat, at the center of the projection area and at each of the four corners, to verify irradiance homogeneity in the plane of projection.

4.5.2. Material Characterization

The UV-Vis absorption of the photopolymers was collected using a UV-Vis spectrophotometer (Cary 60, Agilent, US). The scan was performed in the range of 200-800 nm, with a scan rate of 600 nm/min. The liquid photopolymer samples (thickness 0.12±.01 mm) were sandwiched between two microscopic glass slides (thickness 1 mm).

Surface thickness and dots of printed structure (Figure 4.5) were measured using a centesimal comparator (Borletti, Italy), with a resolution of 0.1 mm. Polymerized monolayer film thickness was measured using a digital caliper (2972, Kraftwerk, Switzerland) with a resolution of 0.01 mm (accuracy: ± 0.02 for size <100 mm), after gentle removal of excess liquid photopolymer with

tissue paper. The average and standard deviation were computed based on four measurements, taken on each side of the squared layer.

The IR absorption of polymerized monolayer films were recorded by FTIR spectrometer (JASCO 4100, US) using attenuated transmission reflectance (ATR) accessory equipped with ZnSe crystal. After careful extraction from the vat, the polymerized monolayer films were placed on the ATR crystal from UV-exposed sides and scanned at three different points. The transmittance was recorded in the range 550-4000 cm^{-1} using 4 cm^{-1} resolution after 64 scans.

Thermogravimetric analysis was done on Porcelite and Ferrolite to assess the powder concentration. The measurements were performed on a Thermogravimetric analyzer (Mettler Toledo, US) with a crucible volume of 100 µL in a 30-800 °C temperature range using a 10 °C/min ramp under 50 ml/min of nitrogen flow.

Particle size analysis for the ceramic and metallic powder in the resins Porcelite and Ferrolite was performed by an optical microscope (Leica Microsystems DM/LP, Germany) equipped with 5 lenses from 5x to 1000x.

Rheology measurements were performed with a rotational rheometer, MCR 92 (Anton Paar, Austria), using a 50 mm parallel plate setup. Rotational tests were carried out to determine the viscosities of all the photopolymers and suspensions using a plate gap of 0.25 mm and linear ramp shear rate 0-100 s^{-1} at 24 °C.

Scanning electron microscopy was performed with SEM-LEO 438 VP (Carl Zeiss AG, Germany) to assess the powder size distribution of the suspensions and surface analysis of thermally treated objects printed with Porcelite.

4.6. Post-printing and thermal treatment

4.6.1. Sample cleaning

The printed samples with Porcelite resin were removed and cleaned with IPA for the removal of excess liquid polymer. For complex geometries, an ultrasonic bath was used for the removal of excess polymer trapped in gaps and holes. Compressed air was used to dry the samples followed by the removal of supporting structures. Later, post-curing was performed in a UV oven for complete curing of the photopolymer.

4.6.2. Debinding and Sintering

Porcelite samples were debinded and sintered using MAB E-80 (Forni Mab, Italy) and Heraeus K1252 (Heraeus Holding GmbH, Germany) furnaces, respectively, in atmospheric conditions. Several samples (green parts) of different dimensions, in form of bars and parallelepiped, were prepared (Figure 4.6) and thermally treated using various heating cycles (see Table 4.2-Table 4.6). The objective was to maximize the final density of the solid object, which was the ratio between the final mass and volume of the sintered samples. The absolute density was, then, compared with the theoretical density of Porcelain (24 g/cm3) to determine the relative density.

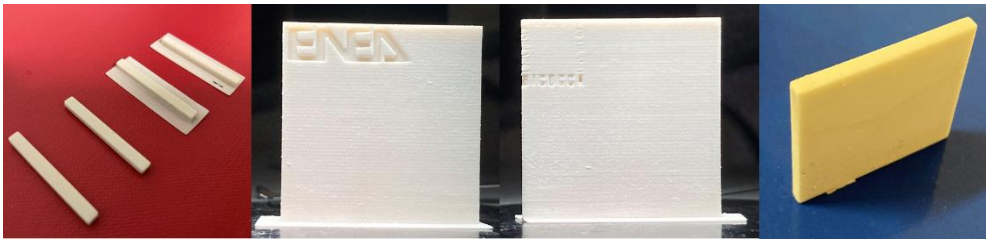

Figure 4.6 Samples (green) prepared for thermal treatment: debinding and sintering.

Table 4.2 Thermal cycle 1: Debinding and sintering performed in two different furnaces.

Step	Debinding		Sintering	
1	20°C-150°C	25°C/h	20°C-1100°C	112°C/h
2	150°C	1 h	1100°C	0 h
3	150°C-600°C	5°C/h	1100°C-1240°C	130°C/h
4	600°C	1 h	1240°C	0 h
5	600°C-20°C	250°C/h	1240°C-20°C	300°C/h
	Total time ~ 99.5 h		Total time ~15 h	

Table 4.3 Thermal cycle 2: Similar to thermal cycle 1, but with 1 h hold at temperature 1240°C during sintering.

Step	Debinding		Sintering	
1	20°C-150°C	25°C/h	20°C-1100°C	112°C/h
2	150°C	1 h	1100°C	0 h
3	150°C-600°C	5°C/h	1100°C-1240°C	130°C/h
4	600°C	1 h	1240°C	1 h
5	600°C-20°C	250°C/h	1240°C-20°C	300°C/h
	Total time ~ 99.5 h		Total time ~16 h	

Table 4.4 Thermal cycle 3: Similar to thermal cycle 2, but sintering is continued in the same furnace after debinding.

Step	Debinding + Sintering	
1	20°C-150°C	25°C/h
2	150°C	1 h
3	150°C-600°C	5°C/h
4	600°C	1 h
5	600°C-1100°C	112°C/h
6	1100°C	0 h
7	1100°C-1240°C	130°C/h
8	1240°C	1 h
9	1240°C-20°C	300°C/h
	Total time ~ 108 h	

Table 4.5 Thermal cycle 4: Similar parameters were used as thermal cycle 2, but the final temperature was increased by 40°C to improve the final density during sintering.

Step	Debinding		Sintering	
1	20°C-150°C	25°C/h	20°C-1100°C	112°C/h
2	150°C	1 h	1100°C	0 h
3	150°C-600°C	5°C/h	1100°C-1280°C	130°C/h
4	600°C	1 h	1280°C	1 h
5	600°C-20°C	250°C/h	1280°C-20°C	300°C/h
	Total time ~ 99.5 h		Total time ~16 h	

Table 4.6 Thermal cycle 5: Similar parameters were used as thermal cycle 2, but with an increase in the final temperature by 20°C during sintering.

Step	Debinding		Sintering	
1	20°C-150°C	25°C/h	20°C-1100°C	112°C/h
2	150°C	1 h	1100°C	0 h
3	150°C-600°C	5°C/h	1100°C-1300°C	130°C/h
4	600°C	1 h	1300°C	1 h
5	600°C-20°C	250°C/h	1300°C-20°C	300°C/h
	Total time ~ 99.5 h		Total time ~16 h	

5. Results

5.1. Experiments performed with 3DL Printer - HD 2.0+ printer

5.1.1. Surface homogeneity tests

To analyze the surface inhomogeneity of the vat, printing time was fixed as 6 s for the base and 2.7 s for the base of the object in Figure 4.5 a. However, only the base of the object (3 layers, 50 μm each) was considered for the measurements in this test. Three samples were printed while changing the relative position of the vat and build head: (a) Normal position, (b) inverting the position of the build head (front to back), and (c) Inverting the position of the build head and vat both, same as normal position (a) but inverted. The numbers in Figure 5.1a, b, and c represent the measurements (in μm) taken at the same point from the samples. The experimental values of thickness of each printed geometry showed huge variance from the theoretical value (150 μm).

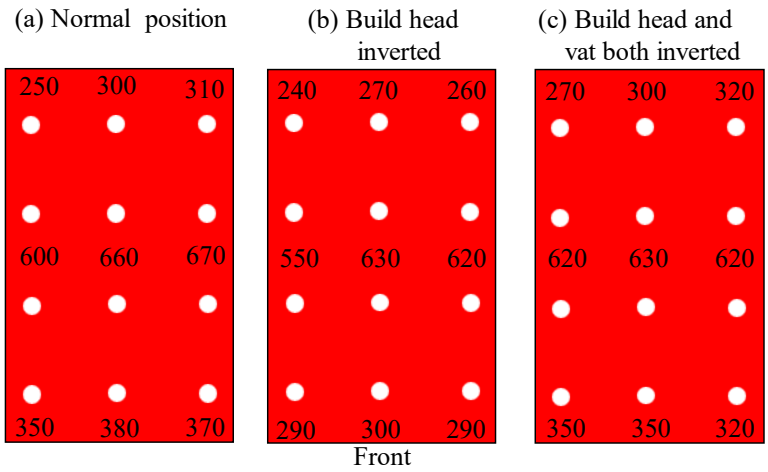

Figure 5.1 Thickness measurements (in μm) of the samples printed in: (a) Normal position, (b) inverted position of build head (front to back), and (c) inverted position of build head and vat both.

However, the measurements showed a trend while moving from the front and rear to the middle of the printed part, for all vat-build head positions.

Moreover, samples (a) and (c) showed similar variations, as they had an identical relative position of the vat and build head. For further validation, the tests were reproduced while applying the digital mask (referred to as mask 1 in Section 4.2.4).

Similar results were observed in the measurements (Figure 5.2), validating the surface defects in the vat. These defects seemed to affect the thickness of the first few layers of the base until the last polymerized layer takes the shape of the vat surface (Figure 5.3).

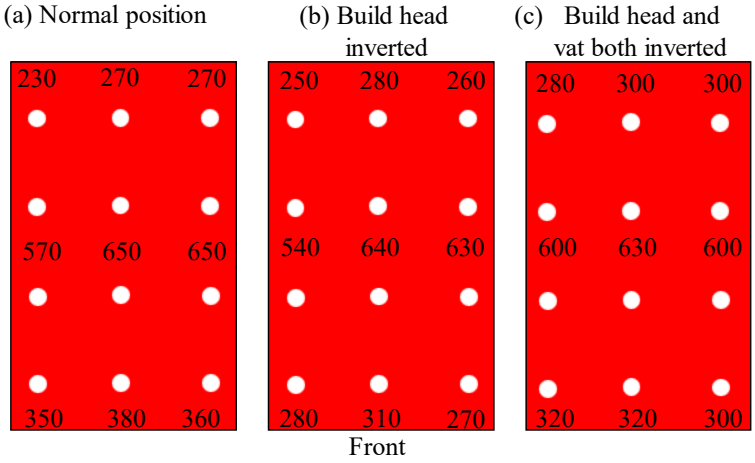

Figure 5.2 Thickness measurements (in μm) of the printed samples using mask 1.

These defects in the vat surface do not contribute much to the final geometry of the printed object. However, it creates an uneven gap between the build head and the vat base, resulting in nonuniform polymerization on the unexposed side of the first printed layer, which leads to the detachment of the printed object from the vat base. This situation is more likely for suspensions or low exposure times when irradiation is not enough to polymerize resin in big gaps (defects).

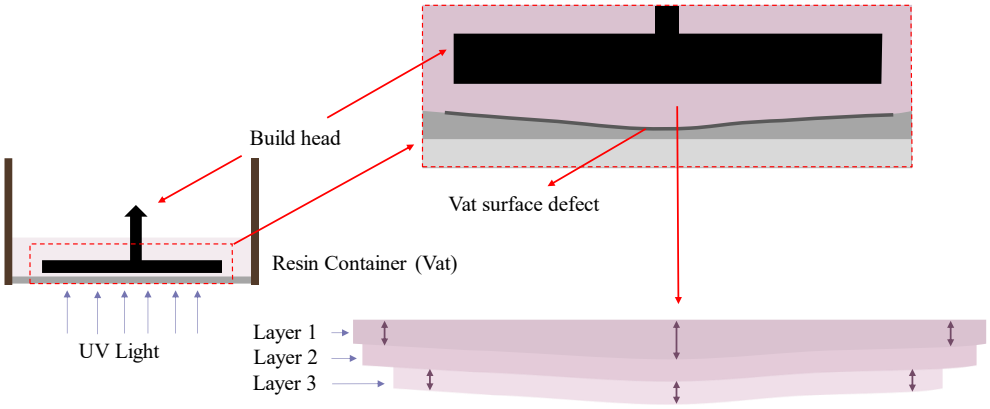

Figure 5.3 Thickness inhomogeneity generated in the first few printed layers due to vat surface defects.

5.1.2. Effect of masks

The effect of the applied mask was not visible in the previous test, due to enough curing of layers during the long (6 s) exposure time of the base. Therefore, dot patterns (7 layers, 50 μm each) were printed at a lower exposure time (2.7 s) to study the effect of masks in a further step (Figure 5.4). The thicknesses of the dots (in white) were calculated after subtracting the nearest measurement of the base (in black), from the total thickness (base and dot).

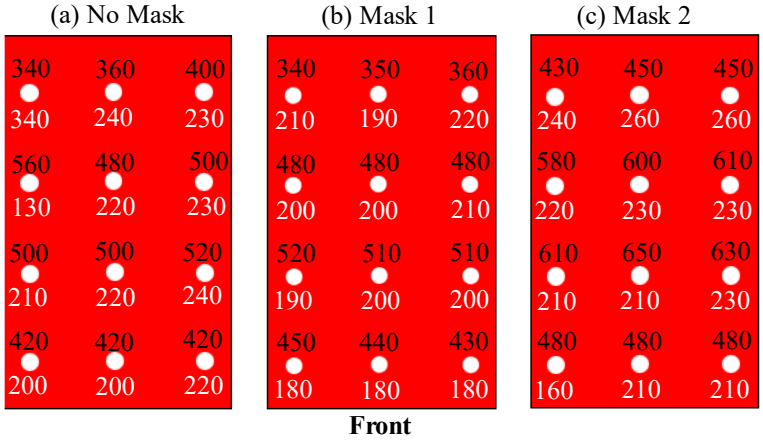

Figure 5.4 Thickness measurements (in μm) of the dot structures (in white) of the samples printed without applying mask (a), and after applying mask 1 (b) and mask 2 (c).

The measured thicknesses of the dots clearly showed the deviation from the theoretical value (350 μm). However, mask 1 showed the minimum deviation in the dots measurements while moving from rear to front. Therefore, the process was further optimized, while varying the grayscale for mask 1 and the corresponding exposure time.

5.1.3. Effective printing parameters

The methodology was again repeated in printing the same object for the determination of effective printing parameters, the threshold for mask 1, and the corresponding exposure time for the layers (Table 5.1).

Table 5.1 Samples prepared at different threshold values for mask 1 and corresponding exposure times for base and object (dot).

Sample	Threshold value	Base exp. time (s)	Object exp. time (s)
(a)	100	8	3.6
(b)	150	8	3.6
(c)	150	10	4.5
(d)	175	6	2.7
(e)	200	4	1.8
(f)	200	4	2.2
(g)	200	6	2.7
(h)	225	4	2.2

Printing of samples started with lower threshold values. For lower thresholds, the exposure times were increased in proportion with the times used for higher threshold values, to obtain similar results. However, variation in the measured thickness including printing failure of one dot was observed due to insufficient polymerization for threshold 100 (Figure 5.5 a, bottom left). As expected, the irradiation was not sufficient, and the mask was dominant at the threshold value. Therefore, a higher threshold (150) was applied for printing the sample using the same exposure times for the base and object.

No unprinted dot was observed with these parameters (Figure 5.5 b and c), however, the dots showed large deviations in the measurements, even at higher exposure times (10 s for base and 4.5 for dot), than the theoretical value.

The dots showed the least deviation in measurements along with the base thickness, printed with threshold 175 (Figure 5.5 d).

With threshold 200, three samples were printed (Figure 5.5 e, f, g) using different exposure times. With the decreased exposure times, for samples (e) and (f), the measurement showed a decrease in the front dots. However, at exposure time for sample (g), and for the sample prepared at threshold 225, the dots measurements showed more deviation than in sample (d).

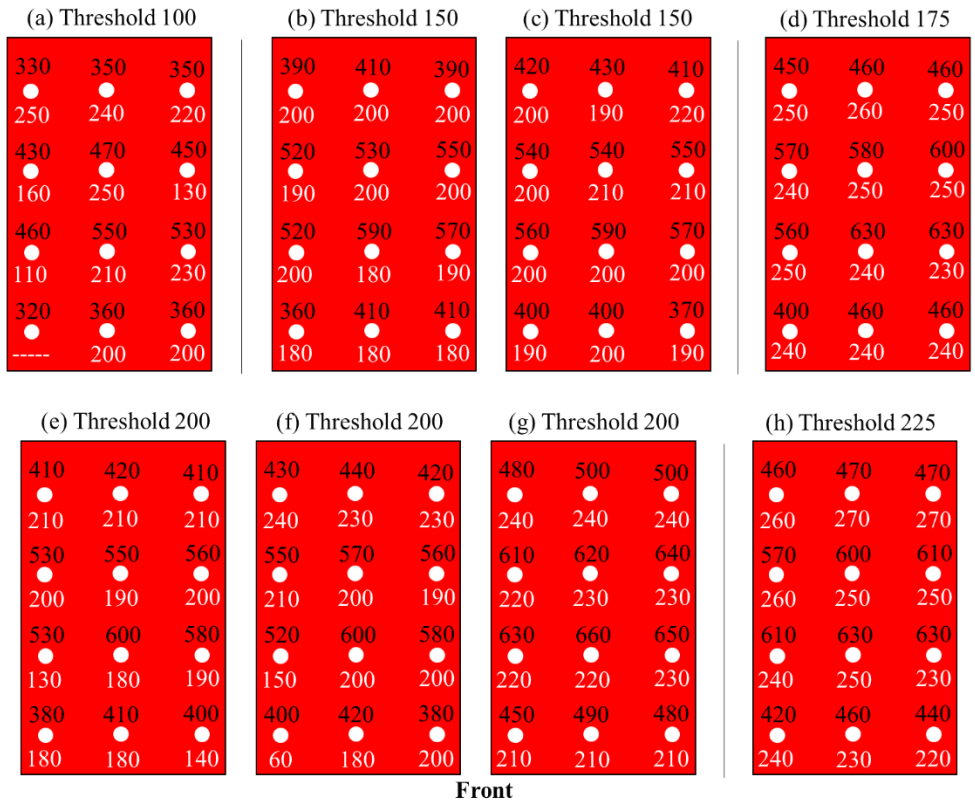

Figure 5.5 Thickness measurements (in μm) of the dot structures (in white) related to the surface thickness (in black), printed at different threshold values and exposure times.

Therefore, mask 1 (threshold 175) exposure time of 6 s (for base) and 2.7 s (for the object) was found most effective for printing in these tests.

5.1.4. Freeform layer thickness determination

Further experiments were performed to verify the previous results and understand the relationship between layer thickness and exposure time using Fun To Do resin. The table geometry used for the study (as shown in Figure 4.5 b) served the purpose of polymerization without the constraint of build head and relating the effect of exposure time on polymerization depth at three different positions 1, 2, and 3 (Figure 5.6 a). The data points presented in the graphs (Figure 5.6 b, c, d) denoted the layer thickness of the tabletop (layer) polymerized on the base, using different exposure times and threshold values for mask 1.

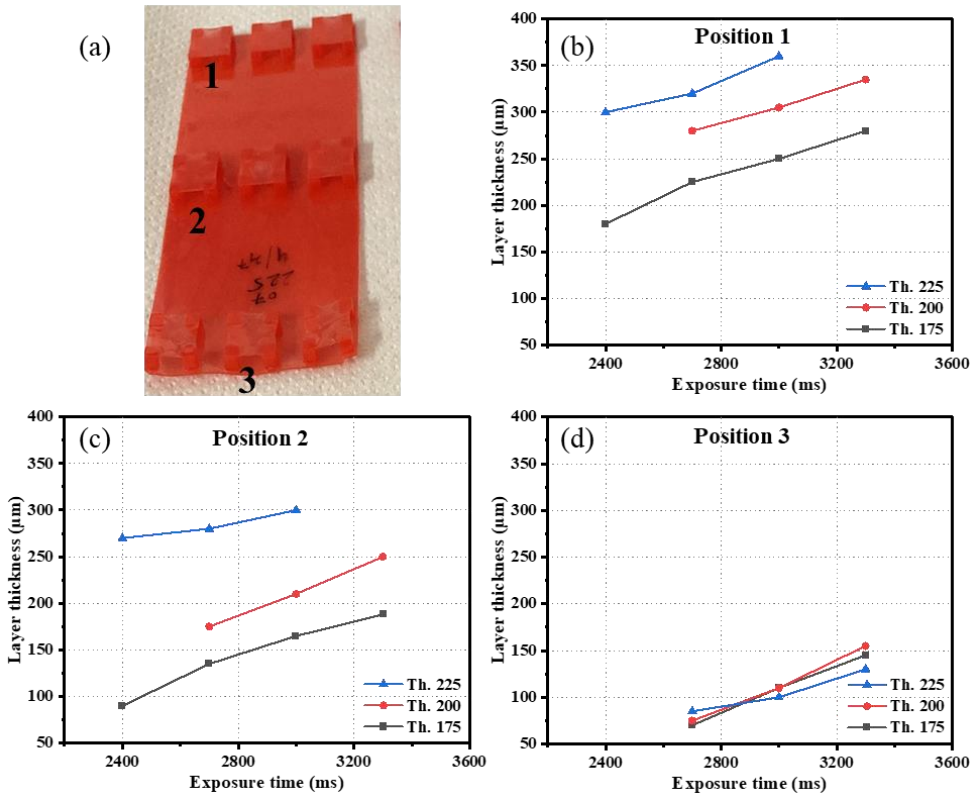

Figure 5.6 (a) Printed table-like structures on the base for determination of layer thickness as a function of exposure time and validation of effective printing parameters at different positions (b), (c), and (d).

These values of layer thickness with corresponding exposure time were fitted in equation (8) for the determination of the parameters: critical time, t_c, and penetration depth, D_p, for the constant radiation rate. The t_c and D_p were calculated as 307.3 µm and 1.3 s, respectively, for measurements at position 1, and 306.9 µm and 1.76 s, respectively, for position 2, at threshold 175. The parameters were not calculated for other thresholds as they showed high variance in layer thickness than threshold 175.

This study provided a detailed understanding of the optimization of the printing conditions: position, applied mask, threshold and corresponding exposure time for printing using DLP technology along with the starting point

to characterize the materials for DLP printing, which is discussed in further sections.

5.2. Rational design and characterization of materials with Voyager Z-20 printer

5.2.1. Radiation source characteristics

The radiation spectrum of the DLP source, illustrated in Figure 5.7 a, presents a peak at 405 nm, as expected by manufacturer information. As such, photopolymers need to absorb radiation around this wavelength to be photopolymerizable and printable. With respect to irradiance, preliminary tests confirmed a linear relationship between the projected light intensity (%) and irradiance, see Figure 5.7 b, as measured in five different points on the vat base.

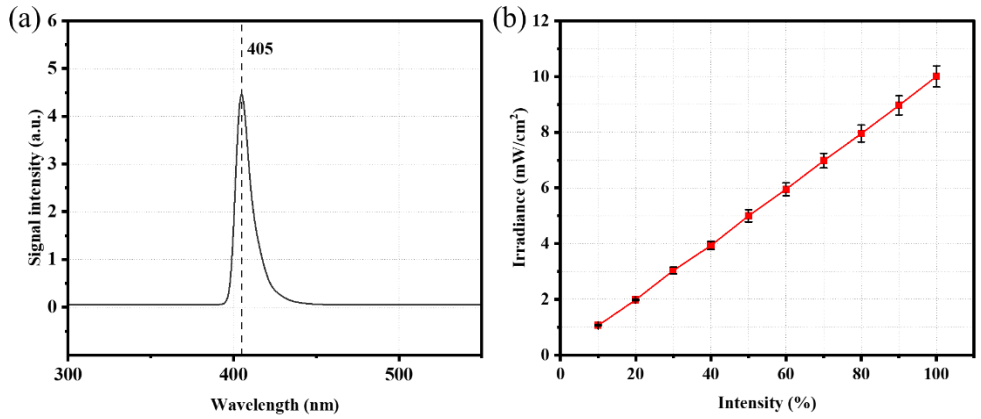

Figure 5.7 UV light characteristics of DLP printer: (a) radiation spectrum of the source, (b) irradiance at different light intensities (grayscale).

5.2.2. Preliminary characterization of resins

The compatibility of photopolymers with the DLP source was validated by preliminary UV-Visible spectroscopy analysis. All the pure resins, i.e., G-Strong, Dental Clear and Model Resin showed absorbance at 405 nm, corresponding to the peak wavelength of the DLP radiation (See Figure 5.8 a). For suspensions, the base resins of Porcelite and Ferrolite were tested after particle sedimentation. The base resin of Porcelite shows good absorption close to 405 nm, whereas Ferrolite base resin presents no significant peak. As such, 1 wt% of TPO, a photoinitiator, was added to Ferrolite, significantly increasing the absorption and thus photopolymerization (see Figure 5.8 a).

Rheology measurements confirm that all resins can be considered Newtonian fluids, as the viscosity is constant in the investigated shear rate range (see Figure 5.8 b). Viscosity is in the order of 10^2 mPa·s for pure resins and 10^3 mPa·s for suspensions. Nonetheless, all viscosities were found to be lower than the threshold of 3000 mPa·s: this value is considered in the literature as an upper limit for the liquid resin viscosity, to ensure full recoat of the vat base and thus good adhesion between two consecutive printing steps [84].

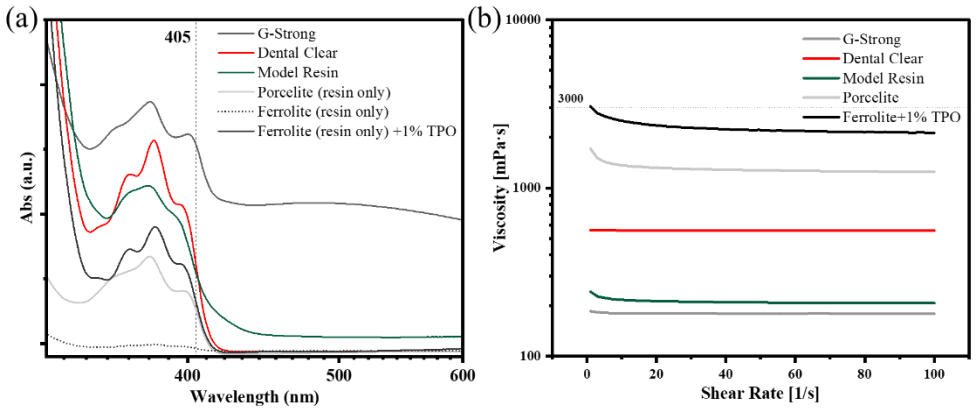

Figure 5.8 Characterization of photopolymers: (a) UV-Vis absorption and (b) rheology of the photopolymers and suspensions. Dashed lines in (a) and (b) correspond to the wavelength of the DLP source and reported limit of viscosity for self-recoating of liquid photopolymer, respectively.

The TGA degradation curves in Figure 5.9 indicated a weight loss, corresponding to the organic component in the suspension, equal to 48% and 43% for Porcelite and Ferrolite, respectively. As such, we can estimate the powder loading to be equal to 52% (Porcelite) and 57% (Ferrolite).

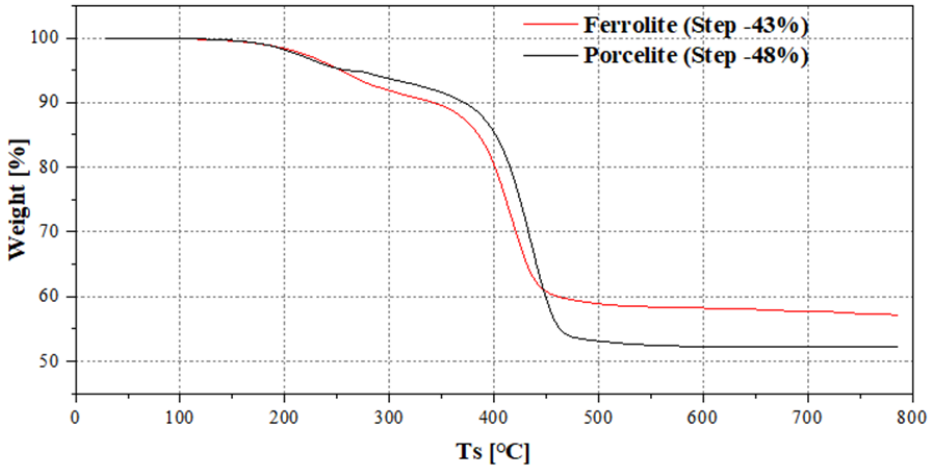

Figure 5.9 TGA curves for suspensions powder loading determination: Porcelite (black) and Ferrolite (red).

The optical images in Figure 5.10, showed that individual particles are in the range of 10-40 µm for both Ferrolite and Porcelite.

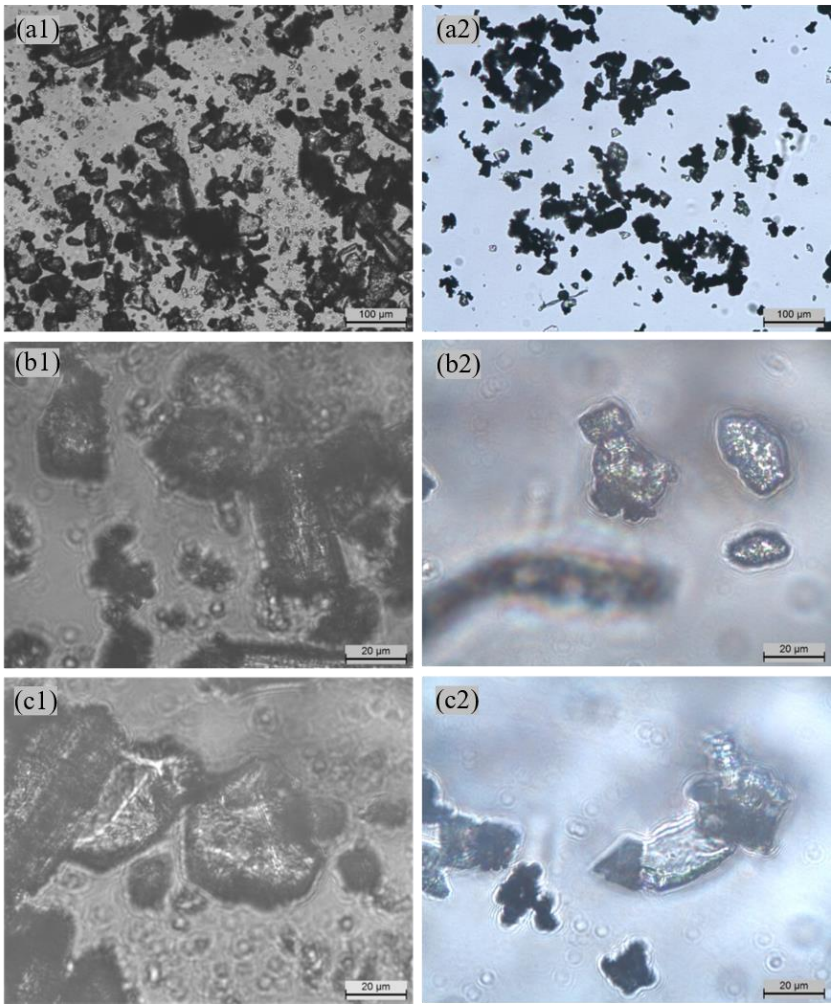

Figure 5.10 Microscopic images taken for particle size determination of Porcelite (a1), (b1) and (c1), and Ferrolite (a2), (b2) and (c2).

5.2.3. Polymerization of monolayer films

5.2.3.1. Pure photopolymers

The correlation between exposure time and the polymerized layer thickness is demonstrated by polymerizing monolayer films at different exposure times in no printing head configuration. The variation of polymerized layer thickness

with exposure time is shown in Figure 5.11 a1, b1 and c1 for pure photopolymers, G-Strong, Model Resin and Dental Clear, respectively. The different curves in each graph correspond to different radiation intensities, which were modulated from 40 to 100% (corresponding to irradiance values in the range of 4 to 10 mW/m^2, see Figure 5.8 b). As expected, the monolayer film thickness increases with both exposure time and irradiance. Also, a monolayer film forms after a certain critical time, which decreases with increasing irradiance. Since the product between the exposure time and irradiance is the energy flux, E_0, thickness values are also presented in Figure 5.11 a2, b2 and c2 as a function of the energy, using a semi-logarithmic plot. For each material, data clearly collapse on a single master curve, which can be fitted using Eq. 27 (Jacob's law), to identify experimentally two values: penetration depth and critical energy. For the fitting, only the experimental data below saturation (~ 50-60 mJ/cm^2) are selected. Insets in Figure 5.11 a2, b2 and c2 show D_p and E_c values as a function of light intensity (i.e. irradiance), with the red, dashed curve representing the value obtained by collective data average: for G-Strong, 173 μm and 6 mJ/cm^2, for Model Resin 246 μm and 4.4 mJ/cm^2, and for Dental Clear 317 μm and 3.6 mJ/cm^2, respectively.

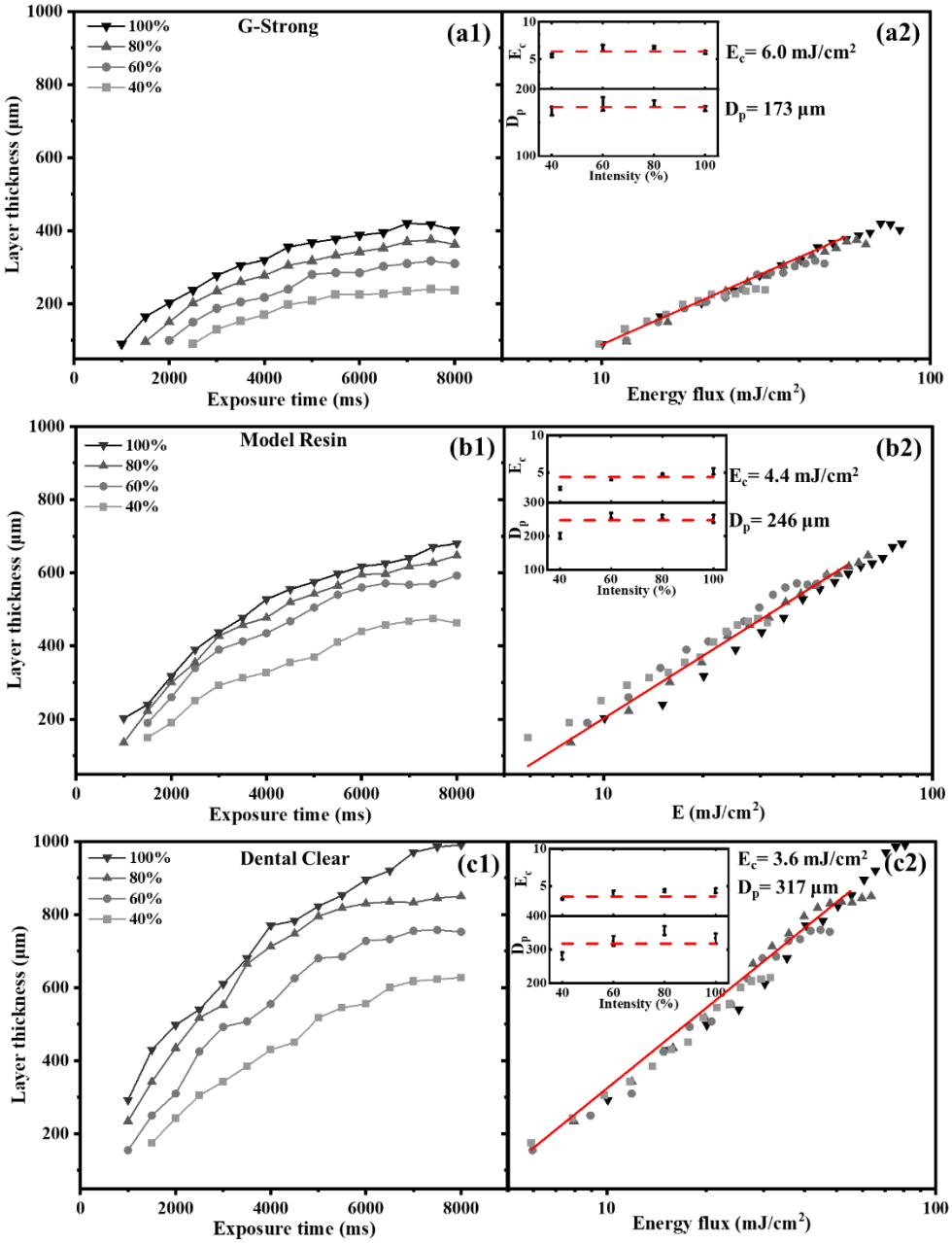

Figure 5.11 Monolayer film thickness as a function of exposure time at 100%, 80%, 60% and 40% light intensities (a1, b1, c1) and as a function of radiated energy flux (a2, b2, c2), for determination of critical energy (E_c) and penetration depth (D_p) of pure resins: G-Strong (a1) & (a2), Model Resin (b1) & (b2) and Dental Clear (c1) & (c2).

5.2.3.2. Suspensions

Similar work was also extended to two suspensions, Porcelite and Ferrolite, with results illustrated in Figure 5.12. Similar trends to pure photopolymers were observed, with monolayer film thickness increasing with both exposure time and irradiance, and the formation of a layer after a critical time. Even for each suspension, data collapse on a single master curve, to quantify penetration depth and critical energy. Experimental data below saturation are used for fitting using Jacob's equation, see Figure 5.12 a2 and b2, to find two characteristic parameters D_p and E_c: for Porcelite, 106 μm and 5.5 mJ/cm^2, and for Ferrolite, 43 μm and 2.3 mJ/cm^2, respectively. Clearly, highly concentrated suspensions have low irradiation penetration. Thus, critical energy is found to be lower than that of pure photopolymers as high powder concentration reduces the photopolymer volume for the same energy doses.

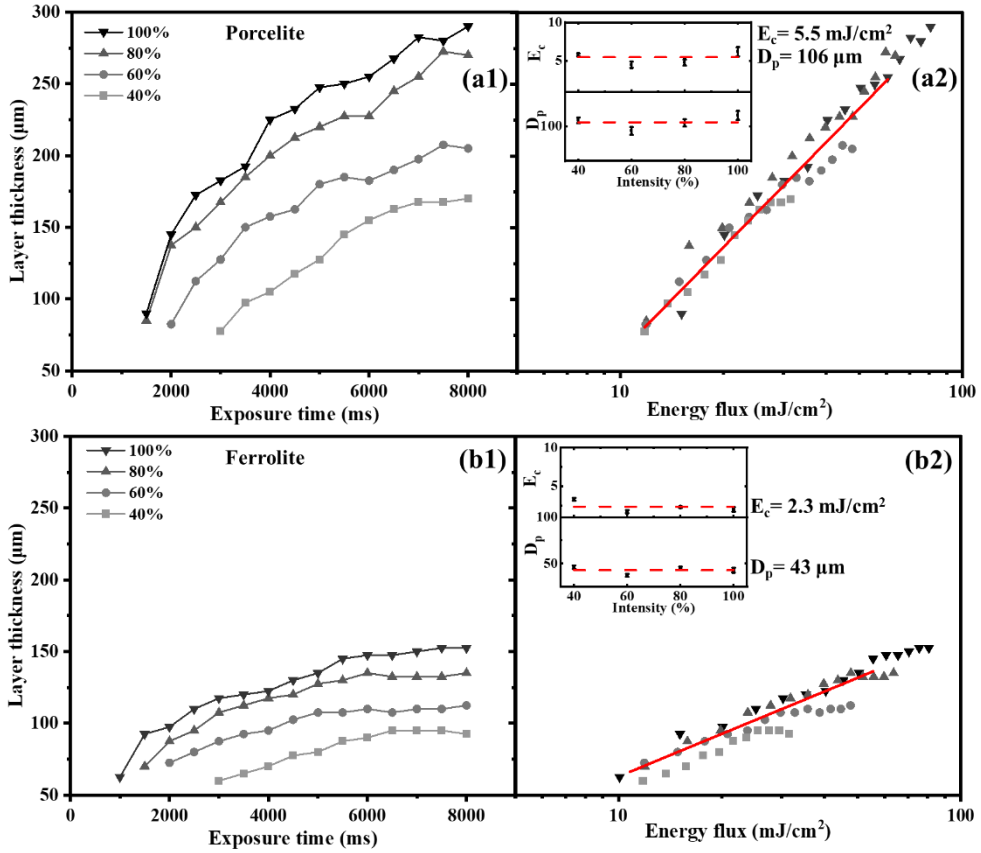

Figure 5.12 Monolayer film thickness as a function of exposure time at 100%, 80%, 60% and 40% light intensities (a1, b1) and as a function of radiated energy flux (a2, b2), for determination of critical energy (E_c) and penetration depth (D_p) of pure suspensions: Porcelite (a1) & (a2) and Ferrolite (+1% TPO) (b1) & (b2).

Evidently, DLP is a potential technology for high-resolution printing using pure photopolymer and suspensions, especially for metals after ceramics. Therefore, tuning the feedstock material for specific DLP printers and further thermal treatment of the printed objects with metal-based suspensions can be one of the prospectives for further studies.

5.2.4. FTIR-ATR analysis

FTIR-ATR spectroscopy was performed to understand the curing behavior of photopolymers with exposure times. Figure 5.13 a shows the absorption spectra of eight monolayer films prepared with G-Strong resin, each exposed to radiation from 1 to 8 s, with 1 s step increase (sample set #5), and the absorption spectrum of the original unexposed resin (0 s). Several vibrational peaks can be investigated to evaluate the conversion of acrylates such as $CH{=}CH_2$ twisting at 810 cm^{-1}, C-O stretching at 1192 cm^{-1}, CH_2 scissor deformation at 1405 cm^{-1}, and $CH{=}CH_2$ stretching at 1635 cm^{-1}, as shown in the literature [181]. The region between 900-1600 cm^{-1} (see Figure 5.13a) was the result of the overlap of several bands due to different bending modes. Both absorptions peaks at 1635 cm^{-1} and 810 cm^{-1} decrease with increasing exposure time, as a consequence of the decrease in the double bonds (C=C) of the acrylate group during polymerization. Among the two peaks, based on previous similar studies in the literature [182,183], we selected the absorption peak at 1635 cm^{-1} to quantify the degree of conversion during polymerization, as also for our measurement this peak shows a clear trend, compared to the peak at 810 cm^{-1}, which is more subject to noise [184]. The absorbance peak for aromatic at 1608 cm^{-1}, corresponding to C=C stretching, was chosen as the reference peak for normalization. Thus, the conversion was calculated as,

$$Degree\ of\ Conversion\ (DC)\ (\%) = \frac{\left(\frac{A_{1635}}{A_{1608}}\right)_0 - \left(\frac{A_{1635}}{A_{1608}}\right)_t}{\left(\frac{A_{1635}}{A_{1608}}\right)_0} \times 100 \qquad (28)$$

where the subscript 0 and t refer to time. The relative absorbance $(A_{1635}/A_{1608})_t$ decreases for increasing exposure time, see Figure 5.13 b, and correspondingly the degree of conversion increases to ~30% after 8 s of exposure. The increase at initial exposures shows the rapid growth in polymeric chains while consuming the reactive species and reaching a steady state.

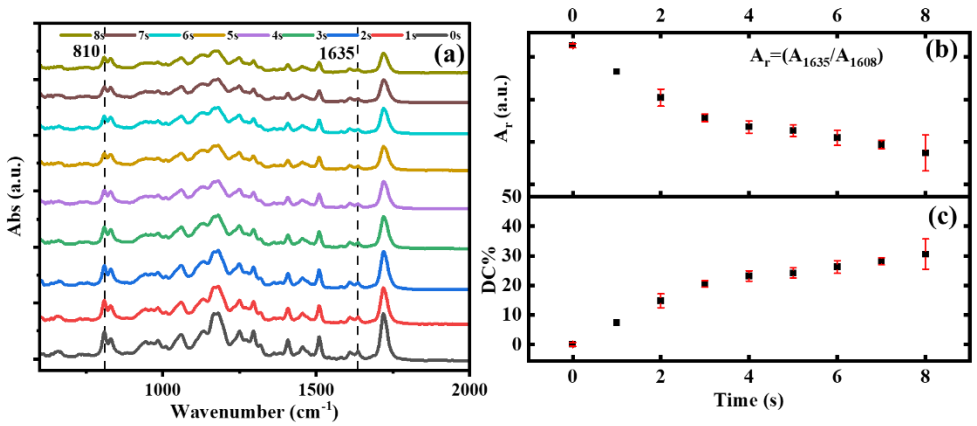

Figure 5.13 FTIR-ATR absorption spectra of freely polymerized layers (a), degree of double bond conversion (b), and relative absorbance (c) of monolayer films polymerized at exposure times without printing head configuration.

One should note that the polymerization is not homogenous within the bulk, as the radiation decays exponentially from the surface to the inner part of the material (see equation 15) [185]. Therefore, the degree of polymerization is not the same on the two sides of the polymerized layer, the bottom side (which is directly exposed to radiation) and the top side: the difference generally depends on the thickness. We have also performed additional tests to compare the difference in the degree of polymerization between the two sides, but they have not been reported due to lack of consistence: the main practical issue in such analysis is that the top layer remains wet by the unpolymerized resin. Both direct measurements of the top layer, without cleaning, and after cleaning with solvent, do not provide clear information on the surface composition during FTIR tests. Nonetheless, from an application point of view, sufficient polymerization should be ensured along the entire thickness, from the bottom to the top side, to facilitate good adhesion with the printing head and between consecutive layers. A decrease in the layer thickness at each step has to be defined, for minimizing the difference in the polymerization along the thickness. Thus, a compromise needs to be found between homogeneity, the required resolution and overall printing time.

5.2.5. Optimized 3D printing space

The trends observed for layer thickness increase as a function of the exposure time enable the definition of a 3D printing map (illustrated in Figure 5.14 a), where an optimal 3D printing space can be specified, based on simple preliminary experiments as those presented above.

Using the exposure time and the layer thickness as primary parameters and assuming given constant irradiation, I_{av}, the printing space is constrained on the left by the characteristic curve defined by Jacob's law expressed using the time (see Eq. 26), and on the right by a maximum time (t_{max}). This second limit is related to the polymerization of the bottom layer: since the adhesion between the vat base and the photopolymerized layer increase with the exposure time, when t_{max} is exceeded, the adhesion becomes too high, with a risk of damage for the layer or for the vat base when separating the two. At this point, the user can define the desired layer thickness, z_{print}: according to the printing space, the printing time must be chosen between t_{min} and t_{max}. The minimum time t_{min} is identified graphically as the intersection between the line corresponding to Eq. 26 and the set value z_{print} (see Figure 5.14a). Mathematically, this corresponds to:

$$t_{min} = t_c e^{\frac{z_{print}}{D_p}} = \frac{E_c}{I_{av}} e^{\frac{z_{print}}{D_p}} \tag{29}$$

where E_c and D_p are the critical energy and the penetration depth of the specific material that needs to be printed. Note that z_{print} results constrained between a minimum, z_{min}, and a maximum, z_{max}, value. The minimum, z_{min}, is set by the resolution of the machine (i.e. the precision of the step motor controlling the vertical motion of the printing head); also, in case of suspensions, z_{min} cannot be lower than the particle size. The maximum, z_{max}, is identified graphically

as the intersection between the line corresponding to Eq. 26 and the maximum time, t_{max} (see Figure 5.14 a). Indeed, layers thicker than z_{max} would require, according to Eq. 26, an exposure time, to ensure polymerization along the entire thickness, which is higher than t_{max}. As such, it would be impossible to satisfy both constraints ($t_{min} < t_p < t_{max}$) simultaneously.

Based on the above results, we demonstrate the potential of DLP to print complex objects using G-Strong (Figure 5.14 b1 & b2), Porcelite (Figure 5.14c) and Ferrolite (Figure 5.14 d). For G-Strong and Porcelite, the layer thickness z_{print} was set as 50 μm, which is well below the penetration depth (173 μm and 106 μm, respectively). For this thickness, the corresponding values for t_{min} and t_{max} for G-Strong are 0. 8 s and 3.6 s: as such, an exposure time of 1.9 s was selected for printing. For Porcelite, the corresponding t_{min} and t_{max} are 0.9 s and 5 s, respectively: as such, an exposure time of 3.6 s was selected for printing. For Ferrolite, the layer thickness was set as 40 μm, which is close to the penetration depth (43 μm). For this thickness, the corresponding t_{min} and t_{max} are 0.3 s and 6 s: as such an exposure time of 3.8 s was selected for printing.

The selected exposure time, t_p, was found adequate for polymerization and good adhesion of two consecutive printing layers. Note that, to ensure good adhesion to the printing head, only the first five layers, as base layers have been printed with an exposure time equal to t_{max}. As such, the 3D printing map, based on material characterization to define printing properties, proved to be a valuable tool for optimal printing using digital light processing.

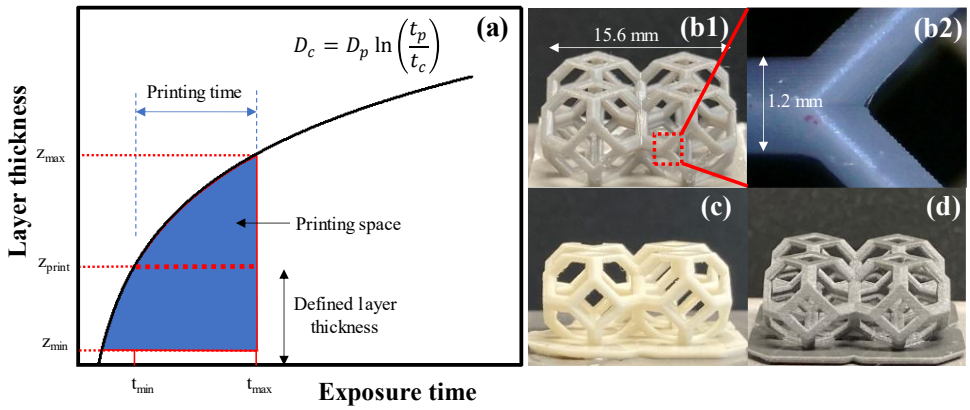

Figure 5.14 Schematic of DLP printing map defining optimized printing space (a). Objects printed with G-Strong (b) & (c), Porcelite (d) and Ferrolite (e) resin using the parameters from the map.

5.3. Preliminary thermal treatment

5.3.1. Debinding and sintering

After determining the printing conditions for Porcelite on the Robot Factory printer, samples were printed for preliminary thermal treatment to achieve a high relative density of the sintered samples (Figure 5.15 a and b).

As suggested in the literature, slow temperature ramps 25°C/h (from 20°C to 150°C) and 5°C/h (from 150°C to 600°C), and long temperature holds, 1h at 150°C and 600°C, were used. The two-step heating process should ensure the formation of interconnected pores for permeation of the gas during debinding, due to resin degradation, without crack formation (refer to Table 4.2-Table 4.6) [71].

Further, four heating cycles were used in the sintering step (thus more than a single step, suggested by Porcelite manufacturer), increasing and holding the maximum temperature. During these steps, the pores generated during the debinding should close, and densify the final object (see sintered samples after cycles 2, 3 and 4 in Figure 5.15 c, d and e, respectively). The results demonstrated (see Table 5.2) that a maximum relative density of 61% was reached, with linear shrinkage of ~16% in XY-direction and ~20 in the Z-direction (between the layers), which was found close to the reported values from the resin manufacturer [186]. The weight loss was measured to be ~53% due to the loss of the polymeric matrix.

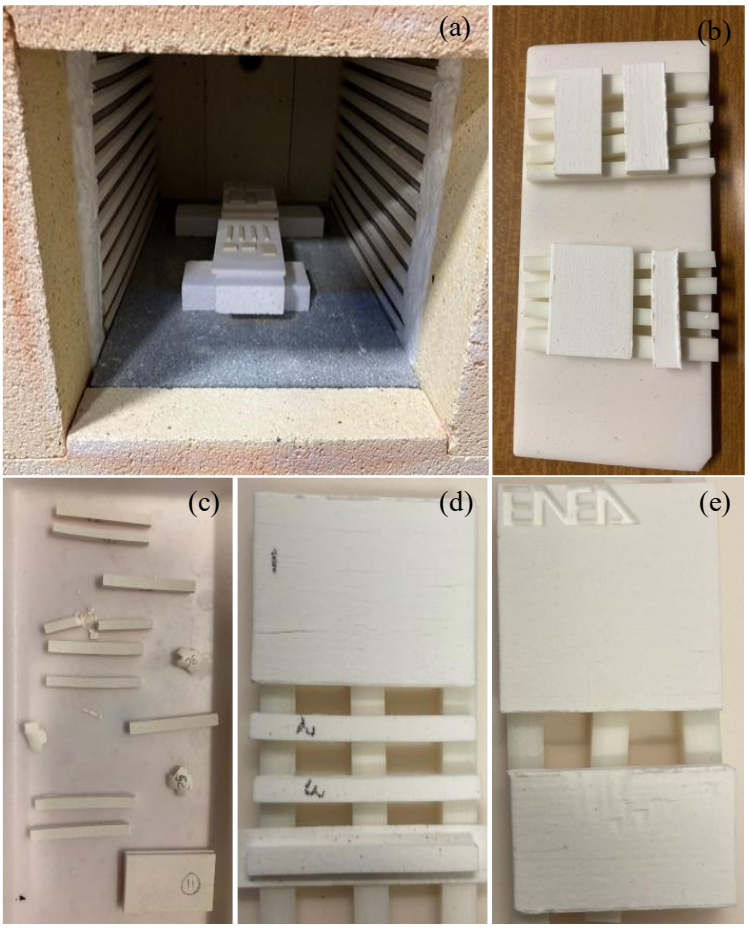

Figure 5.15 (a) Representation of the sample position inside the furnace. (b) Large samples were placed on a well-spaced grid of horizontal bars for good ventilation during debinding. (c)(d) and (e) represents the debinded and sintered samples in cycle 2, 3 and 4 respectively.

Table 5.2 Average shrinkage, density and weight loss of thermally treated samples produced in different heating cycles. Cycle 5 was performed using the same cycle as 5, however, all the printed samples were placed in the furnace as such the layer orientation would be horizontal.*

Cycle	Shrinkage		Density	Rel. Density (%)	Weight Loss
	Length (%)	Between Layers (%)	(gm/cm3)	(Sin. /Ref.) *100	(%)
1	15.1	19.4	1.4	57	53.3
2	14.0	18.6	1.4	58	51.9
3	14.3	18.9	1.4	58	51.5
4	14.9	18.8	1.4	57	52.0
5	15.1	18.8	1.4	59	52.0
5*	16.2	20.1	1.5	61	52.1

5.3.2. SEM analysis

SEM images of debinded and sintered samples from thermal cycles 1 (Figure 5.16 a and b) and 3 (Figure 5.16 c and d) confirmed the micro-cracks formed during the debinding, affecting the final density of the green samples. Literature suggests that these cracks could be formed due to excessive heating rate, low solid contents, or inappropriate temperature holding, resulting in

incomplete healing from the defects generated during debinding step, and may hinder reaching higher densities.

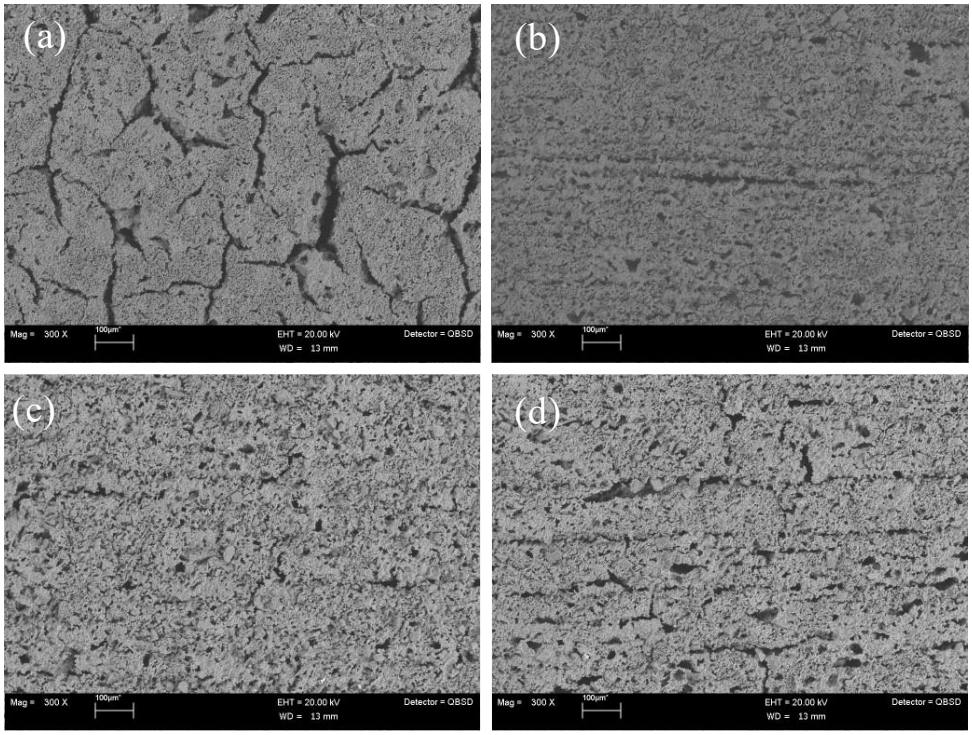

Figure 5.16 SEM images of the sintered samples in thermal cycles 1 (a) and (b), and cycle 3 (c) and (d).

6. Conclusions and perspectives

The thesis is focused on the characteristics and potential of DLP within the wide landscape of additive manufacturing technologies. DLP combines high manufacturing speed with precision, using a variety of materials, ranging from pure resins to ceramic- and metal-loaded suspensions. It begins with the detailed working principles of the DLP manufacturing process, describing the fundamentals of material interaction with the light source.

Specifically, the curing of pure photopolymers as well as ceramic and metal suspensions is investigated, characterizing the material properties relevant to the printing process, such as penetration depth and critical energy. We have presented the theoretical framework offered by the Beer-Lambert law, to understand the radiation absorption within the photopolymer and the associated photopolymerization dynamics. On this basis, along with the experimentally derived material properties, it is possible to define an optimal printing space. In practice, for any given material and printer combination, the methodology developed in this study allows defining a printing space, where the constraints are identified starting from the experimentally measured penetration depth and critical energy and simple design principles. Such a printing space can be used to rationally design new materials and optimize the printing process using DLP and can be also generalized for the optimization of other vat polymerization technologies.

Further, the potential of manufacturing complex functional and non-functional parts using polymers, suspensions, and functional materials attracted the interest of several industrial fields, including dentistry, tissue engineering, electronics, and microfluidics. Also, 4D printing, enabling the fabrication of new materials that change their properties under external stimuli, is a growing field that demonstrates a huge potential in the manufacturing of sensors and actuators, e.g. for robotics and smart wearables [187]. Optimized printing

systems, innovative methods, and newly engineered materials left behind major printing limitations, time, complexity, and materials.

Nonetheless, there are still some open challenges in adopting DLP, as well as other AM technologies, and substituting conventional technologies [188–190]. Among them, one of the questions is the scale of production, which is still limited: from a few microns to a few millimeters. Micro projection stereolithography seems promising in the fabrication of micro features [191] while optimizing printing quality: however, a trade-off exists between size and precision, due to the limited projected area of the DLP source. Another challenge for DLP is the time-consuming separation (and recoating for viscous suspensions) step of the cured layer. Few methods, such as CLIP [57], HARP [58], and tunable pre-curing DLP [192], have evolved to eliminate this time-consuming step but for highly concentrated suspensions (ceramics, metals, and composites) the problem still needs to be addressed. Multi-material printing is still a question for this technology along with other AM methods. To date, there is no commercial system available for multi-material printing with critical cleaning steps during material swapping to avoid cross-contamination. For suspension-based manufacturing of solid parts, the thermal treatment, debinding, and sintering, have still been a challenge in producing dense solid structures with this technology. The fact that very little research in metallic suspension-based manufacturing has been reported so far not only calls for more efforts in DLP-based metal printing but also opens other research opportunities for metallurgy. All these challenges need to be carefully addressed and will promote further research and development on DLP technology in the next coming years.

List of publications

1. R. Chaudhary, R. Akbari, C. Antonini, Rational Design and Characterization of Materials for Optimized Additive Manufacturing by Digital Light Processing, Polymers (Basel). 15 (2023) 287. https://doi.org/10.3390/polym15020287.
2. R. Chaudhary, P. Fabbri, E. Leoni, F. Mazzanti, R. Akbari, C. Antonini, Additive manufacturing by digital light processing: a review, Prog. Addit. Manuf. (2022). https://doi.org/10.1007/s40964-022-00336-0.

Conference presentation

1. R. Chaudhary, R. Akbari, C. Antonini, Characterization of Pure Photopolymers and Suspensions for Digital Light Processing (DLP), ASTM International Conference on Additive Manufacturing 2022, Orlando, FL, USA. (31.10.2022)

Invited talks

1. Additive Manufacturing of metals by Digital Light Processing (DLP) [Winter School of Metallurgy, Amirkabir University, Iran, 15/03/2022] (online)
2. Additive Manufacturing by Digital Light Processing (DLP) [University of Pavia, Italy, 17/01/2022]

7. Bibliography

[1] A. Gebhardt, J.-S. Hötter, Basics, Definitions, and Application Levels, in: Addit. Manuf., Carl Hanser Verlag GmbH & Co. KG, München, 2016: pp. 1–19. https://doi.org/10.3139/9781569905838.001.

[2] C.W. Hull, Arcadia, APPARATUS FOR PRODUCTION OF THREE-DIMENSONAL OBJECTS BY STEREOLITHOGRAPHY, 4,575,330, 1986. https://patentimages.storage.googleapis.com/5c/a0/27/e49642dab99cf6/US4575330.pdf (accessed May 19, 2022).

[3] U.M. Dilberoglu, B. Gharehpapagh, U. Yaman, M. Dolen, The Role of Additive Manufacturing in the Era of Industry 4.0, Procedia Manuf. 11 (2017) 545–554. https://doi.org/10.1016/j.promfg.2017.07.148.

[4] H. Lasi, P. Fettke, H.G. Kemper, T. Feld, M. Hoffmann, Industry 4.0, Bus. Inf. Syst. Eng. 6 (2014) 239–242. https://doi.org/10.1007/s12599-014-0334-4.

[5] T. Duda, L.V. Raghavan, 3D Metal Printing Technology, IFAC-PapersOnLine. 49 (2016) 103–110. https://doi.org/10.1016/j.ifacol.2016.11.111.

[6] S. Ford, M. Despeisse, Additive manufacturing and sustainability: an exploratory study of the advantages and challenges, J. Clean. Prod. 137 (2016). https://doi.org/10.1016/j.jclepro.2016.04.150.

[7] U. Chadha, A. Abrol, N.P. Vora, A. Tiwari, S.K. Shanker, S.K. Selvaraj, Performance evaluation of 3D printing technologies: a review, recent advances, current challenges, and future directions, Prog. Addit. Manuf. (2022) 1–34. https://doi.org/10.1007/s40964-021-00257-4.

[8] A. Bhargav, V. Sanjairaj, V. Rosa, L.W. Feng, J. Fuh YH, Applications of additive manufacturing in dentistry: A review, J. Biomed. Mater. Res. - Part B Appl. Biomater. 106 (2018) 2058–2064. https://doi.org/10.1002/jbm.b.33961.

[9] S. Singh, S. Ramakrishna, Biomedical applications of additive manufacturing: Present and future, Curr. Opin. Biomed. Eng. 2 (2017) 105–115. https://doi.org/10.1016/j.cobme.2017.05.006.

[10] L.R.R. da Silva, W.F. Sales, F. dos A.R. Campos, J.A.G. de Sousa, R. Davis, A. Singh, R.T. Coelho, B. Borgohain, A comprehensive review

on additive manufacturing of medical devices, Prog. Addit. Manuf. 6 (2021) 517–553. https://doi.org/10.1007/s40964-021-00188-0.

[11] M. Srivastava, S. Rathee, S. Maheshwari, T.K. Kundra, Additive Manufacturing Applications, in: Addit. Manuf., CRC Press, Florida, 2019: pp. 235–258. https://doi.org/10.1201/9781351049382-16.

[12] C. Carpenter, Additive Manufacturing for the Space Industry, in: Addit. Manuf., CRC Press, 2015: pp. 290–309. https://doi.org/10.1201/b18893-14.

[13] C. Buchanan, L. Gardner, Metal 3D printing in construction: A review of methods, research, applications, opportunities and challenges, Eng. Struct. 180 (2019) 332–348. https://doi.org/10.1016/j.engstruct.2018.11.045.

[14] D. Bourell, J.P. Kruth, M. Leu, G. Levy, D. Rosen, A.M. Beese, A. Clare, Materials for additive manufacturing, CIRP Ann. 66 (2017) 659–681. https://doi.org/10.1016/j.cirp.2017.05.009.

[15] E. Pei, G.H. Loh, D. Harrison, H. de A. Almeida, M.D. Monzón Verona, R. Paz, A study of 4D printing and functionally graded additive manufacturing, Assem. Autom. 37 (2017) 147–153. https://doi.org/10.1108/AA-01-2017-012.

[16] S. Rathee, M. Srivastava, S. Maheshwari, T.K. Kundra, A.N. Siddiquee, Friction Based Additive Manufacturing Technologies, CRC Press, Boca Raton, FL : CRC Press/Taylor & Francis Group, 2018., 2018. https://doi.org/10.1201/9781351190879.

[17] M. Srivastava, S. Rathee, S. Maheshwari, A. Noor Siddiquee, T.K. Kundra, A Review on Recent Progress in Solid State Friction Based Metal Additive Manufacturing: Friction Stir Additive Techniques, Crit. Rev. Solid State Mater. Sci. 44 (2019) 345–377. https://doi.org/10.1080/10408436.2018.1490250.

[18] S.C. Ligon, R. Liska, J. Stampfl, M. Gurr, R. Mülhaupt, Polymers for 3D Printing and Customized Additive Manufacturing, Chem. Rev. 117 (2017) 10212–10290. https://doi.org/10.1021/acs.chemrev.7b00074.

[19] B. Redwood, F. Schöffer, B. Garret, The 3D Printing Handbook: Technologies, design and applications, 3D Hubs, Amsterdam, 2017. https://lib.hpu.edu.vn/handle/123456789/31395.

[20] A. Gebhardt, J.-S. Hötter, Additive Manufacturing, in: Addit. Manuf., Carl Hanser Verlag GmbH & Co. KG, München, 2016: pp. I–XX.

https://doi.org/10.3139/9781569905838.fm.

[21] F. Calignano, D. Manfredi, E.P. Ambrosio, S. Biamino, M. Lombardi, E. Atzeni, A. Salmi, P. Minetola, L. Iuliano, P. Fino, Overview on additive manufacturing technologies, Proc. IEEE. 105 (2017) 593–612. https://doi.org/10.1109/JPROC.2016.2625098.

[22] K. V Wong, A. Hernandez, A Review of Additive Manufacturing, ISRN Mech. Eng. 2012 (2012) 1–10. https://doi.org/10.5402/2012/208760.

[23] J.-Y. Lee, J. An, C.K. Chua, Fundamentals and applications of 3D printing for novel materials, Appl. Mater. Today. 7 (2017) 120–133. https://doi.org/10.1016/j.apmt.2017.02.004.

[24] J.P. Kruth, X. Wang, T. Laoui, L. Froyen, Lasers and materials in selective laser sintering, Assem. Autom. 23 (2003) 357–371. https://doi.org/10.1108/01445150310698652.

[25] C.Y. Yap, C.K. Chua, Z.L. Dong, Z.H. Liu, D.Q. Zhang, L.E. Loh, S.L. Sing, Review of selective laser melting: Materials and applications, Appl. Phys. Rev. 2 (2015) 41101. https://doi.org/10.1063/1.4935926.

[26] H.K. Rafi, T.L. Starr, B.E. Stucker, A comparison of the tensile, fatigue, and fracture behavior of Ti–6Al–4V and 15-5 PH stainless steel parts made by selective laser melting, Int. J. Adv. Manuf. Technol. 69 (2013) 1299–1309. https://doi.org/10.1007/s00170-013-5106-7.

[27] S.L. Sing, W.Y. Yeong, F.E. Wiria, B.Y. Tay, Z. Zhao, L. Zhao, Z. Tian, S. Yang, Direct selective laser sintering and melting of ceramics: a review, Rapid Prototyp. J. 23 (2017) 611–623. https://doi.org/10.1108/RPJ-11-2015-0178.

[28] C. Körner, Additive manufacturing of metallic components by selective electron beam melting - A review, Int. Mater. Rev. 61 (2016) 361–377. https://doi.org/10.1080/09506608.2016.1176289.

[29] L.E. Murr, S.M. Gaytan, D.A. Ramirez, E. Martinez, J. Hernandez, K.N. Amato, P.W. Shindo, F.R. Medina, R.B. Wicker, Metal Fabrication by Additive Manufacturing Using Laser and Electron Beam Melting Technologies, J. Mater. Sci. Technol. 28 (2012) 1–14. https://doi.org/10.1016/S1005-0302(12)60016-4.

[30] M. Izadi, A. Farzaneh, M. Mohammed, I. Gibson, B. Rolfe, A review of laser engineered net shaping (LENS) build and process parameters of metallic parts, Rapid Prototyp. J. 26 (2020) 1059–1078.

https://doi.org/10.1108/RPJ-04-2018-0088/FULL/PDF.

[31] Y. Li, Y. Hu, W. Cong, L. Zhi, Z. Guo, Additive manufacturing of alumina using laser engineered net shaping: Effects of deposition variables, Ceram. Int. 43 (2017) 7768–7775. https://doi.org/10.1016/J.CERAMINT.2017.03.085.

[32] I. Gibson, D. Rosen, B. Stucker, M. Khorasani, Additive Manufacturing Technologies, Springer International Publishing, Cham, 2021. https://doi.org/10.1007/978-3-030-56127-7.

[33] M. Ziaee, N.B. Crane, Binder jetting: A review of process, materials, and methods, Addit. Manuf. 28 (2019) 781–801. https://doi.org/10.1016/j.addma.2019.05.031.

[34] X. Lv, F. Ye, L. Cheng, S. Fan, Y. Liu, Binder jetting of ceramics: Powders, binders, printing parameters, equipment, and post-treatment, Ceram. Int. 45 (2019) 12609–12624. https://doi.org/10.1016/j.ceramint.2019.04.012.

[35] D. Ahn, J.H. Kweon, J. Choi, S. Lee, Quantification of surface roughness of parts processed by laminated object manufacturing, J. Mater. Process. Technol. 212 (2012) 339–346. https://doi.org/10.1016/J.JMATPROTEC.2011.08.013.

[36] B. Dermeik, N. Travitzky, Laminated Object Manufacturing of Ceramic-Based Materials, Adv. Eng. Mater. 22 (2020) 2000256. https://doi.org/10.1002/adem.202000256.

[37] O.A. Mohamed, S.H. Masood, J.L. Bhowmik, Optimization of fused deposition modeling process parameters: a review of current research and future prospects, Adv. Manuf. 3 (2015) 42–53. https://doi.org/10.1007/s40436-014-0097-7.

[38] S.C. Daminabo, S. Goel, S.A. Grammatikos, H.Y. Nezhad, V.K. Thakur, Fused deposition modeling-based additive manufacturing (3D printing): techniques for polymer material systems, Mater. Today Chem. 16 (2020) 100248. https://doi.org/10.1016/j.mtchem.2020.100248.

[39] A.D. Castiaux, C.W. Pinger, E.A. Hayter, M.E. Bunn, R.S. Martin, D.M. Spence, PolyJet 3D-Printed Enclosed Microfluidic Channels without Photocurable Supports, Anal. Chem. 91 (2019) 6910–6917. https://doi.org/10.1021/ACS.ANALCHEM.9B01302/SUPPL_FILE/AC9B01302_SI_002.ZIP.

[40] A. Cazón, P. Morer, L. Matey, PolyJet technology for product prototyping: Tensile strength and surface roughness properties, Proc. Inst. Mech. Eng. Part B J. Eng. Manuf. 228 (2014) 1664–1675. https://doi.org/10.1177/0954405413518515.

[41] P.J. Bártolo, Stereolithographic Processes, in: Stereolithography, Springer US, Boston, MA, 2011: pp. 1–36. https://doi.org/10.1007/978-0-387-92904-0_1.

[42] M. Pagac, J. Hajnys, Q.-P. Ma, L. Jancar, J. Jansa, P. Stefek, J. Mesicek, A Review of Vat Photopolymerization Technology: Materials, Applications, Challenges, and Future Trends of 3D Printing, Polymers (Basel). 13 (2021) 598. https://doi.org/10.3390/polym13040598.

[43] Q. Mu, L. Wang, C.K. Dunn, X. Kuang, F. Duan, Z. Zhang, H.J. Qi, T. Wang, Digital light processing 3D printing of conductive complex structures, Addit. Manuf. 18 (2017) 74–83. https://doi.org/10.1016/j.addma.2017.08.011.

[44] X. Kuang, J. Wu, K. Chen, Z. Zhao, Z. Ding, F. Hu, D. Fang, H.J. Qi, Grayscale digital light processing 3D printing for highly functionally graded materials, Sci. Adv. 5 (2019). https://doi.org/10.1126/sciadv.aav5790.

[45] L.J. Hornbeck, Digital Light Processing update: status and future applications, in: M.H. Wu (Ed.), Proj. Displays V, 1999: pp. 158–170. https://doi.org/10.1117/12.349351.

[46] D.W. Monk, R.O. Gale, The digital micromirror device for projection display, Microelectron. Eng. 27 (1995) 489–493. https://doi.org/10.1016/0167-9317(94)00151-J.

[47] O. Santoliquido, P. Colombo, A. Ortona, Additive Manufacturing of ceramic components by Digital Light Processing: A comparison between the “bottom-up” and the “top-down” approaches, J. Eur. Ceram. Soc. 39 (2019) 2140–2148. https://doi.org/10.1016/j.jeurceramsoc.2019.01.044.

[48] X. Wu, C. Xu, Z. Zhang, Flexible film separation analysis of LCD based mask stereolithography, J. Mater. Process. Technol. 288 (2021) 116916. https://doi.org/10.1016/j.jmatprotec.2020.116916.

[49] L. Wu, Z. Dong, H. Du, C. Li, N.X. Fang, Y. Song, Bioinspired Ultra-Low Adhesive Energy Interface for Continuous 3D Printing: Reducing Curing Induced Adhesion, Research. 2018 (2018) 1–10. https://doi.org/10.1155/2018/4795604.

[50] D.A. Walker, J.L. Hedrick, C.A. Mirkin, Rapid, large-volume, thermally controlled 3D printing using a mobile liquid interface., Science. 366 (2019) 360–364. https://doi.org/10.1126/science.aax1562.

[51] Y. Xu, Y. Zhu, Y. Sun, J. Jin, Y. Chen, A Vibration-Assisted Separation Method for Constrained-Surface-Based Stereolithography, J. Manuf. Sci. Eng. 143 (2021). https://doi.org/10.1115/1.4048445.

[52] X. Wu, Q. Lian, D. Li, Z. Jin, Tilting separation analysis of bottom-up mask projection stereolithography based on cohesive zone model, J. Mater. Process. Technol. 243 (2017) 184–196. https://doi.org/10.1016/J.JMATPROTEC.2016.12.016.

[53] R.B. Wicker, E.W. MacDonald, Multi-material, multi-technology stereolithography, Virtual Phys. Prototyp. 7 (2012) 181–194. https://doi.org/10.1080/17452759.2012.721119.

[54] Q. Ge, A.H. Sakhaei, H. Lee, C.K. Dunn, N.X. Fang, M.L. Dunn, Multimaterial 4D Printing with Tailorable Shape Memory Polymers., Sci. Rep. 6 (2016) 31110. https://doi.org/10.1038/srep31110.

[55] X. Peng, X. Kuang, D.J. Roach, Y. Wang, C.M. Hamel, C. Lu, H.J. Qi, Integrating digital light processing with direct ink writing for hybrid 3D printing of functional structures and devices, Addit. Manuf. 40 (2021) 101911. https://doi.org/10.1016/j.addma.2021.101911.

[56] H.X. Nguyen, H. Suen, B. Poudel, P. Kwon, H. Chung, Development of an innovative, high speed, large-scaled, and affordable metal additive manufacturing process, CIRP Ann. 69 (2020) 177–180. https://doi.org/10.1016/j.cirp.2020.04.069.

[57] R. Janusziewicz, J.R. Tumbleston, A.L. Quintanilla, S.J. Mecham, J.M. DeSimone, Layerless fabrication with continuous liquid interface production., Proc. Natl. Acad. Sci. U. S. A. 113 (2016) 11703–11708. https://doi.org/10.1073/pnas.1605271113.

[58] D.A. Walker, J.L. Hedrick, C.A. Mirkin, Rapid, large-volume, thermally controlled 3D printing using a mobile liquid interface, Science (80-.). 366 (2019) 360–364. https://doi.org/10.1126/science.aax1562.

[59] B.E. Kelly, I. Bhattacharya, H. Heidari, M. Shusteff, C.M. Spadaccini, H.K. Taylor, Volumetric additive manufacturing via tomographic reconstruction., Science. 363 (2019) 1075–1079. https://doi.org/10.1126/science.aau7114.

[60] M.T. Raimondi, S.M. Eaton, M.M. Nava, M. Laganà, G. Cerullo, R. Osellame, Two-photon laser polymerization: from fundamentals to biomedical application in tissue engineering and regenerative medicine., J. Appl. Biomater. Funct. Mater. 10 (2012) 55–65. https://doi.org/10.5301/JABFM.2012.9278.

[61] A.-I. Bunea, N. del Castillo Iniesta, A. Droumpali, A.E. Wetzel, E. Engay, R. Taboryski, Micro 3D Printing by Two-Photon Polymerization: Configurations and Parameters for the Nanoscribe System, Micro. 1 (2021) 164–180. https://doi.org/10.3390/micro1020013.

[62] J.W. Choi, H.C. Kim, R. Wicker, Multi-material stereolithography, J. Mater. Process. Technol. 211 (2011) 318–328. https://doi.org/10.1016/J.JMATPROTEC.2010.10.003.

[63] J.D. Spencer, R.C. Cobb, P.M. Dickens, Vibratory Finishing of Stereolithography Parts, Int. Solid Free. Fabr. Symp. (1993). https://doi.org/10.15781/T2DJ5906T.

[64] N.N. Kumbhar, A. V. Mulay, Post Processing Methods used to Improve Surface Finish of Products which are Manufactured by Additive Manufacturing Technologies: A Review, J. Inst. Eng. Ser. C. 99 (2018) 481–487. https://doi.org/10.1007/s40032-016-0340-z.

[65] D. Mostafavi, M.M. Methani, W. Piedra-Cascón, A. Zandinejad, M. Revilla-León, Influence of the Rinsing Postprocessing Procedures on the Manufacturing Accuracy of Vat-Polymerized Dental Model Material, J. Prosthodont. 30 (2021) 610–616. https://doi.org/10.1111/JOPR.13288.

[66] W. Piedra-Cascón, V.R. Krishnamurthy, W. Att, M. Revilla-León, 3D printing parameters, supporting structures, slicing, and post-processing procedures of vat-polymerization additive manufacturing technologies: A narrative review, J. Dent. 109 (2021) 103630. https://doi.org/10.1016/J.JDENT.2021.103630.

[67] A. Unkovskiy, P.H.B. Bui, C. Schille, J. Geis-Gerstorfer, F. Huettig, S. Spintzyk, Objects build orientation, positioning, and curing influence dimensional accuracy and flexural properties of stereolithographically printed resin, Dent. Mater. 34 (2018) e324–e333. https://doi.org/10.1016/J.DENTAL.2018.09.011.

[68] C. Riccio, M. Civera, O.G. Ruiz, P. Pedullà, M.R. Reinoso, G. Tommasi, M. Vollaro, V. Burgio, C. Surace, Effects of Curing on

Photosensitive Resins in SLA Additive Manufacturing, Appl. Mech. 2021, Vol. 2, Pages 942-955. 2 (2021) 942–955. https://doi.org/10.3390/APPLMECH2040055.

[69] J.C. Wang, H. Dommati, Fabrication of zirconia ceramic parts by using solvent-based slurry stereolithography and sintering, Int. J. Adv. Manuf. Technol. 2018 985. 98 (2018) 1537–1546. https://doi.org/10.1007/S00170-018-2349-3.

[70] P. Cai, L. Guo, H. Wang, J. Li, J. Li, Y. Qiu, Effects of slurry mixing methods and solid loading on 3D printed silica glass parts based on DLP stereolithography, Ceram. Int. (2020) 0–1. https://doi.org/10.1016/j.ceramint.2020.03.260.

[71] K. Wang, M. Qiu, C. Jiao, J. Gu, D. Xie, C. Wang, X. Tang, Z. Wei, L. Shen, Study on defect-free debinding green body of ceramic formed by DLP technology, Ceram. Int. 46 (2020) 2438–2446. https://doi.org/10.1016/J.CERAMINT.2019.09.237.

[72] C. Liu, B. Qian, X. Liu, L. Tong, J. Qiu, Additive manufacturing of silica glass using laser stereolithography with a top-down approach and fast debinding, RSC Adv. 8 (2018) 16344–16348. https://doi.org/10.1039/C8RA02428F.

[73] X. Kuang, G. Carotenuto, L. Nicolais, Review of ceramic sintering and suggestions on reducing sintering temperatures, Adv. Perform. Mater. 4 (1997) 257–274. https://doi.org/10.1023/A:1008621020555.

[74] R. He, W. Liu, Z. Wu, D. An, M. Huang, H. Wu, Q. Jiang, X. Ji, S. Wu, Z. Xie, Fabrication of complex-shaped zirconia ceramic parts via a DLP- stereolithography-based 3D printing method, Ceram. Int. 44 (2018) 3412–3416. https://doi.org/10.1016/j.ceramint.2017.11.135.

[75] J.-C. Wang, H. Dommati, Fabrication of zirconia ceramic parts by using solvent-based slurry stereolithography and sintering, Int. J. Adv. Manuf. Technol. 98 (2018) 1537–1546. https://doi.org/10.1007/s00170-018-2349-3.

[76] M. Schwentenwein, J. Homa, Additive Manufacturing of Dense Alumina Ceramics, Int. J. Appl. Ceram. Technol. 12 (2015) 1–7. https://doi.org/10.1111/IJAC.12319.

[77] J. Guo, Y. Zeng, P. Li, J. Chen, Fine lattice structural titanium dioxide ceramic produced by DLP 3D printing, Ceram. Int. 45 (2019) 23007–23012. https://doi.org/10.1016/J.CERAMINT.2019.07.346.

[78] J.W. Lee, I.H. Lee, D.W. Cho, Development of micro-stereolithography technology using metal powder, Microelectron. Eng. 83 (2006) 1253–1256. https://doi.org/10.1016/J.MEE.2006.01.192.

[79] M. Roumanie, C. Flassayer, A. Resch, L. Cortella, R. Laucournet, Influence of debinding and sintering conditions on the composition and thermal conductivity of copper parts printed from highly loaded photocurable formulations, SN Appl. Sci. 3 (2021) 1–11. https://doi.org/10.1007/S42452-020-04049-3/FIGURES/12.

[80] J.Y. Lee, J. An, C.K. Chua, Fundamentals and applications of 3D printing for novel materials, Appl. Mater. Today. 7 (2017) 120–133. https://doi.org/10.1016/J.APMT.2017.02.004.

[81] E. Pei, G.H. Loh, Technological considerations for 4D printing: an overview, Prog. Addit. Manuf. 3 (2018) 95–107. https://doi.org/10.1007/S40964-018-0047-1/FIGURES/22.

[82] M. Srivastava, S. Rathee, Additive manufacturing: recent trends, applications and future outlooks, Prog. Addit. Manuf. 7 (2022) 261–287. https://doi.org/10.1007/s40964-021-00229-8.

[83] M.C. Henn, N.A. Mokadam, Three-dimensional printing to plan intracardiac operations, JTCVS Tech. 9 (2021) 101–108. https://doi.org/10.1016/j.xjtc.2021.02.050.

[84] M.L. Griffith, J.W. Halloran, Freeform fabrication of ceramics via stereolithography, J. Am. Ceram. Soc. 79 (1996) 2601–2608. https://doi.org/10.1111/j.1151-2916.1996.tb09022.x.

[85] N.L. Porter, R.M. Pilliar, M.D. Grynpas, Fabrication of porous calcium polyphosphate implants by solid freeform fabrication: A study of processing parameters and in vitro degradation characteristics, J. Biomed. Mater. Res. 56 (2001) 504–515. https://doi.org/10.1002/1097-4636(20010915)56:4<504::AID-JBM1122>3.0.CO;2-J.

[86] J.-W. Choi, R. Wicker, S.-H. Lee, K.-H. Choi, C.-S. Ha, I. Chung, Fabrication of 3D biocompatible/biodegradable micro-scaffolds using dynamic mask projection microstereolithography, J. Mater. Process. Technol. 209 (2009) 5494–5503. https://doi.org/10.1016/j.jmatprotec.2009.05.004.

[87] M. Zarek, M. Layani, I. Cooperstein, E. Sachyani, D. Cohn, S. Magdassi, M. Zarek, M. Layani, I. Cooperstein, E. Sachyani, D. Cohn, S. Magdassi, 3D Printing of Shape Memory Polymers for Flexible Electronic Devices, Adv. Mater. 28 (2016) 4449–4454.

https://doi.org/10.1002/ADMA.201503132.

[88] D.K. Patel, A.H. Sakhaei, M. Layani, B. Zhang, Q. Ge, S. Magdassi, Highly Stretchable and UV Curable Elastomers for Digital Light Processing Based 3D Printing, Adv. Mater. 29 (2017) 1606000. https://doi.org/10.1002/adma.201606000.

[89] Z. Dong, M. Vuckovac, W. Cui, Q. Zhou, R.H.A. Ras, P.A. Levkin, 3D Printing of Superhydrophobic Objects with Bulk Nanostructure, Adv. Mater. (2021) 2106068. https://doi.org/10.1002/adma.202106068.

[90] P.M. Dickens, R. Stangroom, M. Greul, B. Holmer, K.K.B. Hon, R. Hovtun, R. Neumann, S. Noeken, D. Wimpenny, Conversion of RP models to investment castings, Rapid Prototyp. J. 1 (1995) 4–11. https://doi.org/10.1108/13552549510104401.

[91] S.Y. Kim, Y.S. Shin, H.D. Jung, C.J. Hwang, H.S. Baik, J.Y. Cha, Precision and trueness of dental models manufactured with different 3-dimensional printing techniques, Am. J. Orthod. Dentofac. Orthop. 153 (2018) 144–153. https://doi.org/10.1016/J.AJODO.2017.05.025.

[92] R. He, W. Liu, Z. Wu, D. An, M. Huang, H. Wu, Q. Jiang, X. Ji, S. Wu, Z. Xie, Fabrication of complex-shaped zirconia ceramic parts via a DLP- stereolithography-based 3D printing method, Ceram. Int. 44 (2018) 3412–3416. https://doi.org/10.1016/j.ceramint.2017.11.135.

[93] C. Piconi, Oxide Ceramics for Biomedical Applications, in: Encycl. Mater. Sci. Technol., Elsevier, 2001: pp. 6595–6601. https://doi.org/10.1016/b0-08-043152-6/01165-7.

[94] F. Chen, H. Zhu, J.M. Wu, S. Chen, L.J. Cheng, Y.S. Shi, Y.C. Mo, C.H. Li, J. Xiao, Preparation and biological evaluation of ZrO2 all-ceramic teeth by DLP technology, Ceram. Int. 46 (2020) 11268–11274. https://doi.org/10.1016/J.CERAMINT.2020.01.152.

[95] C. Schmidleithner, S. Malferrari, R. Palgrave, D. Bomze, M. Schwentenwein, D.M. Kalaskar, Application of high resolution DLP stereolithography for fabrication of tricalcium phosphate scaffolds for bone regeneration, Biomed. Mater. 14 (2019) 045018. https://doi.org/10.1088/1748-605X/ab279d.

[96] Z. Liu, H. Liang, T. Shi, D. Xie, R. Chen, X. Han, L. Shen, C. Wang, Z. Tian, Additive manufacturing of hydroxyapatite bone scaffolds via digital light processing and in vitro compatibility, Ceram. Int. 45 (2019) 11079–11086. https://doi.org/10.1016/j.ceramint.2019.02.195.

[97] I. Cooperstein, E. Shukrun, O. Press, A. Kamyshny, S. Magdassi, Additive Manufacturing of Transparent Silica Glass from Solutions, ACS Appl. Mater. Interfaces. 10 (2018) 18879–18885. https://doi.org/10.1021/acsami.8b03766.

[98] D.G. Moore, L. Barbera, K. Masania, A.R. Studart, Three-dimensional printing of multicomponent glasses using phase-separating resins., Nat. Mater. 19 (2020) 212–217. https://doi.org/10.1038/s41563-019-0525-y.

[99] E.M. Hernández-Rodríguez, P. Acosta-Mora, J. Méndez-Ramos, E. Borges Chinea, P. Esparza Ferrera, J. Canales-Vázquez, P. Núñez, J.C. Ruiz-Morales, Prospective use of the 3D printing technology for the microstructural engineering of Solid Oxide Fuel Cell components, Boletín La Soc. Española Cerámica y Vidr. 53 (2014) 213–216. https://doi.org/10.3989/cyv.252014.

[100] B. Ozkan, F. Sameni, F. Bianchi, H. Zarezadeh, S. Karmel, D.S. Engstrøm, E. Sabet, 3D printing ceramic cores for investment casting of turbine blades, using LCD screen printers: The mixture design and characterisation, J. Eur. Ceram. Soc. 42 (2022) 658–671. https://doi.org/10.1016/j.jeurceramsoc.2021.10.043.

[101] J. Cao, M. Idrees, G. Tian, J. Liu, S. Xiong, J. Yuan, P. Wang, Z. Liu, C. Liu, Z. Chen, Complex SiC-based structures with high specific strength fabricated by vat photopolymerization and one-step pyrolysis, Addit. Manuf. (2021) 102430. https://doi.org/10.1016/J.ADDMA.2021.102430.

[102] J. Schmidt, P. Colombo, Digital light processing of ceramic components from polysiloxanes, J. Eur. Ceram. Soc. 38 (2018) 57–66. https://doi.org/10.1016/j.jeurceramsoc.2017.07.033.

[103] A. Shafiee, A. Atala, Tissue Engineering: Toward a New Era of Medicine, Annu. Rev. Med. 68 (2017) 29–40. https://doi.org/10.1146/annurev-med-102715-092331.

[104] G. Ratheesh, J.R. Venugopal, A. Chinappan, H. Ezhilarasu, A. Sadiq, S. Ramakrishna, 3D Fabrication of Polymeric Scaffolds for Regenerative Therapy, ACS Biomater. Sci. Eng. 3 (2017) 1175–1194. https://doi.org/10.1021/ACSBIOMATERIALS.6B00370.

[105] S.H. Kim, H. Hong, O. Ajiteru, M.T. Sultan, Y.J. Lee, J.S. Lee, O.J. Lee, H. Lee, H.S. Park, K.Y. Choi, J.S. Lee, H.W. Ju, I.-S. Hong, C.H. Park, 3D bioprinted silk fibroin hydrogels for tissue engineering, Nat.

Protoc. 2021. (2021) 1–49. https://doi.org/10.1038/s41596-021-00622-1.

[106] Y. Lu, G. Mapili, G. Suhali, S. Chen, K. Roy, A digital micro-mirror device-based system for the microfabrication of complex, spatially patterned tissue engineering scaffolds, J. Biomed. Mater. Res. Part A. 77A (2006) 396–405. https://doi.org/10.1002/JBM.A.30601.

[107] W. Zhu, X. Ma, M. Gou, D. Mei, K. Zhang, S. Chen, 3D printing of functional biomaterials for tissue engineering, Curr. Opin. Biotechnol. 40 (2016) 103–112. https://doi.org/10.1016/j.copbio.2016.03.014.

[108] R.C. Advincula, J.R.C. Dizon, E.B. Caldona, R.A. Viers, F.D.C. Siacor, R.D. Maalihan, A.H. Espera, On the progress of 3D-printed hydrogels for tissue engineering, MRS Commun. 2021 115. 11 (2021) 539–553. https://doi.org/10.1557/S43579-021-00069-1.

[109] N.A. Traugutt, D. Mistry, C. Luo, K. Yu, Q. Ge, C.M. Yakacki, Liquid-Crystal-Elastomer-Based Dissipative Structures by Digital Light Processing 3D Printing, Adv. Mater. 32 (2020) 2000797. https://doi.org/10.1002/adma.202000797.

[110] T. Zhao, R. Yu, S. Li, X. Li, Y. Zhang, X. Yang, X. Zhao, C. Wang, Z. Liu, R. Dou, W. Huang, Superstretchable and Processable Silicone Elastomers by Digital Light Processing 3D Printing, ACS Appl. Mater. Interfaces. 11 (2019) 14391–14398. https://doi.org/10.1021/ACSAMI.9B03156.

[111] W.H.Y. Clarissa, C.H. Chia, S. Zakaria, Y.C.Y. Evyan, Recent advancement in 3-D printing: nanocomposites with added functionality, Prog. Addit. Manuf. 2021. (2021) 1–26. https://doi.org/10.1007/S40964-021-00232-Z.

[112] Q. Mu, L. Wang, C.K. Dunn, X. Kuang, F. Duan, Z. Zhang, H.J. Qi, T. Wang, Digital light processing 3D printing of conductive complex structures, Addit. Manuf. 18 (2017) 74–83. https://doi.org/10.1016/j.addma.2017.08.011.

[113] D.E. Yunus, S. Sohrabi, R. He, W. Shi, Y. Liu, Acoustic patterning for 3D embedded electrically conductive wire in stereolithography, J. Micromechanics Microengineering. 27 (2017) 045016. https://doi.org/10.1088/1361-6439/AA62B7.

[114] H. Wu, P. Chen, C. Yan, C. Cai, Y. Shi, Four-dimensional printing of a novel acrylate-based shape memory polymer using digital light processing, Mater. Des. 171 (2019) 107704.

https://doi.org/10.1016/j.matdes.2019.107704.

[115] X. Zhou, K. Parida, O. Halevi, S. Magdassi, P.S. Lee, All 3D Printed Stretchable Piezoelectric Nanogenerator for Self-Powered Sensor Application., Sensors (Basel). 20 (2020) 1–9. https://doi.org/10.3390/s20236748.

[116] G. Zhu, Y. Hou, J. Xiang, J. Xu, N. Zhao, Digital Light Processing 3D Printing of Healable and Recyclable Polymers with Tailorable Mechanical Properties, ACS Appl. Mater. Interfaces. 13 (2021) 34954–34961. https://doi.org/10.1021/ACSAMI.1C08872.

[117] H. Gong, M. Beauchamp, S. Perry, A.T. Woolley, G.P. Nordin, Optical approach to resin formulation for 3D printed microfluidics, RSC Adv. 5 (2015) 106621–106632. https://doi.org/10.1039/C5RA23855B.

[118] A. V. Nielsen, M.J. Beauchamp, G.P. Nordin, A.T. Woolley, 3D Printed Microfluidics, Annu. Rev. Anal. Chem. 13 (2020) 45–65. https://doi.org/10.1146/annurev-anchem-091619-102649.

[119] F. Alam, M. Elsherif, A.E. Salih, H. Butt, 3D printed polymer composite optical fiber for sensing applications, Addit. Manuf. 58 (2022) 102996. https://doi.org/10.1016/j.addma.2022.102996.

[120] M. Ali, F. Alam, Y.F. Fah, O. Shiryayev, N. Vahdati, H. Butt, 4D printed thermochromic Fresnel lenses for sensing applications, Compos. Part B Eng. 230 (2022) 109514. https://doi.org/10.1016/j.compositesb.2021.109514.

[121] G. Kaur, A. Marmur, S. Magdassi, Fabrication of superhydrophobic 3D objects by Digital Light Processing, Addit. Manuf. 36 (2020) 101669. https://doi.org/10.1016/J.ADDMA.2020.101669.

[122] R. Liska, M. Schuster, R. Inführ, C. Turecek, C. Fritscher, B. Seidl, V. Schmidt, L. Kuna, A. Haase, F. Varga, H. Lichtenegger, J. Stampfl, Photopolymers for rapid prototyping, J. Coatings Technol. Res. 4 (2007) 505–510. https://doi.org/10.1007/s11998-007-9059-3.

[123] N. Arsu, M. Aydin, Y. Yagci, S. Jockusch, N.J. Turro, One component thioxanthone based Type II photoinitiators, in: Photochem. UV Curing New Trends, 2006: pp. 1–13.

[124] A.J. Bean, Radiation Curing of Printing Inks, in: Radiat. Curing, Springer US, Boston, MA, 1992: pp. 301–332. https://doi.org/10.1007/978-1-4899-0712-7_8.

[125] C. Decker, Photoinitiated crosslinking polymerisation, Prog. Polym. Sci. 21 (1996) 593–650. https://doi.org/10.1016/0079-6700(95)00027-5.

[126] J.P. Fouassier, F. Morlet-Savary, J. Lalevée, X. Allonas, C. Ley, Dyes as photoinitiators or photosensitizers of polymerization reactions, Materials (Basel). 3 (2010) 5130–5142. https://doi.org/10.3390/ma3125130.

[127] J.P. Fouassier, J. Lalevée, Photoinitiators for Polymer Synthesis: Scope, Reactivity and Efficiency, Wiley-VCH Verlag GmbH & Co. KGaA, Weinheim, Germany, 2012. https://doi.org/10.1002/9783527648245.

[128] X. Pan, M.A. Tasdelen, J. Laun, T. Junkers, Y. Yagci, K. Matyjaszewski, Photomediated controlled radical polymerization, Prog. Polym. Sci. 62 (2016) 73–125. https://doi.org/10.1016/j.progpolymsci.2016.06.005.

[129] M. Szwarc, M. Van Beylen, Ionic Polymerization and Living Polymers, Springer Dordrecht, Dordrecht, 1993. https://doi.org/10.1007/978-94-011-1478-3.

[130] C. Mendes-Felipe, J. Oliveira, I. Etxebarria, J.L. Vilas-Vilela, S. Lanceros-Mendez, State-of-the-Art and Future Challenges of UV Curable Polymer-Based Smart Materials for Printing Technologies, Adv. Mater. Technol. 4 (2019) 1800618. https://doi.org/10.1002/admt.201800618.

[131] J. V. Crivello, The discovery and development of onium salt cationic photoinitiators, J. Polym. Sci. Part A Polym. Chem. 37 (1999) 4241–4254. https://doi.org/10.1002/(SICI)1099-0518(19991201)37:23<4241::AID-POLA1>3.0.CO;2-R.

[132] W. Schnabel, Polymers and Light, Wiley, Weinheim, Germany, 2007. https://doi.org/10.1002/9783527611027.

[133] H. Lai, X. Peng, L. Li, D. Zhu, P. Xiao, Novel monomers for photopolymer networks, Prog. Polym. Sci. 128 (2022) 101529. https://doi.org/10.1016/j.progpolymsci.2022.101529.

[134] A. Bagheri, J. Jin, Photopolymerization in 3D Printing, ACS Appl. Polym. Mater. 1 (2019) 593–611. https://doi.org/10.1021/acsapm.8b00165.

[135] Y. Yagci, S. Jockusch, N.J. Turro, Photoinitiated Polymerization:

Advances, Challenges, and Opportunities, Macromolecules. 43 (2010) 6245–6260. https://doi.org/10.1021/ma1007545.

[136] S. Nam, E. Pei, A taxonomy of shape-changing behavior for 4D printed parts using shape-memory polymers, Prog. Addit. Manuf. 4 (2019) 167–184. https://doi.org/10.1007/S40964-019-00079-5/FIGURES/28.

[137] J.W. Halloran, Ceramic Stereolithography: Additive Manufacturing for Ceramics by Photopolymerization, Annu. Rev. Mater. Res. 46 (2016) 19–40. https://doi.org/10.1146/annurev-matsci-070115-031841.

[138] S.C. Ventura, S.C. Narang, S. Sharma, J. Stotts, A new sff process for functional ceramic components, in: Solid Free. Fabr. Symp. Proc., 1996: pp. 327–334.

[139] C. Hinczewski, S. Corbel, T. Chartier, Ceramic suspensions suitable for stereolithography, J. Eur. Ceram. Soc. 18 (1998) 583–590. https://doi.org/10.1016/s0955-2219(97)00186-6.

[140] J.W. Halloran, Ceramic Stereolithography: Additive Manufacturing for Ceramics by Photopolymerization, Annu. Rev. Mater. Res. 46 (2016) 19–40. https://doi.org/10.1146/annurev-matsci-070115-031841.

[141] A. Badev, Y. Abouliatim, T. Chartier, L. Lecamp, P. Lebaudy, C. Chaput, C. Delage, Photopolymerization kinetics of a polyether acrylate in the presence of ceramic fillers used in stereolithography, J. Photochem. Photobiol. A Chem. 222 (2011) 117–122. https://doi.org/10.1016/j.jphotochem.2011.05.010.

[142] J.W. Halloran, V. Tomeckova, S. Gentry, S. Das, P. Cilino, D. Yuan, R. Guo, A. Rudraraju, P. Shao, T. Wu, T.R. Alabi, W. Baker, D. Legdzina, D. Wolski, W.R. Zimbeck, D. Long, Photopolymerization of powder suspensions for shaping ceramics, J. Eur. Ceram. Soc. 31 (2011) 2613–2619. https://doi.org/10.1016/j.jeurceramsoc.2010.12.003.

[143] J.H. Jang, S. Wang, S.M. Pilgrim, W.A. Schulze, Preparation and characterization of barium titanate suspensions for stereolithography, J. Am. Ceram. Soc. 83 (2000) 1804–1806. https://doi.org/10.1111/j.1151-2916.2000.tb01467.x.

[144] V. Tomeckova, J.W. Halloran, Flow behavior of polymerizable ceramic suspensions as function of ceramic volume fraction and temperature, J. Eur. Ceram. Soc. 31 (2011) 2535–2542. https://doi.org/10.1016/j.jeurceramsoc.2011.01.019.

[145] R. Gmeiner, G. Mitteramskogler, J. Stampfl, A.R. Boccaccini, Stereolithographic ceramic manufacturing of high strength bioactive glass, Int. J. Appl. Ceram. Technol. 12 (2015) 38–45. https://doi.org/10.1111/ijac.12325.

[146] D. Komissarenko, P. Sokolov, A. Evstigneeva, I. Shmeleva, A. Dosovitsky, Rheological and Curing Behavior of Acrylate-Based Suspensions for the DLP 3D Printing of Complex Zirconia Parts, Materials (Basel). 11 (2018) 2350. https://doi.org/10.3390/ma11122350.

[147] V. Tomeckova, F. Teyssandier, S.J. Norton, B.J. Love, J.W. Halloran, Photopolymerization of acrylate suspensions, J. Photochem. Photobiol. A Chem. 247 (2012) 74–81. https://doi.org/10.1016/j.jphotochem.2012.08.008.

[148] T. Chartier, A. Badev, Y. Abouliatim, P. Lebaudy, L. Lecamp, Stereolithography process: Influence of the rheology of silica suspensions and of the medium on polymerization kinetics - Cured depth and width, J. Eur. Ceram. Soc. 32 (2012) 1625–1634. https://doi.org/10.1016/j.jeurceramsoc.2012.01.010.

[149] K. Zhang, R. He, G. Ding, C. Feng, W. Song, Digital light processing of 3Y-TZP strengthened ZrO 2 ceramics, Mater. Sci. Eng. A. 774 (2020) 138768. https://doi.org/10.1016/j.msea.2019.138768.

[150] W. Liu, H. Wu, Z. Tian, Y. Li, Z. Zhao, M. Huang, X. Deng, Z. Xie, S. Wu, 3D printing of dense structural ceramic microcomponents with low cost: Tailoring the sintering kinetics and the microstructure evolution, J. Am. Ceram. Soc. 102 (2019) 2257–2262. https://doi.org/10.1111/jace.16241.

[151] D. An, H. Li, Z. Xie, T. Zhu, X. Luo, Z. Shen, J. Ma, Additive manufacturing and characterization of complex Al2O3 parts based on a novel stereolithography method, Int. J. Appl. Ceram. Technol. 14 (2017) 836–844. https://doi.org/10.1111/ijac.12721.

[152] S. Zhang, N. Sha, Z. Zhao, Surface modification of α-Al2O3 with dicarboxylic acids for the preparation of UV-curable ceramic suspensions, J. Eur. Ceram. Soc. 37 (2017) 1607–1616. https://doi.org/10.1016/j.jeurceramsoc.2016.12.013.

[153] Y. Wang, Z. Wang, S. Liu, Z. Qu, Z. Han, F. Liu, L. Li, Additive manufacturing of silica ceramics from aqueous acrylamide based suspension, Ceram. Int. 45 (2019) 21328–21332.

https://doi.org/10.1016/j.ceramint.2019.07.118.

[154] M. Borlaf, N. Szubra, A. Serra-capdevila, W.W. Kubiak, T. Graule, Fabrication of ZrO2 and ATZ materials via UV-LCM-DLP additive manufacturing technology, J. Eur. Ceram. Soc. 40 (2020) 1574–1581. https://doi.org/10.1016/j.jeurceramsoc.2019.11.037.

[155] X. Li, H. Zhong, J. Zhang, Y. Duan, J. Li, D. Jiang, Fabrication of zirconia all-ceramic crown via DLP-based stereolithography, Int. J. Appl. Ceram. Technol. 17 (2020) 844–853. https://doi.org/10.1111/ijac.13441.

[156] K. Li, Z. Zhao, The e ff ect of the surfactants on the formulation of UV-curable SLA alumina suspension, Ceram. Int. 43 (2017) 4761–4767. https://doi.org/10.1016/j.ceramint.2016.11.143.

[157] Y. De Hazan, J. Heinecke, A. Weber, T. Graule, High solids loading ceramic colloidal dispersions in UV curable media via comb-polyelectrolyte surfactants, J. Colloid Interface Sci. 337 (2009) 66–74. https://doi.org/10.1016/j.jcis.2009.05.012.

[158] F. Kotz, K. Arnold, W. Bauer, D. Schild, N. Keller, K. Sachsenheimer, T.M. Nargang, C. Richter, D. Helmer, B.E. Rapp, Three-dimensional printing of transparent fused silica glass, Nature. 544 (2017) 337–339. https://doi.org/10.1038/nature22061.

[159] P. Cai, L. Guo, H. Wang, J. Li, J. Li, Y. Qiu, Q. Zhang, Q. Lue, Effects of slurry mixing methods and solid loading on 3D printed silica glass parts based on DLP stereolithography, Ceram. Int. 46 (2020) 16833–16841. https://doi.org/10.1016/j.ceramint.2020.03.260.

[160] G. Ding, R. He, K. Zhang, C. Xie, M. Wang, Y. Yang, D. Fang, Stereolithography-based additive manufacturing of gray-colored SiC ceramic green body, J. Am. Ceram. Soc. 102 (2019) 7198–7209. https://doi.org/10.1111/jace.16648.

[161] R. RIEDEL, G. MERA, R. HAUSER, A. KLONCZYNSKI, Silicon-Based Polymer-Derived Ceramics: Synthesis Properties and Applications-A Review, J. Ceram. Soc. Japan. 114 (2006) 425–444. https://doi.org/10.2109/jcersj.114.425.

[162] Y. de Hazan, D. Penner, Y. De Hazan, D. Penner, SiC and SiOC ceramic articles produced by stereolithography of acrylate modified polycarbosilane systems, J. Eur. Ceram. Soc. 37 (2017) 5205–5212. https://doi.org/10.1016/j.jeurceramsoc.2017.03.021.

[163] Z. Li, Z. Chen, J. Liu, Y. Fu, C. Liu, P. Wang, M. Jiang, C. Lao, Additive manufacturing of lightweight and high-strength polymer-derived SiOC ceramics, Virtual Phys. Prototyp. 15 (2020) 163–177. https://doi.org/10.1080/17452759.2019.1710919.

[164] Y. Gao, G. Mera, H. Nguyen, K. Morita, H.J. Kleebe, R. Riedel, Processing route dramatically influencing the nanostructure of carbon-rich SiCN and SiBCN polymer-derived ceramics. Part I: Low temperature thermal transformation, J. Eur. Ceram. Soc. 32 (2012) 1857–1866. https://doi.org/10.1016/j.jeurceramsoc.2011.09.012.

[165] E. Zanchetta, M. Cattaldo, G. Franchin, M. Schwentenwein, J. Homa, G. Brusatin, P. Colombo, Stereolithography of SiOC Ceramic Microcomponents, Adv. Mater. 28 (2016) 370–376. https://doi.org/10.1002/adma.201503470.

[166] J. Schmidt, A. Alpay, M. Schwentenwein, P. Colombo, Complex mullite structures fabricated via digital light processing of a preceramic polysiloxane with active alumina fillers, J. Eur. Ceram. Soc. 39 (2019) 1336–1343. https://doi.org/10.1016/j.jeurceramsoc.2018.11.038.

[167] M. Wang, C. Xie, R. He, G. Ding, K. Zhang, G. Wang, D. Fang, Polymer-derived silicon nitride ceramics by digital light processing based additive manufacturing, J. Am. Ceram. Soc. 102 (2019) 5117–5126. https://doi.org/10.1111/jace.16389.

[168] L. Brigo, J.E.M. Schmidt, A. Gandin, N. Michieli, P. Colombo, G. Brusatin, 3D Nanofabrication of SiOC Ceramic Structures, Adv. Sci. 5 (2018) 1800937. https://doi.org/10.1002/advs.201800937.

[169] T.A. Pham, D.P. Kim, T.W. Lim, S.H. Park, D.Y. Yang, K.S. Lee, Three-dimensional SiCN ceramic microstructures via nano-stereolithography of inorganic polymer photoresists, Adv. Funct. Mater. 16 (2006) 1235–1241. https://doi.org/10.1002/adfm.200600009.

[170] S. Li, W. Duan, T. Zhao, W. Han, L. Wang, R. Dou, G. Wang, The fabrication of SiBCN ceramic components from preceramic polymers by digital light processing (DLP) 3D printing technology, J. Eur. Ceram. Soc. 38 (2018) 4597–4603. https://doi.org/10.1016/j.jeurceramsoc.2018.06.046.

[171] I. Cooperstein, E. Shukrun, O. Press, A. Kamyshny, S. Magdassi, Additive Manufacturing of Transparent Silica Glass from Solutions, ACS Appl. Mater. Interfaces. 10 (2018) 18879–18885. https://doi.org/10.1021/acsami.8b03766.

[172] X. Wang, F. Schmidt, D. Hanaor, P.H. Kamm, S. Li, A. Gurlo, Additive manufacturing of ceramics from preceramic polymers: A versatile stereolithographic approach assisted by thiol-ene click chemistry, Addit. Manuf. 27 (2019) 80–90. https://doi.org/10.1016/j.addma.2019.02.012.

[173] Z.C. Eckel, C. Zhou, J.H. Martin, A.J. Jacobsen, W.B. Carter, T.A. Schaedler, Additive manufacturing of polymer-derived ceramics, Science (80-.). 351 (2016) 58–62. https://doi.org/10.1126/science.aad2688.

[174] S.A. Brinckmann, N. Patra, J. Yao, T.H. Ware, C.P. Frick, R.S. Fertig, Stereolithography of SiOC Polymer-Derived Ceramics Filled with SiC Micronwhiskers, Adv. Eng. Mater. 20 (2018) 1–10. https://doi.org/10.1002/adem.201800593.

[175] P.J. Bartolo, J. Gaspar, Metal filled resin for stereolithography metal part, CIRP Ann. 57 (2008) 235–238. https://doi.org/10.1016/j.cirp.2008.03.124.

[176] P. Jacobs, Rapid prototyping & manufacturing— Fundamentals of stereolithography, Society of Manufacturing Engineers, Dearborn, 1992. https://books.google.com/books?hl=en&lr=&id=-y33AwAAQBAJ&oi=fnd&pg=PP1&ots=gYewD397Ld&sig=ZqreaCvFILhXfeLHsWcW5us9fvU.

[177] G. Odian, Radical Chain Polymerization, in: Princ. Polym., John Wiley & Sons, Inc., Hoboken, NJ, USA, 2004: pp. 198–349. https://doi.org/10.1002/047147875X.ch3.

[178] M.M. Emami, D.W. Rosen, Modeling of light field effect in deep vat polymerization for grayscale lithography application, Addit. Manuf. 36 (2020) 101595. https://doi.org/10.1016/j.addma.2020.101595.

[179] J.H. Lee, R.K. Prud'homme, I.A. Aksay, Cure depth in photopolymerization: Experiments and theory, J. Mater. Res. 16 (2001) 3536–3544. https://doi.org/10.1557/JMR.2001.0485.

[180] M.L. Griffith, J.W. Halloran, Scattering of ultraviolet radiation in turbid suspensions, J. Appl. Phys. 81 (1997) 2538–2546. https://doi.org/10.1063/1.364311.

[181] T. Scherzer, Depth profiling of the conversion during the photopolymerization of acrylates using real-time FTIR-ATR spectroscopy, Vib. Spectrosc. 29 (2002) 139–145. https://doi.org/10.1016/S0924-2031(01)00202-8.

[182] I.M. Barszczewska-Rybarek, Quantitative determination of degree of conversion in photocured poly(urethane-dimethacrylate)s by Fourier transform infrared spectroscopy, J. Appl. Polym. Sci. 123 (2012) 1604–1611. https://doi.org/10.1002/app.34553.

[183] D. Kunwong, N. Sumanochitraporn, S. Kaewpirom, Curing behavior of a UV-curable coating based on urethane acrylate oligomer: The influence of reactive monomers, Songklanakarin J. Sci. Technol. 33 (2011) 201–207.

[184] L. Feng, B.I. Suh, The Noise in Measurements of Degree of Conversion of (Meth)Acrylates by FTIR-ATR, Int. J. Polym. Anal. Charact. 11 (2006) 133–146. https://doi.org/10.1080/10236660600630418.

[185] C.I. Higgins, T.E. Brown, J.P. Killgore, Digital light processing in a hybrid atomic force microscope: In Situ, nanoscale characterization of the printing process, Addit. Manuf. 38 (2021) 101744. https://doi.org/10.1016/J.ADDMA.2020.101744.

[186] Porcelite®, (n.d.). https://tethon3d.com/wp-content/uploads/Porcelite-User-Guide.pdf (accessed November 25, 2022).

[187] A. Andreu, P.-C. Su, J.-H. Kim, C.S. Ng, S. Kim, I. Kim, J. Lee, J. Noh, A.S. Subramanian, Y.-J. Yoon, 4D printing materials for vat photopolymerization, Addit. Manuf. 44 (2021) 102024. https://doi.org/10.1016/j.addma.2021.102024.

[188] S. Saleh Alghamdi, S. John, N. Roy Choudhury, N.K. Dutta, Additive Manufacturing of Polymer Materials: Progress, Promise and Challenges, Polymers (Basel). 13 (2021) 753. https://doi.org/10.3390/polym13050753.

[189] M. Bhuvanesh Kumar, P. Sathiya, Methods and materials for additive manufacturing: A critical review on advancements and challenges, Thin-Walled Struct. 159 (2021) 107228. https://doi.org/10.1016/j.tws.2020.107228.

[190] A. Vafadar, F. Guzzomi, A. Rassau, K. Hayward, Advances in Metal Additive Manufacturing: A Review of Common Processes, Industrial Applications, and Current Challenges, Appl. Sci. 11 (2021) 1213. https://doi.org/10.3390/app11031213.

[191] Q. Ge, Z. Li, Z. Wang, K. Kowsari, W. Zhang, X. He, J. Zhou, N.X. Fang, Projection micro stereolithography based 3D printing and its applications, Int. J. Extrem. Manuf. 2 (2020) 022004. https://doi.org/10.1088/2631-7990/ab8d9a.

[192] Y. Li, Q. Mao, X. Li, J. Yin, Y. Wang, J. Fu, Y. Huang, High-fidelity and high-efficiency additive manufacturing using tunable pre-curing digital light processing, Addit. Manuf. 30 (2019) 100889. https://doi.org/10.1016/j.addma.2019.100889.